

Science and Technology of Nuclear Installations

Countercurrent Flow Limitations in a Pressurized Water Reactor

Guest Editors: Deendarlianto, Thomas Höhne,
and Michio Murase





Countercurrent Flow Limitations in a Pressurized Water Reactor

Science and Technology of Nuclear Installations

Countercurrent Flow Limitations in a Pressurized Water Reactor

Guest Editors: Deendarlianto, Thomas Höhne,
and Michio Murase



Copyright © 2012 Hindawi Publishing Corporation. All rights reserved.

This is a special issue published in "Science and Technology of Nuclear Installations." All articles are open access articles distributed under the Creative Commons Attribution License, which permits unrestricted use, distribution, and reproduction in any medium, provided the original work is properly cited.

Editorial Board

Nusret Aksan, Switzerland
Antonio C. Marques Alvim, Brazil
Won Pil Baek, Korea
Stephen M. Bajorek, USA
George Bakos, Greece
Jozsef Banati, Sweden
Ricardo Barros, Brazil
Anis Bousbia Salah, Belgium
Giovanni B. Bruna, France
Nikola Čavlina, Croatia
Xu Cheng, China
Leon Cizelj, Slovenia
Alejandro Clausse, Argentina
Francesco D' Auria, Italy
Marcos P. de Abreu, Brazil
Giovanni Dell'Orco, France
Juan Carlos Ferreri, Argentina
Nikolay Fil, Russia
Cesare Frepoli, USA
Giorgio Galassi, Italy
Regina Galetti, Brazil

Michel Giot, Belgium
Valerio Giusti, Italy
Horst Glaeser, Germany
Satish Kumar Gupta, India
Ali Hainoun, Syria
Keith E. Holbert, USA
Kostadin Ivanov, Germany
Yacine Kadi, Republic of Korea
Ahmed Khedr, Egypt
Tomasz Kozłowski, USA
Tomoaki Kunugi, Japan
Mike Kuznetsov, Germany
H.-Y. Lee, Republic of Korea
Bundit Limmeechokchai, Thailand
Jiri Macek, Czech Republic
Annalisa Manera, USA
Borut Mavko, Slovenia
Oleg Melikhov, Russia
Rafael Miró, Spain
Josef Misak, Czech Republic
Rahim Nabbi, Germany

Manmohan Pandey, India
Yuriy Parfenov, Russia
Yves Pontillon, France
Nik Popov, Canada
Piero Ravetto, Italy
Francesc Reventos, Spain
Enrico Sartori, France
Carlo Sborchia, France
Massimo Sepielli, Italy
Arkady Serikov, Germany
James F. Stubbins, USA
Iztok Tiselj, Slovenia
Rizwan Uddin, USA
Eugenijus Ušpuras, Lithuania
Richard Wright, Norway
Chao Xu, China
Yanko Yanev, Bulgaria
Zhiwei Zhou, China
Enrico Zio, Italy
Massimo Zucchetti, Italy

Contents

Countercurrent Flow Limitations in a Pressurized Water Reactor, Deendarlianto, Thomas Höhne, and Michio Murase
Volume 2012, Article ID 608678, 2 pages

Counter Current Flow Limitation of Gas-Liquid Two-Phase Flow in Nearly Horizontal Pipe, Sigit Prayitno, R. A. Santoso, Deendarlianto, Thomas Höhne, and Dirk Lucas
Volume 2012, Article ID 513809, 9 pages

Experimental Characterisation of the Interfacial Structure during Counter-Current Flow Limitation in a Model of the Hot Leg of a PWR, Christophe Vallée, Toshifumi Nariai, Takashi Futatsugi, Akio Tomiyama, Dirk Lucas, and Michio Murase
Volume 2012, Article ID 298452, 8 pages

Numerical Simulation of Size Effects on Countercurrent Flow Limitation in PWR Hot Leg Models, I. Kinoshita, M. Murase, and A. Tomiyama
Volume 2012, Article ID 907364, 7 pages

Countercurrent Flow Limitation at the Junction between the Surge Line and the Pressurizer of a PWR, Taiga Doi, Takashi Futatsugi, Michio Murase, Kosuke Hayashi, Shigeo Hosokawa, and Akio Tomiyama
Volume 2012, Article ID 754724, 10 pages

Image-Processing-Based Study of the Interfacial Behavior of the Countercurrent Gas-Liquid Two-Phase Flow in a Hot Leg of a PWR, Gustavo A. Montoya, Deendarlianto, Dirk Lucas, Thomas Höhne, and Christophe Vallée
Volume 2012, Article ID 209542, 10 pages

Experimental Investigation of Rising Gas Bubble Characteristics from a Vertical Tube under CCFL Condition, Kunihito Matsumura and Fumito Kaminaga
Volume 2012, Article ID 785157, 15 pages

VOF Calculations of Countercurrent Gas-Liquid Flow in a PWR Hot Leg, M. Murase, A. Tomiyama, I. Kinoshita, Y. Utanohara, Chihiro Yanagi, T. Takata, and A. Yamaguchi
Volume 2012, Article ID 935391, 9 pages

Countercurrent Air-Water Flow in a Scale-Down Model of a Pressurizer Surge Line, Takashi Futatsugi, Chihiro Yanagi, Michio Murase, Shigeo Hosokawa, and Akio Tomiyama
Volume 2012, Article ID 174838, 7 pages

Assessment of TRACE CCFL Model with SBLOCA Experiment of IIST Facility, Jung-Hua Yang, Jong-Rong Wang, Hao-Tzu Lin, and Chunkuan Shih
Volume 2012, Article ID 731616, 8 pages

Editorial

Countercurrent Flow Limitations in a Pressurized Water Reactor

Deendarlianto,¹ Thomas Höhne,² and Michio Murase³

¹ Department of Mechanical & Industrial Engineering, Faculty of Engineering, Gadjah Mada University, Jalan Grafika No. 2, Yogyakarta 55281, Indonesia

² Helmholtz-Zentrum Dresden-Rossendorf e.V., Institute of Fluid Dynamics, P.O. Box 510 119, 01314 Dresden, Germany

³ Institute of Nuclear Technology, Institute of Nuclear Safety System, Incorporated, 64 Sata, Mihama-cho, Mikata-gun, Fukui 919-1205, Japan

Correspondence should be addressed to Thomas Höhne, t.hoehne@hzdr.de

Received 6 March 2012; Accepted 6 March 2012

Copyright © 2012 Deendarlianto et al. This is an open access article distributed under the Creative Commons Attribution License, which permits unrestricted use, distribution, and reproduction in any medium, provided the original work is properly cited.

Steam generators in a pressurized water reactor (PWR) nuclear power plant transfer heat from a primary coolant (pressurized water at about 15 MPa) to a secondary coolant (pressurized water/steam at about 7 MPa). The primary coolant water is heated in the core and passes through the steam generators, where it transfers heat to the secondary coolant water to generate steam. The steam then drives a turbine that turns an electric generator. Steam is condensed and returns to the steam generator as feedwater. Hot leg pipes connect the reactor pressure vessel (RPV) and the steam generator (SG) and consist of a combination of horizontal sections, single or multiple elbows, and inclined or vertical sections depending on the manufacturer of the reactor [1].

In the event of hypothetical accident scenarios in PWR, emergency strategies have to be mapped out, in order to guarantee the reliable removal of decay heat from the reactor core, also in case of component breakdown. One essential passive heat removal mechanism is the reflux cooling mode. This mode can appear for instance during a small break loss-of-coolant accident (LOCA) or because of loss of residual heat removal (RHR) systems during midloop operation at plant outage after the reactor shutdown. Here, the accident at Three Mile Island (TMI) Unit 2 in 1979 has already indicated that the core heat removal mechanism during a small-break (SB) LOCA should be understood more clearly [2]. It includes a comprehensive study on the natural circulation cooling capability, such as loop seal clearing and countercurrent flow limitation (CCFL).

In the scenario of an LOCA, it is considered that the reactor will be depressurized and vaporization will take place, thereby creating steam in the PWR primary side. Should this

lead to “reflux condensation,” which may be a favourable event progression, the generated steam will flow to the steam generator through the hot leg. This steam will condense in the steam generator, and the condensate will flow back through the hot leg to the reactor, resulting in countercurrent steam/water flow. In some scenarios, the success of core cooling depends on the behaviour of this countercurrent flow.

In most cases of the CCFL experiments, the liquid flow rate was kept constant, and the gas flow rate was increased and decreased in small increments and decrements, respectively. For small gas flow rate, the liquid film flows countercurrently with the gas phase. During this condition, the pressure difference inside the test section slightly increases with the gas mass flow rate. This regime is defined as the stable countercurrent flow. As the gas flow rate is gradually increased, thus, there is the maximum gas flow rate in which the downflowing water mass flow rate is equal to the inlet liquid mass flow rate. This point is defined as the onset of flooding or CCFL. With further increasing of the gas mass flow rate, the downflowing liquid mass flow rate is close to zero. This point corresponds to the zero liquid penetration. In this situation, the cooling of the reactor core from the hot leg is impossible but may be continued by coolant drained through the cold leg to the downcomer. The region between the CCFL and zero liquid penetration is defined as partial delivery region. In turn, when the gas flow rate is decreased, a point is reached where a fully counter-current gas-liquid two-phase flow is established. This is known as the deflooding point.

Over several decades, a number of experimental and theoretical studies of countercurrent gas-liquid two-phase

flow have been carried out to understand the fundamental aspect of the flooding mechanism and to prove practical knowledge for the safety design of nuclear reactors. They included experimental, scaling parameter development, analytical and computational modeling. Starting from the pioneering work of Wallis [3], extensive experimental data base has been accumulated dealing with a diverse array of conditions from these studies, leading to the development of phenomenological correlations and scaling parameters of the CCFL. Meanwhile, as we can see in the open literature some contradictory conclusions about flooding mechanisms, they were carried out under the same experimental conditions. Therefore, it is very difficult to obtain a general conclusion from the available data.

On the other hand, the nuclear thermal-hydraulic community is also facing today interesting challenges. These include the development and validation of new mathematical and computational tools that will be used for improved and more detailed analysis as well as new generations of reactors. For this purpose, the computational fluid dynamics (CFD) tool is considered to be able to simulate most of two-phase flow configurations encountered in nuclear reactor power plants. The introducing of CFD method on the countercurrent flow in a model of PWR hot leg includes the investigation of CCFL mechanisms, heat transfer effects, flow patterns, hysteresis behaviour, and the extension of the obtained flow behaviour from small scale to full-reactor scale. However, the available literature regarding this important topic is rare.

It is expected by the community that the development of a general model closer to physics and including less empiricism in the CFD model should be considered [4, 5]. Such models are an essential precondition for the application of CFD codes to the modeling of flow-related phenomena in nuclear facilities. Here, the validation of the developed local geometry-independent models for mass, momentum, heat transfer, and scalar transport should be conducted. The necessary validation is performed by comparing model results against measured data.

In view of the above, it has been decided to bring out this special issue. The available papers include the state of the art of CCFL experiment in a simple inclined or vertical pipe, scale down PWR hot leg model, CFD modeling, and development of new data base using image processing technique. Thus, this special issue provides the reader with useful information on the progress of the works regarding CCFL in a PWR, and also on open questions, requirements for further research, modeling, and experimental data.

*Deendarlianto
Thomas Höhne
Michio Murase*

References

- [1] Deendarlianto, T. Höhne, D. Lucas, and K. Vierow, "Gas-liquid countercurrent two-phase flow in a PWR hot leg: a comprehensive research review," *Nuclear Engineering and Design*, vol. 243, pp. 214–233, 2012.
- [2] H. Y. Jeong, "Prediction of counter-current flow limitation at hot leg pipe during a small-break LOCA," *Annals of Nuclear Energy*, vol. 29, no. 5, pp. 571–583, 2002.
- [3] G. B. Wallis, *One-Dimensional Two-Phase Flow*, McGraw Hill, New York, NY, USA, 1969.
- [4] T. Höhne, Deendarlianto, and D. Lucas, "Numerical simulations of counter-current two-phase flow experiments in a PWR hot leg model using an interfacial area density model," *International Journal of Heat and Fluid Flow*, vol. 32, pp. 1047–1056, 2011.
- [5] N. Minami, M. Murase, and A. Tomiyama, "Countercurrent gas-liquid flow in a PWR hot leg under reflux cooling (II) numerical simulation of 1/15-scale air-water tests," *Journal of Nuclear Science and Technology*, vol. 47, no. 2, pp. 149–155, 2010.

Research Article

Counter Current Flow Limitation of Gas-Liquid Two-Phase Flow in Nearly Horizontal Pipe

Sigit Prayitno,¹ R. A. Santoso,¹ Deendarlianto,¹ Thomas Höhne,² and Dirk Lucas²

¹Department of Mechanical & Industrial Engineering, Faculty of Engineering, Gadjah Mada University, Jalan Grafika No. 2 Yogyakarta 55281, Indonesia

²Helmholtz Zentrum Dresden Rossendorf, Institute of Safety Research, P.O. Box 510 119, 01314 Dresden, Germany

Correspondence should be addressed to Deendarlianto, deendarlianto@ugm.ac.id

Received 13 December 2011; Accepted 29 February 2012

Academic Editor: Michio Murase

Copyright © 2012 Sigit Prayitno et al. This is an open access article distributed under the Creative Commons Attribution License, which permits unrestricted use, distribution, and reproduction in any medium, provided the original work is properly cited.

Experimental work about counter current two-phase flow of air and gas in nearly horizontal pipe has been performed. The work was performed in a 1.1 m long circular transparent acrylic pipe with 50 mm inner diameter, in two inclination angle settings (20° and 10° from horizontal). The smooth liquid and air inlet was used. Porous liquid inlet and a nozzle connected with calm section were used as liquid and gas inlet. The effect of liquid properties is examined by using five different working fluids (Water, two different concentration of butanol and glycerin aqua solutions). As for results. (1) CCFL causes a drastic change in the delivered liquid to the lower plenum. (2) The effect of inclination angle is significantly observed. The flooding gas superficial velocity decreases with inclination angle. (3) The liquid viscosity affects the flooding phenomena.

1. Introduction

Counter current flow in vertical tube has many applications in a diverse range of process industries. The phenomenon of flooding is of considerable technological importance, as flooding can be limiting factor in the operation of equipment. For example, in a pressurized water reactor (PWR), the counter-current flow of steam (upward) and cold water (downward) may take place in vertical channels when the emergency core cooling (ECC) water is injected into the reactor vessel. This leads to complex processes including the condensation of steam due to the introduction of cold water in to the reactor core. Most importantly upward steam flow may prevent sufficient cooling of reactor component by ECC water. Flooding phenomena have been studied in order to develop analytical models to predict the onset of flooding velocity. As a result, a large number of correlations have been proposed in the literature to predict it for given set of condition. In spite of the large number of reported results, there is still considerable uncertainty concerning the phenomena at the onset of flooding.

A previous work by Wallis [1] who studied counter current of liquid-gas flow in vertically channel found the

inversely proportional relationship of the liquid and gas velocity. To provide a further observation, Hewitt [2] and Barnea et al. [3] performed an experiment in inclined pipe and showed the effect of inclination angle. They found that the effect of inclination angle is complicated. The flow rate at which flooding occurs increases and then decreases as the inclination angle is changed from horizontal to vertical. In the other hand, Pantzali et al. [4] showed the tendency of the flooding gas flow rate increase with the increase of the inclination angle.

Another important aspect in flooding is the influence of the liquid properties. Kamei et al. [5] performed an experimental work about the effect of surface tension in flooding phenomena. They concluded that the flooding gas velocity increases with the decrease of surface tension. A further experimental work performed by Suzuki et al. [6] conclude that the effect of surface tension is complicated. The opposite result was showed by Ousaka et al. [7], Chung et al. [8], and Zapke and Kröger [9]. They showed that surface tension had a stabilizing effect on flooding. It is proved by the instability of interfacial area and the decrease of flooding velocity with the decrease of surface tension. An experimental work about the effect of liquid viscosity was performed by Clift et al. [10],

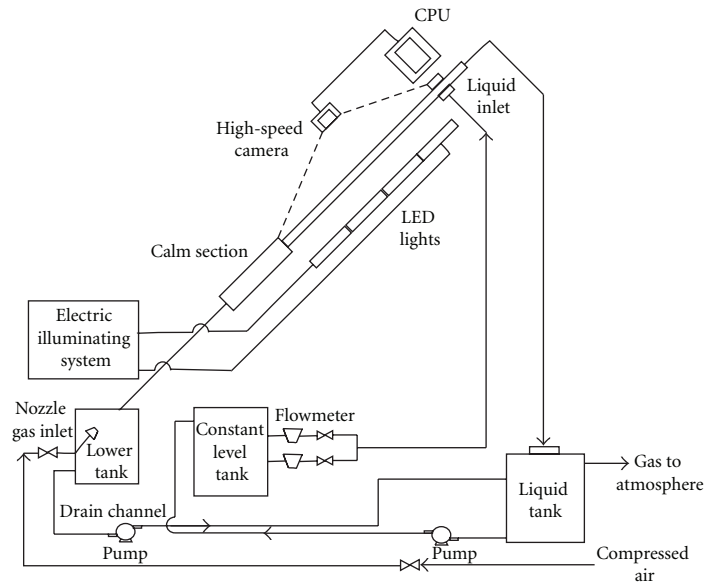


FIGURE 1: The schematic of experimental apparatus.

they found the destabilizing effect of viscosity, an increase of viscosity is followed with the decrease of flooding velocity. This result is fully in agreement with Tien et al. [11], Chung et al. [8], Zapke and kröger [9], Mouza et al. [12], and Nariai et al. [13]. Suzuki et al. [6] found the opposite trend. They found that the flooding velocity tend to increase with an increase in liquid viscosity.

The previous experimental works revealed that the agreement has not been met. The main objective of the work described in the present experimental work is to examine the influence of the fluid properties and the pipe inclination on the CCFL. Air, water, and two different butanol and glycerin aqua solutions were used as the working fluid for this purpose. The two inclination angles, 20° and 10° from horizontal axis are used to provide more observation data that is very limited in the low-inclination angle.

2. Experimental Apparatus

A scheme of this present experimental facility is shown in Figure 1. The tests were performed in a 1.1 m long circular transparent acrylic pipe with 50 mm inner diameter. The transparent circular acrylic test section was mounted in the aluminium beam, which designed to be able to be assembled in two inclination angles: 20 and 10 degree from horizontal axis. Compressed air was supplied by a reservoir, and the flow gas was regulated by the digital regulator. Air entered via nozzle connected to the lower plenum and calm section to provide a smoother air flow rate entering the test section. The air flows from the larger to the small section area of the calm section to minimize the disturbance effect in the air streamline. This method was used in the previous work done by Deendarlianto et al. [14]. The liquid was supplied by the feeder pump connected to the liquid tank. The liquid supply flow rate and temperature were measured with signet flow

transmitter and the digital thermometer to assure the liquid supplied as the experimenter expected. The detail of the air inlet and calm section geometry are shown in Figures 2 and 3. The porous liquid entry was used as the smooth liquid entry as shown in Figure 4.

The present experiments were performed using air and five test liquids, that is water, two difference concentration of butanol and glycerin aqua solutions, thus providing test liquid with a variation of surface tension σ and viscosity μ . The liquid properties were measured in the ambient temperature condition, that is, $\pm 22^\circ\text{C}$ and their properties are given in Table 1. The sample of the liquid tests is taken during the experiment and compared to the data sheet of liquid properties of the mixtures. A good agreement was resulted, the mixtures were under soluble condition and met the liquid properties data sheet.

The onset of flooding was detected as follows, that is, by stepwise increase with a small increment of air-flow rate under a constant water flow rate. Firstly we waited for a few minutes to ensure the flow pattern was in a steady state after the change of the air flow rate. At the same time, a visual data observation and the delivered liquid flow rate were recorded. The onset of flooding was defined as the limiting point of stability of the counter-current flow, indicated by the maximum air flow rate at which the delivered liquid flow rate was equal to the inlet liquid flow rate. As the air flow rate was increased continuously, a flow pattern transition occurs. The stable counter current flow tended to be unstable. The unstable counter current flow was indicated at which the difference of the liquid flow rate from upper plenum to the delivered liquid flow rate in the lower plenum was found. The delivered liquid flow rate in the lower plenum decreases with an increase in the air flow rate. This condition is called as counter current flow limitation (CCFL) or flooding. This

TABLE 1: Liquid properties*.

Fluid	Density [kg/m ³]	Surface tension [mN/m]	Viscosity [mPa.s]	Index
Water	997.00	73.62	1.002	W1
30% glycerin aqua solution	1064.25	69.49	2.633	V1
50% glycerin aqua solution	1104.6	69.34	5.164	V2
2% butanol aqua solution	994	51.45	1.245	S1
5% butanol aqua solution	989.5	39.76	1.266	S2

*The measured fluid properties were measured in the ambient condition ($P = 101325 \text{ N/m}^2$, $T = 295 \text{ }^\circ\text{K}$).

method was used by the previous investigators such as Celata et al. [15] and Deendarlianto et al. [14].

The superficial velocity is described as the ratio between flow rate and crosssection of the circular channel as shown below:

$$J_k = \frac{Q}{A_s}, \quad (1)$$

at which subscript k indicates G supplied gas and L, d delivered liquid phase, J superficial velocity, Q flowrate, and A_s inner crosssection area of the circular acrylic pipe.

The experimental conditions were conducted in the range of supplied liquid superficial velocity $J_L = 0.023 \sim 0.24 \text{ m/s}$ and that of air $J_G = 0 \sim 13.8 \text{ m/s}$.

3. Results and Discussion

To simplify the explanation in this paper, we use some abbreviations for the test liquids by referring to their liquid properties. The significance of abbreviations described in this paper is as follows: W1: air-water ($\sigma = 0.073 \text{ N/m}$ and $\mu = 0.001 \text{ Pa.s}$), S1: 2% butanol aqua solution ($\sigma = 0.051 \text{ N/m}$), S2: 5% butanol aqua solution ($\sigma = 0.039 \text{ N/m}$), V1 30% glycerin aqua solution ($\mu = 0.0026 \text{ Pa.s}$) and V2 50% glycerin aqua solution ($\mu = 0.0051 \text{ Pa.s}$).

Figure 5 illustrates the effect of pipe inclination angle on the CCFL in terms of the gas superficial velocities J_G and the delivered liquid superficial velocities $J_{L,d}$. The effect of inclination angle was found in the range of $J_{L,d} \leq 0.15 \text{ m/s}$ at which flooding occurs in the pipe section. The flooding gas superficial velocities observed tend to decrease in the decrease of the pipe inclination angle. It might be as the effect of gravitational forces. The decrease of the inclination angle dilutes the gravity force, it means that the role of gravity force to counteract the air flow rate becomes weaker in the decrease of inclination angle, therefore, the air flow rates needed to make an upward liquid flow decrease in the decrease of inclination angle. It causes the slope of the plotted 20° CCFL curve to be higher than 10° CCFL curve as shown in Figure 5. Figures 5(a), 5(b), 5(c), and 5(d) show that the effect of inclination angle is getting weaker at high delivered liquid superficial velocities. It is proved by the two plotted curves that are closer to each other. It may be considered as the effect of an irregular wave formed in the liquid inlet area and tends to block the crosssection. This indicates the occurrence of the entrance flooding.

In order to observe the behavior of the liquid film on the CCFL condition, visual observation was performed by

the Redlake Motion Pro high-speed video camera. Bundled with 500 fps and 1280×1024 as the maximum framerate and resolution, it can assure the good quality of visual observation data. The camera is set up in the 200 frames per second to provide a good visual observation data as shown in Figures 6, 7, and 8. A tendency is observed, the liquid film flows like a wavy appears at the onset of flooding, then the waves increase in the height. As the wave height reaches a certain value, the wave begins to be broken up by the air flow. There is some droplet entrainment in air flow rate. The three liquid tests show the same trend, but it is not fully the same. The different phenomena are shown by the three liquid tests (W1, S2, and V2). V2 shows the higher height and frequency of the wave formed, compared to W1 in the same of time range. S2 shows that the droplet entrainment occurs in the smaller wave compared to W1, it means that the height of the wave needed to be broken is smaller than other. These indicate that CCFL characteristic depends on the liquid properties.

Wallis [1] proposed the dimensionless number or known as Wallis parameter, J_k^* , in terms of the dimensionless gas and liquid superficial velocities to predict the onset of flooding in vertical pipe. It is defined as follows:

$$J_k^* = J_k \sqrt{\frac{\rho_k}{gD(\rho_l - \rho_g)}}, \quad (2)$$

at which subscript k indicates G gas and L, d delivered liquid phase, ρ the density, and D is the inner diameter of the pipe used. The correlation is expressed as,

$$J_G^{*1/2} + m J_{L,d}^{*1/2} = C, \quad (3)$$

the constants m and C are based on the experiment set up and condition.

Figure 9 illustrates the effect of surface tension on the CCFL in terms of the dimensionless number as proposed by Wallis in which (a) and (b) correspond to the cases of W1, S1, S2, in the 20 and 10 degree inclination angle. The close observation of the figure reveals that the effect surface tension on CCFL is not significantly observed. The destabilizing effect of surface tension was only observed in the liquid film behavior as shown in Figure 8. The very chaotic flow pattern was shown. It can be explained as the decrease of surface tension means a smaller pressure difference in the liquid-gas interfacial area can be restrained by the liquid film. It causes the liquid behavior to be unstable flow easily. Therefore, the more chaotic flow is performed and the droplet entrainment

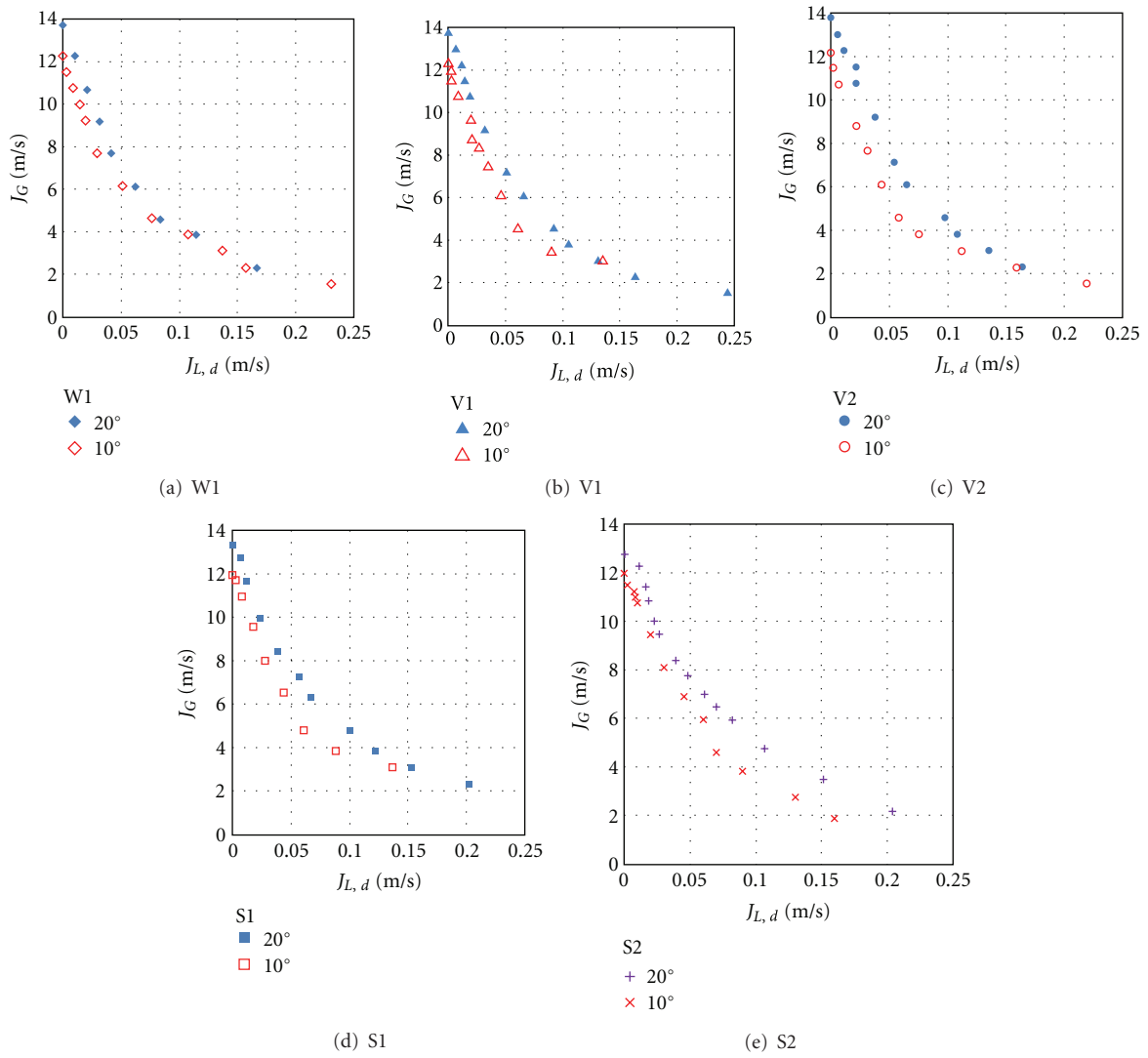


FIGURE 5: Effect of pipe inclination angle in the flooding.

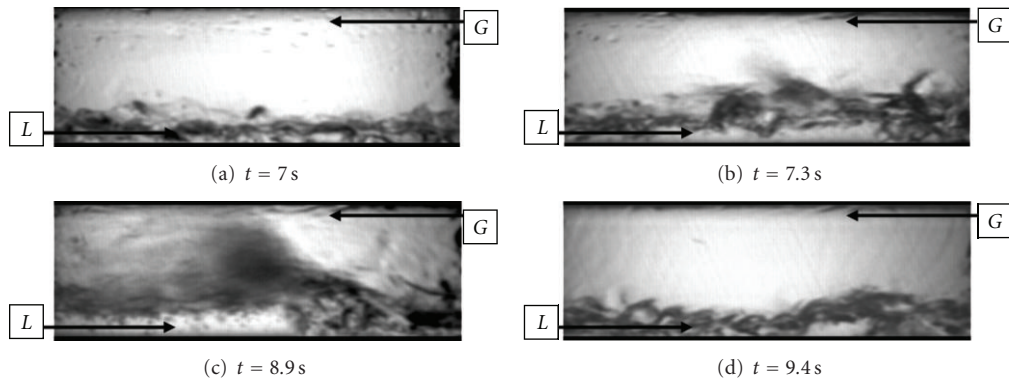


FIGURE 6: A typical sequence of frames showing the liquid film behavior on CCFL condition of W1 ($J_{L,d} = 0.0019$ m/s, $J_G = 9.2$ m/s and $\theta = 10^\circ$).

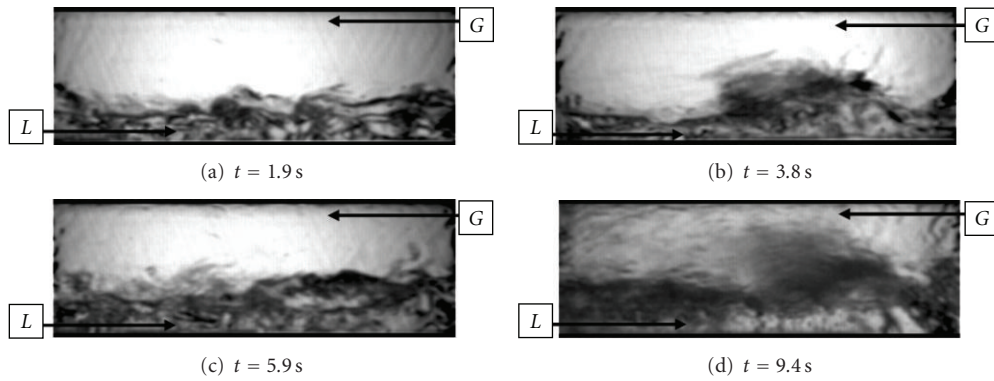


FIGURE 7: A typical sequence of frames showing the liquid film behavior on CCFL condition of V2 ($J_{L,d} = 0.0018$ m/s, $J_G = 9.19$ m/s and $\theta = 10$).

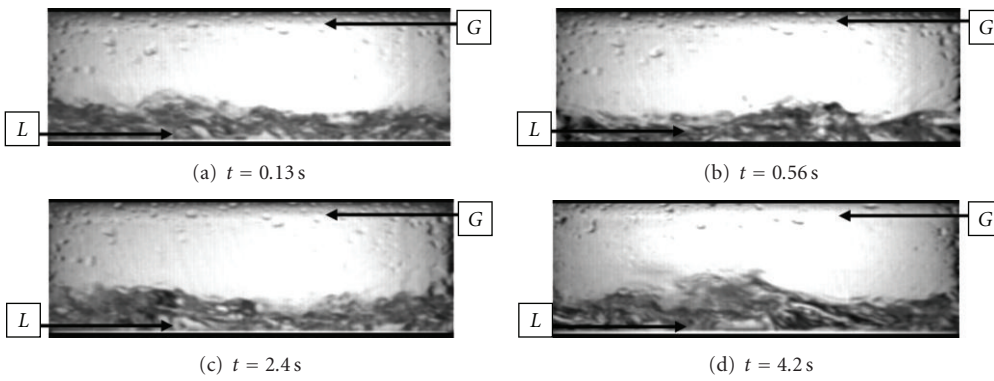


FIGURE 8: A typical sequence of frames showing the liquid film behavior on CCFL condition of S2 ($J_{L,d} = 0.0084$ m/s, $J_G = 10.8047$ m/s and $\theta = 10^\circ$).

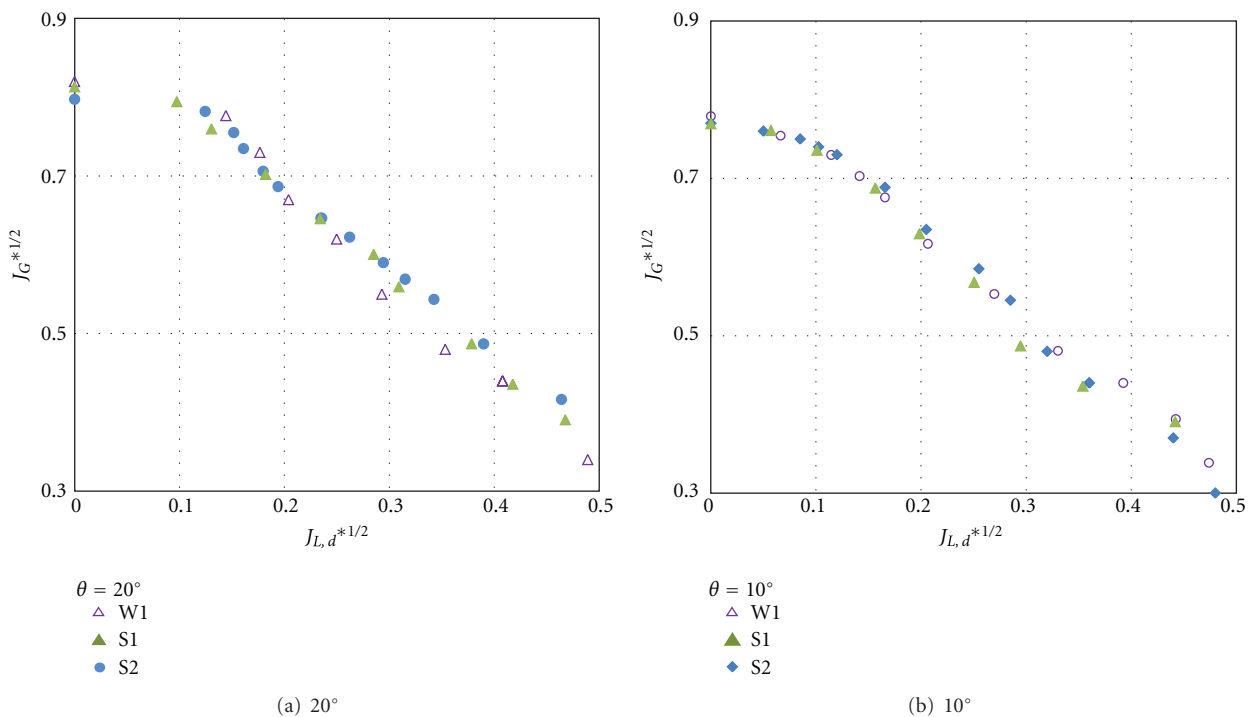


FIGURE 9: The effect of liquid surface tension on the flooding.

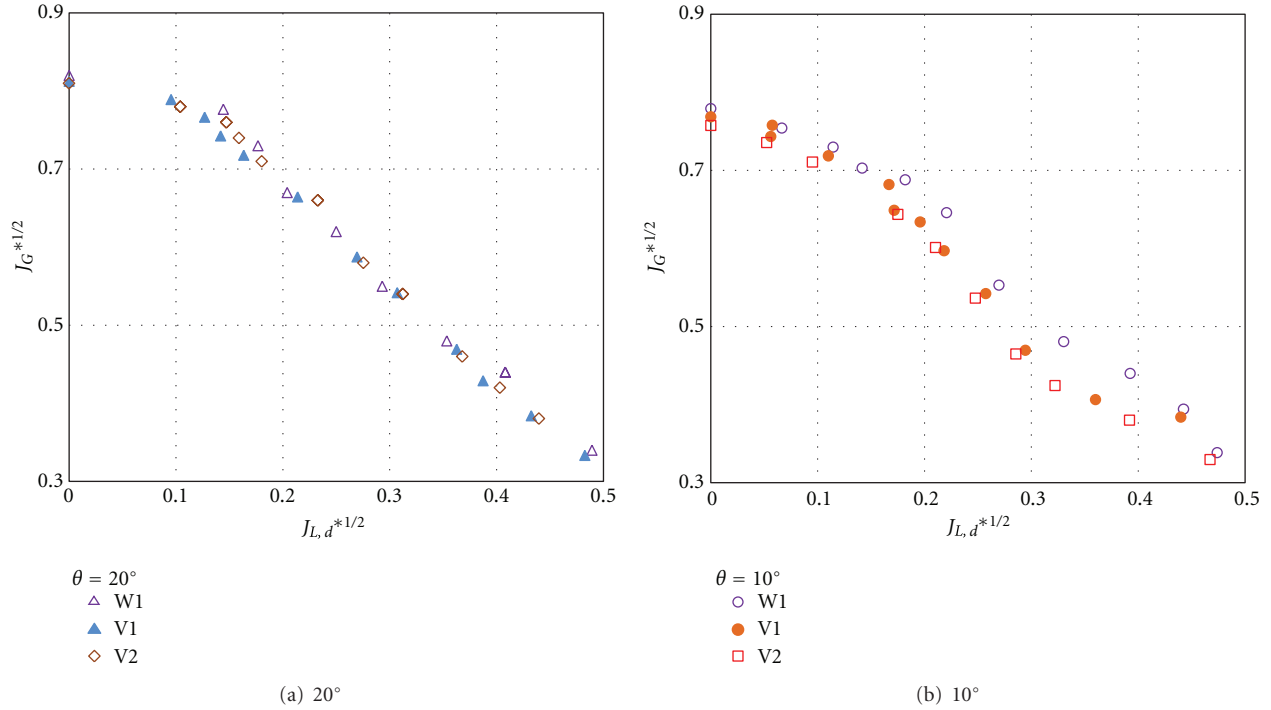


FIGURE 10: The effect of the liquid viscosity on flooding.

occurs in the smaller wave height. It is very interesting that the observed chaotic flow pattern does not significantly affect the plotted gas flooding superficial velocities. It is proved by the plotted CCFL curve that perform close to each other as shown in Figure 9. This result is in fully agreement with Nariai et al. [13] who performed the CCFL experiment in the same inner diameter pipe used in this present work. The Figures 9(a) and 9(b) show the different slope of the two plotted inclination angle experiment data. The curve slope of Figure 9(a) is higher than 9(b), it is considered as the slope “*m*” in Wallis correlation closely related to geometrical dimension. The geometrical dimension here is inclination angle. The inclination angle corresponds to the gravity force that dominantly influences the CCFL in both of plotted W1, S1 and S2 curves.

Further observation was done to examine the effect of the viscosity on flooding. Figure 10 shows CCFL data plotted in terms of dimensionless number proposed by Wallis. An increase in the liquid viscosity means an increase in the flow resistance. As the liquid flows down, the liquid film pressure reduces due to the effect of friction, hence the pressure different in the liquid-gas interface area increases. A fluctuated wave is formed to compensate the additional pressure different in the liquid-gas interface area. Figure 10(a) shows that the CCFL curves of W1, V1 and V2 are close to each other. It means that the fluctuated wave does not always correspond to the destabilizing effect, there is stabilizing mechanism that is able to delay the destabilizing effect. Chung et al. [8] proposed a new viscous effect, that is, viscous damping effect which was not accounted before. Viscous damping as the ability of the liquid to stabilize the flow behavior will counteract with the destabilizing

effect of viscosity, therefore, the net liquid viscosity effect is found to be very small. The different condition is illustrated by Figure 10(b), an increase in the viscosity causes the decrease of the gas superficial velocity. It is considered as the destabilizing effect of viscosity. The destabilizing effect of viscosity appears dominantly to the viscous dumping. It is proved by the high-frequency wave formed as shown in the Figure 7. It may be caused by the effect of inclination angle that dilutes the gravity forces that correspond to the viscous damping effect. Therefore, the CCFL curves of V1 and V2 tend to lag behind the W1.

A comparison is made to know the tendency of the flooding experimental works in inclined pipe. The comparison in the inclined pipe is made by plotting the data in the dimensionless number as shown in Figure 11.

Figure 11(a) shows a comparison of the present experimental data with the data resulted by Barnea et al. [3] and Geweke et al. [16]. Although this present work used the same inner diameter pipe as Barnea et al. [3] and Geweke et al. [16], the comparison indicates that there is a different condition observed in these experiments. The Barnea et al. data shows the highest $J_G^{*1/2}$ than others. It may be caused by the 10 meters long pipe and the difference of the definition of the flooding used. Geweke et al. [16] data shows the closely agreement with the present, it performs a slightly higher plotting. It may be due to the higher pressure of the system used than the present work used. As we knows from the literature that the higher pressure system condition tends to increase the flooding velocities, it is considered as the effect of the fluid properties used, change with the function of pressure, and temperature condition.

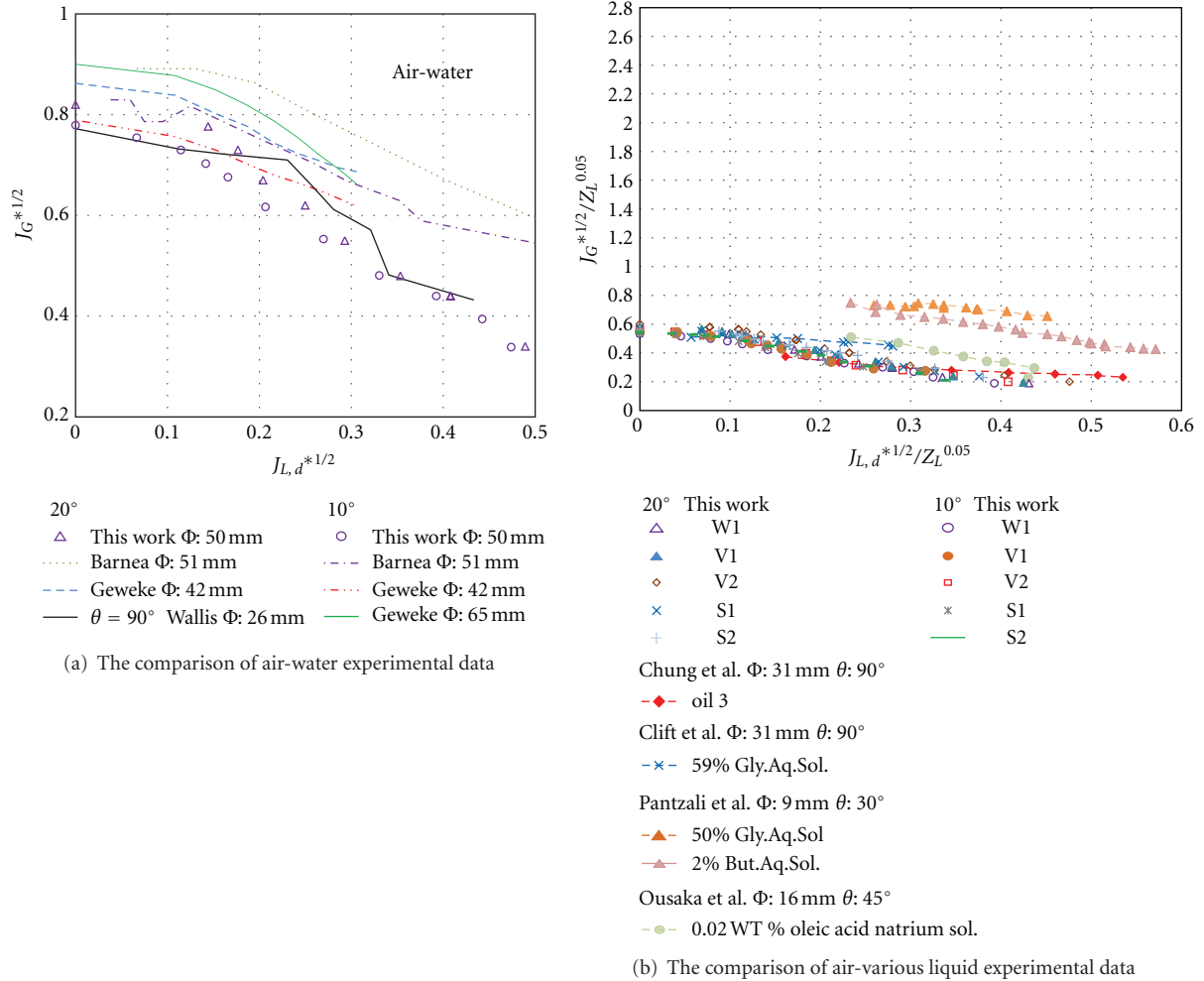


FIGURE 11: The data comparison of flooding experimental data.

An increase in the pipe inclination angle, the experimental data resulted by Wallis [1] show a slight lower CCFL curve. It may be due to the difference in diameter used in his vertical pipe flooding experiment.

Zapke and Kröger [9] examined the countercurrent gas-liquid flow in inclined tubes. They noted that the flooding is significantly affected by the liquid properties. They claim that the constant C in the Wallis correlation is a function of the liquid properties. Then, they proposed a dimensionless liquid property parameter to be combined with the Wallis correlation to provide a trend of flooding phenomena. It was proved successfully to correlate some experimental data. The liquid property parameter is defined as follows:

$$Z_L = \frac{\sqrt{D\rho_L\sigma}}{\mu_L}. \quad (4)$$

A further comparison is made to evaluate the combination of Wallis dimensionless number J_k^* and Zapke dimensionless liquid property Z_L to correlate the flooding experimental data. The comparison is made by the combination of

$J_k^{*0.5}/Z_L^{0.05}$ to be the axis of the plotted data. This combination was proved as good enough correlation number by Zapke and Kröger [9]. It was proved by the good correlation of some experimental work data that concern in examining the effect of liquid properties.

As shown in Figure 11(b) it is shown that the combination of Wallis and the liquid property does not fully correlate the data. The data scatter widely, especially for an extremely change of geometrical dimension like inner diameter and inclination angle as shown in Ousaka et al. [7] and Pantzali et al. [4] plotted data. A new parameter is needed to be found to provide a general flooding correlation.

4. Conclusion

The onset of flooding in nearly horizontal pipe was investigated experimentally. The tube diameter and tube length were 50 mm and 1.1 m, respectively. The experiments were carried out using water, two different concentrations of butanol aqua solution and glycerin aqua solution as test liquids. The results are summarized as follows.

- (1) The flooding is characterized by the inversely proportional relation of the flooding velocities that is, the flooding gas superficial velocities decrease with an increase in the liquid flow rate.
- (2) The effect of inclination angle is significantly observed to affect the flooding phenomena. A decrease of the flooding gas superficial velocities is observed with the decrease of inclination angle.
- (3) The liquid viscosity influence in the flooding phenomena is relatively stronger than the surface tension effect. It is proved by the destabilizing effect of viscosity that is strong enough to decrease the flooding gas superficial velocities.
- (4) The viscous dumping effect is found as the minor effect of the liquid viscosity. This effect becomes stronger in a little change of the liquid viscosity, but the destabilizing effect of liquid viscosity is to be dominant in the decrease of inclination angle.

Acknowledgments

The author would like to thank Dr. Deendarlianto for the knowledge, assistance, and patience in the performance of the experiment and the Helmholtz Zentrum Dresden Rossendorf Topflow Facility crews for their contribution in this experiment. This work is also partly supported by Alexander Van Humboldt Foundation in Germany.

References

- [1] G. B. Wallis, *One-Dimensional Two-Phase Flow*, chapter 11, McGraw Hill, New York, NY, USA, 1969.
- [2] G. F. Hewitt, "Influence of end conditions, tube inclination and physical properties on flooding in gas liquid flows," Harwell Report HTFS-RS 222, 1977.
- [3] D. Barnea, N. Ben Yoseph, and Y. Taitel, "Flooding in inclined pipes: effect of entrance section," *Canadian Journal of Chemical Engineering*, vol. 64, no. 2, pp. 177–184, 1986.
- [4] M. A. Pantzali, A. A. Mouza, and S. V. Paras, "Study of hydrodynamic characteristics of the liquid layer during counter-current flow in inclined small diameter tubes: the effect of liquid properties," in *Proceedings of the 6th International Conference on Multiphase Flow (ICMF '07)*, Leipzig, Germany, 2007.
- [5] S. Kamei, J. Onishi, and T. Okane, "Flooding in a wetted wall tower," *Chemical Engineering*, vol. 18, pp. 364–368, 1954.
- [6] S. Suzuki and T. Ueda, "Behaviour of liquid films and flooding in counter-current two-phase flow-part 1. flow in circular tubes," *International Journal of Multiphase Flow*, vol. 3, no. 6, pp. 517–532, 1977.
- [7] A. Ousaka, Deendarlianto, A. Kariyasaki, and T. Fukano, "Prediction of flooding gas velocity in gas—liquid counter-current two-phase flow in inclined pipes," *Nuclear Engineering and Design*, vol. 236, no. 12, pp. 1282–1292, 2005.
- [8] K. S. Chung, C. P. Liu, and C. L. Tien, "Flooding in two-phase countercurrent flows-II: experimental investigation," *Physicochemical Hydrodynamics*, vol. 1, pp. 209–220, 1980.
- [9] A. Zapke and D. G. Kröger, "The influence of fluid properties and inlet geometry on flooding in vertical and inclined tubes," *International Journal of Multiphase Flow*, vol. 22, no. 3, pp. 461–472, 1996.
- [10] R. Clift, C. L. Pritchard, and R. M. Nedderman, "The effect of viscosity on the flooding conditions in wetted wall columns," *Chemical Engineering Science*, vol. 21, no. 1, pp. 87–95, 1966.
- [11] C. L. Tien and C. P. Liu, "Survey on vertical two phase counter-current flooding," EPRINP-984, 1979.
- [12] A. A. Mouza, S. V. Paras, and A. J. Karabelas, "Incipient flooding in inclined tubes of small diameter," *International Journal of Multiphase Flow*, vol. 29, no. 9, pp. 1395–1412, 2003.
- [13] T. Nariai, A. Tomiyama, C. Vallée, D. Lucas, I. Kinoshita, and M. Murase, "Counter-current flow limitation in a scaled-down model of a PWR hot leg," in *Proceedings of the International Topical Meeting on Nuclear Thermal-Hydraulics, Operation and Safety (NUTHOS-8) N8P0109*, pp. 10–14, Shanghai, China, 2010.
- [14] Deendarlianto, A. Ousaka, A. Kariyasaki, T. Fukano, and M. Konishi, "The effects of surface tension on the flow pattern and counter-current flow limitation (CCFL) in gas-liquid two-phase flow in an inclined pipe," *Japanese Journal of Multiphase Flow*, vol. 18, pp. 337–350, 2004.
- [15] G. P. Celata, M. Cumo, and T. Setaro, "A data set of flooding in circular tubes," *Experimental Thermal and Fluid Science*, vol. 5, no. 4, pp. 437–447, 1992.
- [16] H. Beckmann and D. Mewes, "Experimental studies of counter-current flow in inclined tubes," in *Proceedings of the European Two Phase Flow Group Meeting*, p. B1, Rome, Italy, 1991.

Research Article

Experimental Characterisation of the Interfacial Structure during Counter-Current Flow Limitation in a Model of the Hot Leg of a PWR

Christophe Vallée,¹ Toshifumi Nariai,² Takashi Futatsugi,² Akio Tomiyama,² Dirk Lucas,¹ and Michio Murase³

¹ Institute of Safety Research, Helmholtz-Zentrum Dresden-Rossendorf (HZDR), 01314 Dresden, Germany

² Graduate School of Engineering, Kobe University, Nada-ku, Kobe-shi, Hyogo 657-8501, Japan

³ Institute of Nuclear Technology, Institute of Nuclear Safety System, Inc. (INSS), Mihama-cho, Mikata-gun, Fukui 919-1205, Japan

Correspondence should be addressed to Christophe Vallée, c.vallee@hzdr.de

Received 27 November 2011; Accepted 3 February 2012

Academic Editor: Deendarlianto

Copyright © 2012 Christophe Vallée et al. This is an open access article distributed under the Creative Commons Attribution License, which permits unrestricted use, distribution, and reproduction in any medium, provided the original work is properly cited.

In order to investigate the two-phase flow behaviour during counter-current flow limitation in the hot leg of a pressurised water reactor, dedicated experiments were performed in a scaled down model of *Kobe University*. The experiments were performed with air and water at atmospheric pressure and room temperature. At high flow rates, CCFL occurs and the discharge of water to the reactor pressure vessel simulator is limited by the formation of slugs carrying liquid back to the steam generator. The structure of the interface was observed from the side of the channel test section using a high-speed video camera. An algorithm was developed to recognise the stratified interface in the camera frames after background subtraction. This method allows extracting the water level at any position in the image as well as performing further statistical treatments. The evolution of the interfacial structure along the horizontal part of the hot leg is shown by the visualisation of the probability distribution of the water level and analysed in function of the liquid and gas flow rates. The data achieved are useful for the analysis of the flow conditions as well as for the validation of modelling approaches like computational fluid dynamics.

1. Introduction

In the event of hypothetical accident scenarios in a pressurised water reactor (PWR), emergency strategies have to be mapped out, in order to guarantee the reliable removal of the decay heat from the reactor core, also in case of component breakdown. Therefore, the primary circuit is designed to favour a natural circulation which allows to release the heat to the secondary circuit over the steam generators (SGs). One essential passive heat removal mechanism is the reflux cooling mode. In the reflux condenser mode, the water level in the reactor pressure vessel (RPV) is already reduced to the level of the hot leg nozzle or even below, consequently, only steam flows to the steam generator. The steam coming from the RPV condenses in the vertical U-tubes of the steam generator and, in each half of the steam generator, the condensate flows down the tube in which it has been formed.

Therefore, about one half of the condensate flows as usual over the pump to the downcomer, whereas the other part flows over the hot leg back to the upper plenum. In the hot leg, the condensate has to flow in counter current to the steam.

However, the stratified counter-current flow of condensate and steam is only stable for a certain range of flow rates. In fact, if the steam flow increases too much, the condensate is clogged in the hot leg. This is the onset of the counter-current flow limitation (CCFL): the liquid is carried over by the steam and partially entrained in opposite direction to the steam generator. As a consequence, the hot leg and steam generator are flooded, which decreases the water level in the RPV and reduces the core cooling. In case of an additional increase of the steam flow, the condensate is completely blocked and the reflux cooling mode ends. In this situation the cooling of the reactor core from the hot leg is impossible,

but may be continued by coolant drained through the cold leg to the downcomer.

The reflux condenser cooling mode can appear for instance during a small break loss of coolant accident (LOCA) or because of a loss of residual heat removal (RHR) system during midloop operation at plant outage after its shutdown. For the validation and optimisation of accident management strategies, such transient scenarios are reproduced in dedicated facilities or rather simulated. The use of one-dimensional system codes, which are principally based on empirical correlations, is a common practice. The implemented correlations are adapted to reflect the macroscopic flow characteristics and were extensively validated in the past; consequently, they can be used for safety analyses. However, the correlations do not allow to predict the flow conditions from first principles, and therefore, present limitations. In particular for the flow situations dominated by 3D effects, a computational fluid dynamics (CFDs) approach is required to evaluate the local behaviour in detail. These simulation methods are not yet mature and have to be validated before they can be applied to nuclear reactor safety. Therefore, dedicated experimental data is needed with high resolution in space and time.

To support the theoretical model development and the validation of CFD codes, air/water counter-current flow experiments were performed in a scaled down model of the hot leg of a PWR built at Kobe University. The present study investigates the structure of the interface observed from the side of the channel test section using a high-speed video camera. After some image scaling evaluations, an algorithm developed to recognise the stratified interface in the camera frames after background subtraction will be presented. Finally, the evolution of the water level along the hot leg will be analysed in function of the liquid and gas flow rates with help of statistical treatments showing the global structure of the interface.

2. Previous Investigations of Counter-Current Flow Limitation in PWR Hot Legs

The first detailed investigations on counter-current flow limitation in a hot leg typical geometry (i.e., a horizontal conduit connected to a riser) date back to the late seventies. Richter et al. [1] performed air/water experiments in a scaled down model of the hot leg of a PWR. The test section was made of acrylic glass in order to allow visual observation of the two-phase flow. They proposed to correlate the obtained flooding data with the nondimensional superficial velocity introduced by Wallis [2] in 1969 for vertical counter-current flows in pipes. In 1980, Krolewski [3] established the experimental flooding characteristic of five different hot leg geometries with air and water. She shows that the characteristic of the CCFL depends significantly on the angle of the riser as well as on the inlet and outlet geometry.

Later on, Ohnuki [4] performed counter-current flow limitation experiments in a horizontal pipe connected to an inclined riser with air/water and saturated steam/water

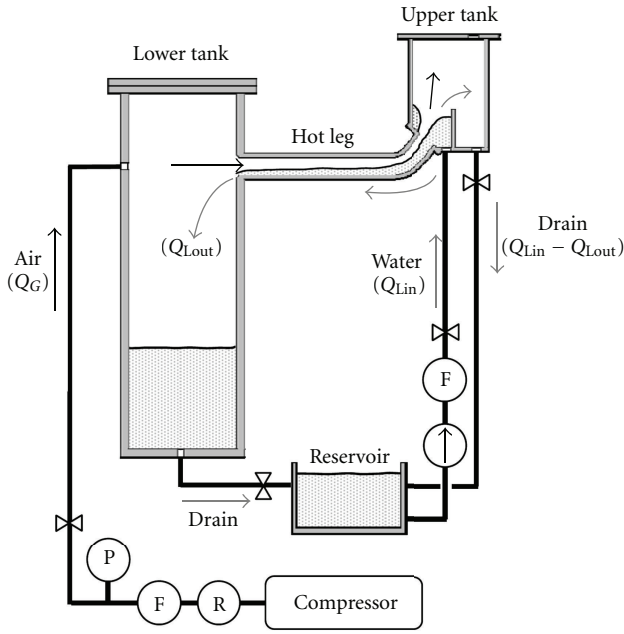
both under atmospheric pressure conditions. From his results, Ohnuki concluded that the flooding characteristics are independent from the fluid combination. Furthermore, he varied the most important geometrical aspects of the hot leg: the conduit diameter, the length of the straight pipes, and the angle of the riser. As a result of his investigations, Ohnuki proposed an empirical correlation to predict the onset of flooding by using the Wallis parameter, in which the y -intercept constant is a function of the length to diameter ratio of the horizontal pipe as well as of the length of the inclined riser.

Furthermore, steam/water CCFL experiments under increased pressure conditions were performed in the Upper Plenum Test Facility (UPTF), which simulates the primary circuit of a PWR at full scale. The experiments related by Weiss and Hertlein [5] simulate the reflux condenser mode after a small break LOCA. These were conducted at pressures of 3 and 15 bar and saturation conditions. A comparison of the results with the correlations of Richter et al. and Ohnuki confirmed that the Wallis parameter allows a proper geometrical scaling of the effects of counter-current flow limitation.

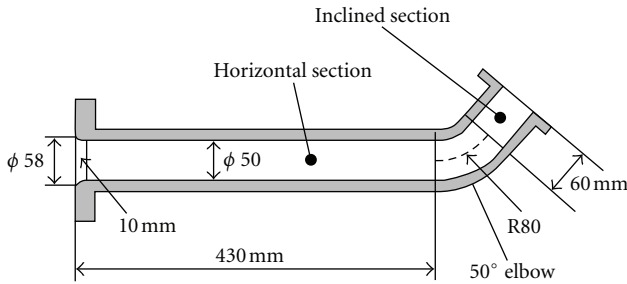
More recently, Kim and No [6] have merged in one database the experimental results obtained by eight different research groups, which were published between 1986 and 1999. The database includes cold air/water as well as steam/water experiments. By the regression through a total of 356 data points, Kim and No proposed a flooding correlation as function of the length to diameter ratio of the horizontal part of the hot leg. The prediction error of the correlation was evaluated against the considered database to 8.7%.

This brief review of the literature shows that previous investigations cover many aspects of the CCFL in hot leg typical geometries. However, the goal of most of the previous experiments was the development and validation of one-dimensional system codes. Therefore, the available data mainly focuses on macroscopic effects, which do not allow a detailed validation of the CFD codes. In fact, for comparison with CFD calculations, dedicated experimental data are needed with high resolution in space and time, for instance by the application of optical measuring techniques.

Such "CFD grade" experiments were recently performed at *Helmholtz-Zentrum Dresden-Rossendorf* (cf. Vallée et al. [7]). The structure of the two-phase flow was observed with a high-speed video camera in a model of the hot leg with rectangular cross-section at reactor typical boundary conditions (saturated steam/water at up to 50 bar and 264°C). However, the large scale of the test facility as well as the harsh boundary conditions unfortunately do not allow to observe the complete hot leg. Therefore, the complementary test facilities available at Kobe University were used for additional air/water experiments. The first results obtained in Kobe were reported by Minami et al. [8], including flow pattern maps, hysteresis effects between flooding and deflooding as well as the CCFL characteristics. Furthermore, Nariai et al. [9] investigated the influence of the fluid properties on the CCFL characteristics, varying the liquid phase viscosity with glycerol/water solutions.



P: pressure guage, F: flow meter, R: regulator
(a) scheme of the experimental setup



(b) hot leg test section

FIGURE 1: Hot leg test facility of Kobe University.

3. Experimental Setup and Procedure

Figure 1 shows a schematic of the experimental setup. It consists of the upper tank corresponding to the inlet plenum of a steam generator (SG), of the hot leg test section, and of the lower tank simulating the reactor pressure vessel (RPV). Furthermore, the experimental setup includes supply systems for the air and the liquid as well as a water reservoir. Details of the hot leg test section are shown in Figure 1(b). The hot leg consists of a horizontal section, a 50° elbow and an inclined section. It is scaled at 1 : 15 compared to the original nuclear power plant, corresponding to an inner diameter D of 50 mm. The dimensions of the separators are $L \times H \times W = 300 \times 1000 \times 100$ mm and $200 \times 160 \times 300$ mm for the lower and upper tank, respectively. The hot leg and the separators are made of transparent acrylic resin to allow optical observations.

Air is supplied from an oil-free compressor through a control valve and a flow meter (FLT-N, Flowcell, Ltd.) to the lower tank (cf. Figure 1(a)). The opening for the air is

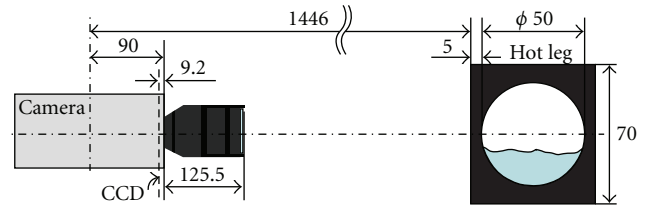


FIGURE 2: Cross-section of the hot leg pipe and position of the camera.

situated opposite to the one for the hot leg test section. The liquid (tap water) is injected to the bottom of the upper tank by a magnet pump via a flow meter (FLT-N, Flowcell, Ltd.) and flows through the test section into the lower tank. The experiments were performed at room temperature and atmospheric pressure, the air being discharged to the environment from the upper tank. The measuring uncertainties for the inlet superficial water velocity $j_{L,in}$ and for the superficial gas velocity j_G were estimated with 95% of confidence at $\pm 3.0\%$ and $\pm 2.5\%$, respectively.

The upper tank is divided into two parts by a 105 mm high weir placed at 110 mm of the left wall (cf. Figure 1(a)). This volume below the weir simulates the volume of the original steam generator inlet plenum. When CCFL occurs in the hot leg, the part of liquid which overflows the weir in the upper tank is drained into the reservoir. This design allows quasistationary counter-current flow limitation experiments. However, the separation area does not simulate the effects of the steam generator itself. In general, the water head in the upper tank does not significantly affect the CCFL characteristics. However, the fluctuation of the water head affects the fluctuation of pressure in the lower tank as well as the gas inlet flow rate into the hot leg. Consequently, this effect influences the CCFL characteristics due to a nonlinear behaviour. For further general information concerning this effect, please refer to the study by Navarro [10].

During the experiments, constant water and air flow rates were injected into the test facility. The air volume flow rate was varied from 0 to 15.7 L/s (corresponding to superficial gas velocities j_G in the pipe of 0 to 8 m/s) and the inlet water flow rate from 0.17 to 0.50 L/s (i.e., $j_{L,in} = 0.085, \dots, 0.25$ m/s). The experimental series were started with high air flow rates where CCFL is clearly established in order to avoid hysteresis effects (cf. Minami et al. [8]).

4. Optical Observations

Optical measurements were performed with a high-speed video camera. The flow was filmed from the side of the channel at 300 frames per second. Depending on the fluctuation of the flow structures over time, the recording time was varied between 20 and 30 s, leading to 6000 to 9000 images.

4.1. Image Scaling. As shown in Figure 2, the camera was placed at approximately 1.4 m from the channel. The settings lead to a spatial resolution of the images of about 2.2

pixel/mm (cf. example in Figure 5). In order to evaluate the distortion of the recorded images, the optical path was modelled from the camera objective to the hot leg model. As shown in the cross-sectional view (cf. Figure 2), the test section is not a pipe in a strict sense, it is a rectangular block of acrylic glass drilled in the centre. The result of the simulation is shown in Figure 3 for a half-filled test section and a distance between camera and channel outer wall of 100 mm. This short distance was chosen in order to intensify the optical refraction effects. Refractive indexes of 1.00, 1.333, and 1.49 were assumed for the air, the water, and the acrylic glass, respectively. As shown in Figure 3, the cross-section geometry corresponds to a divergent lens. However, due to the high index difference between air and acrylic glass, the divergence is more important in the empty part of the hot leg, compared to the domain filled with water. Furthermore, a part of the channel cannot be observed because of total reflection on the round acrylic glass interface.

Moreover, the model was used to evaluate the vertical distortion and resolution of the camera observation. Therefore, it was assumed that the bottom of the interface visible on the camera images corresponds to its left border in contact with the acrylic glass. In fact, due to the divergence of the test section, in the lower half of the channel a lower water level can only be observed if the interface is more concave than the inclination of the light path in water. As this does not apply for the upper half, a second optical path was simulated assuming that the bottom of the interface corresponds to the opposite border of the test section (curve “simulation 2” in Figure 4). Furthermore, the model allows to calculate the limit of total reflection from which the interface is visible on the image: 2.8 mm for the water and 8.4 mm for the air from the top or bottom of the pipe ($y = \pm 25$ mm in Figure 3), respectively.

In order to check the model, calibration measurements were performed before the CCFL experiments. Therefore, the test section was filled with a defined stratified water level and recorded with the high-speed video camera. The position of the interface in the camera images was plotted in function of the measured water level and compared with the simulation results in Figure 4. The simulated line was scaled linearly in pixels in function of the position of the top and bottom outer border of the test section (at $y = \pm 35$ mm, cf. Figure 2). As shown in Figure 4, the agreement between calibration measurements and simulation 1 is good, while simulation 2 gives wrong results. Consequently, this modelling shows that the bottom of the interface visible on the camera images corresponds to the left contact point between the channel and the air/water interface.

4.2. Image Processing Method. In order to capture the gas/liquid interface in the camera frames, an image processing algorithm was developed. As the top of the interface is difficult to identify automatically (in particular due to light reflexions on the water surface and to the background illumination differing for full and empty conditions), the current procedure detects its bottom limit. The principle of the capture method is illustrated in Figure 5 and consists in the following steps:

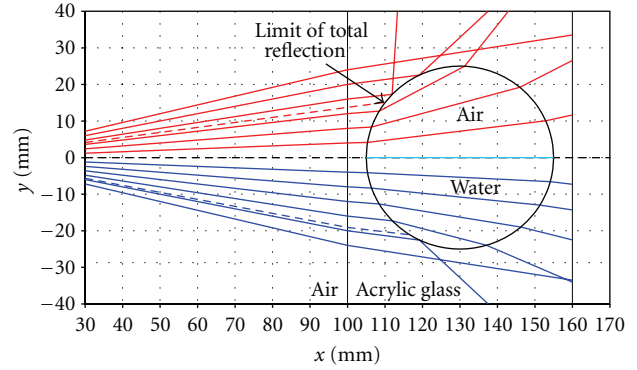


FIGURE 3: Scheme of the simulated optical path through the hot leg cross-section (distance between camera and channel outer wall: 100 mm).

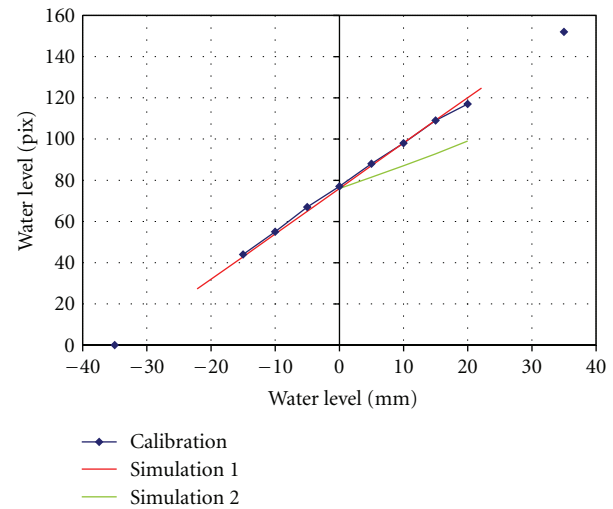


FIGURE 4: Vertical resolution of the optical observation: comparison between experimental calibration and simulation.

- (1) synthesis of a background image (bottom: full channel/top: empty channel, cf. Figure 5(b));
- (2) background subtraction (Figure 5(c));
- (3) calculation of a vertical gray level gradient over 3 pixels (top and bottom neighbours), cf. Figure 5(d);
- (4) searching for the maximum gradient in each vertical line (Figure 5(e));
- (5) filtering and detection of the wrong pixels:
 - (a) linear interpolation of single outlier with the neighbours (limit = 7 pixels),
 - (b) detection of the wrong group of pixels from their distance to the local moving average calculated over 10 neighbours to left and right (distance > 7 pixels);
- (6) correction of the wrong group of pixels:
 - (a) calculation of the linear interpolation line joining the last well detected pixels;

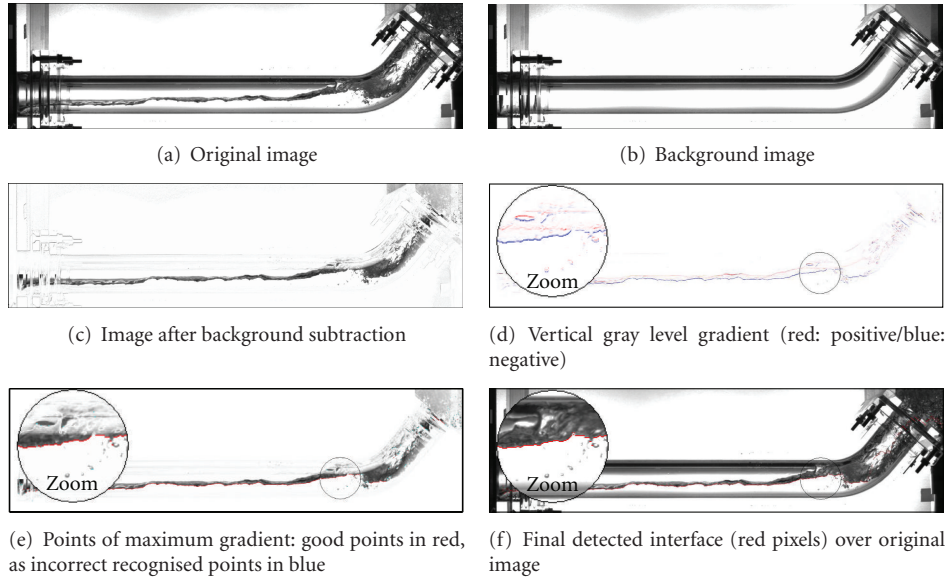


FIGURE 5: Visualisation of the main steps of the image processing (image taken during CCFL at $j_{L,in} = 0.25$ m/s and $j_G = 4.0$ m/s).

- (b) downweighting with a normal distribution weight function the gradient calculated in step (3) in function of the distance to the linear interpolation line;
- (c) researching for maximum gradient in the vertical line (Figure 5(f)).

As shown in Figure 5(f), the method gives very good results in the horizontal part of the hot leg. However, due to flanges and seals, the flow in the last part of the test section to the RPV simulator is only partially visible, disturbing the measurement in this region. Furthermore, in the riser to the SG tank, the low contrast between background and interface as well as the annular character of the flow leads to a largely incorrect detection. Consequently, the measurement results will not be analysed in these problematic regions hereafter.

5. Results

5.1. Water Level History. As an example, the experiment chosen to illustrate this section was performed at following boundary conditions:

- (i) water flow rate: 0.50 L/s (i.e., $j_{L,in} = 0.25$ m/s).
- (ii) air flow rate: 7.9 L/s (i.e., $j_G = 4.0$ m/s).

The water level in a cross-section as a function of time is obtained from the coordinates of the pixels detected in the high-speed camera images over a complete sequence. As an example, Figure 6 shows the resulting water level history for 7 chosen cross-sections identified by a colour on the picture above. The axial positions are indicated relatively to the inner wall of the lower tank (RPV simulator). Because the images are processed separately, few single outlier were observed in the time plot, which were averaged with the neighbours if the position difference was exceeding 5 pixels.

Along the horizontal part of the hot leg, wavy flow was observed during CCFL and, consequently, the water level presents relatively small fluctuations. The propagation direction of small waves is ambiguous, whereas some larger waves generated close to the bend pass through the hot leg to the lower tank (cf. arrow). In the bended region, the fluctuation of the water level is higher due to the water flow recirculation as well as slug generation, involving bubble formation. Here, the waves propagate in both directions, depending if the wave is high enough to grow unstably to a slug or not.

5.2. Probability Distribution of the Water Level

5.2.1. Calculation and Graphical Representation. As shown in previous section, the interface dynamics depends on the position in the test section. Therefore, a statistical approach is proposed in order to reflect the structure of the interface over time. The probability distribution of the water levels was calculated in each vertical cross-section for the complete measuring time (30.0 s, i.e., 9000 frames). As the image processing algorithm gives one single water level for each axial coordinate, the probability of the water levels measured at the pixel with the coordinates (x, y) is evident to calculate. The obtained probability distribution was represented according to a coloured scale and was superposed to the background picture in Figure 7. This shows relatively thin distributions with high probabilities in the horizontal part of the hot leg, especially close to the RPV simulator. In the direction of the bend, the probability expands due to the generation of larger waves and slugs as mentioned in previous section. The results in the problematic regions of the flange and seals close to RPV simulator as well as in the riser are questionable and should not be analysed. Consequently, these parts were not represented hereafter.

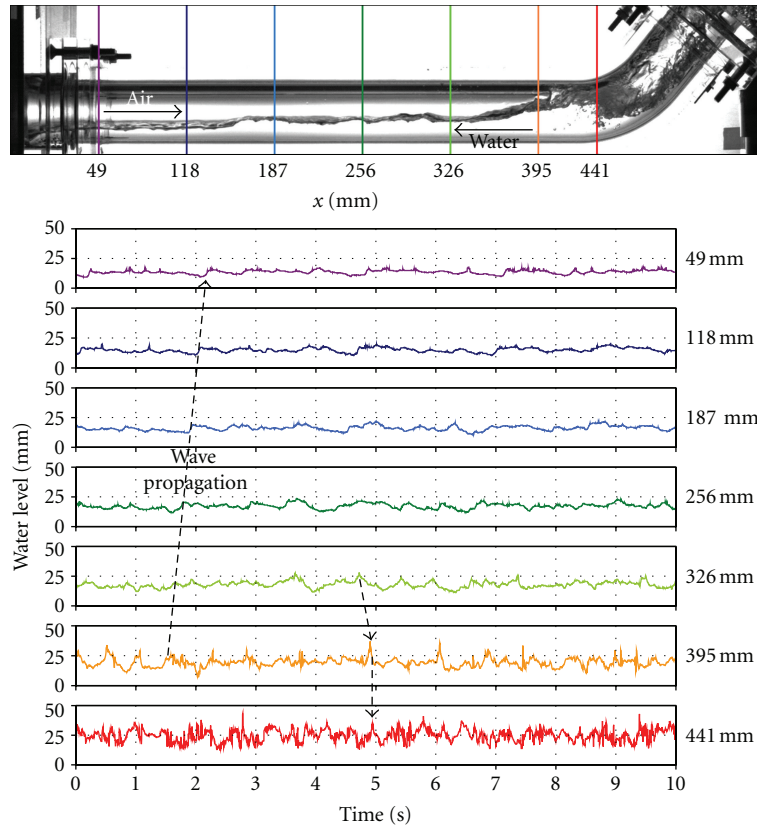


FIGURE 6: Time-dependent water level in chosen cross-sections during CCFL at $j_{L,in} = 0.25$ m/s and $j_G = 4.0$ m/s.

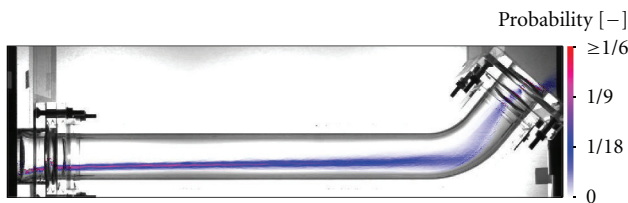


FIGURE 7: Visualisation of the probability distribution of the water level (colours) over the background picture (black and white)—CCFL at $j_{L,in} = 0.25$ m/s and $j_G = 4.0$ m/s.

5.2.2. Evolution of the Stratified Structure with the Boundary Conditions during CCFL. A series of experiments was performed at a constant injection of water corresponding to a superficial velocity of 0.25 m/s, while the air superficial velocity was varied from 0 to 8.0 m/s. The resulting visualisations of the probability distribution of the water level are shown in Figure 8. Without air flow rate (cf. Figure 8(a)), the water flow in the test section is supercritical ($Fr > 1$) because of the acceleration occurring down the riser. This explains why the water level increases in downstream direction due to the pressure drop. At air superficial velocities higher or equal to 1.0 m/s, CCFL is reached in the hot leg. According to the structure of the probability distribution, two different flow behaviours were observed.

(i) At low air flow rates (i.e., $1.0 \leq j_G \leq 2.0$ m/s), the probability distribution is broad, indicating a highly

fluctuating water level. These large fluctuations are due to the development of large liquid pockets obstructing the complete cross-section and expelled to the steam generator separator by the air flow. These structures originate from large water amounts intruding regularly into the hot leg from the upper tank and correspond to the oscillatory flow pattern described by Minami et al. [8]. This process occurring at relatively long time intervals, the water level in the hot leg decreases drastically in between of two water pockets, explaining the amplitude of the probability distribution.

(ii) At high air flow rate (i.e., $j_G \geq 4.0$ m/s), the water level is low and relatively stable with high probabilities. This is attributed to the frequent development of large waves or small slugs, which do not reach the top of the pipe, transporting the water back to the SG tank more continuously compared to the large liquid pockets.

At $j_G = 8.0$ m/s, the discharge liquid flow to the RPV simulator is null (i.e., zero liquid penetration). The stratified liquid in the horizontal pipe does not reach the lower exit, although it is longer than visible in the images due to the total reflexion effects (cf. Section 4.1). However, compared to previous CCFL conditions, the general structure of the interface is not affected by the zero liquid penetration.

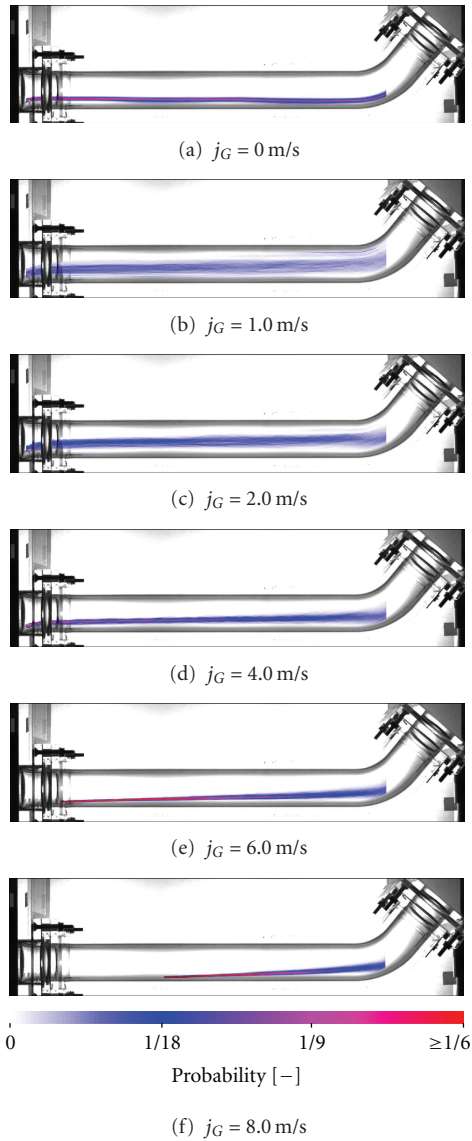


FIGURE 8: Evolution of the probability distribution of the water level in function of the air flow rate for experiments with $j_{L,in} = 0.25$ m/s.

Furthermore, series of experiments were performed to check the independency of the interface structure to the inlet water flow rate. As an example, the results obtained at a constant gas superficial velocity of 4.0 m/s and injected water superficial velocities of 0.085 to 0.25 m/s are shown in Figure 9. At these boundary conditions counter-current flow limitation is achieved in the hot leg. As expected, the probability distributions of the water level present no visible dependence on the injected water flow rate.

Moreover, for air superficial velocities higher than 4.0 m/s, the water level in the horizontal section presents an overall linear increase from left to right (cf. Figures 8 and 9). This result supports the assumption made to the water level in a simple CCFL model based on a momentum balance, which was proposed in the literature (Ohnuki et al. [4]).

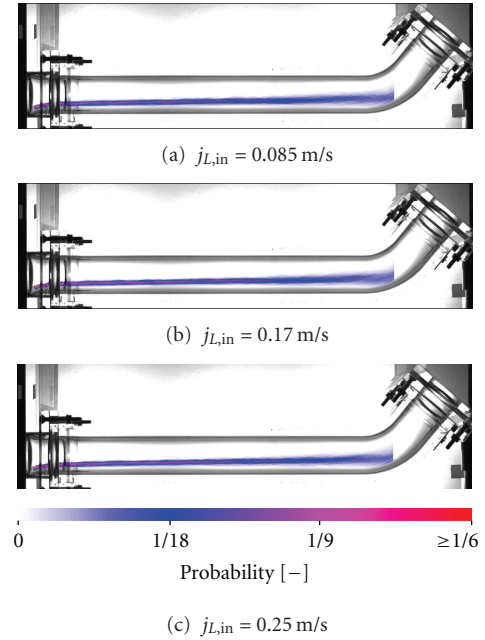


FIGURE 9: Evolution of the probability distribution of the water level in function of the injected water flow rate for experiments with $j_G = 4.0$ m/s.

6. Summary and Conclusions

In order to investigate the two-phase flow behaviour during counter-current flow limitation in the hot leg of a pressurised water reactor, dedicated experiments were performed in a scaled down model of Kobe University. The structure of the interface was observed from the side of the channel test section using a high-speed video camera. An algorithm was developed to recognise the stratified interface in the camera frames after background subtraction. This method allows extracting the water level at any location of the image as well as further statistical treatments. The evolution of the water level along the horizontal part of the hot leg in function of the liquid and gas flow rates was shown.

It was found that the flow structure during CCFL depends on the flow regime in the hot leg: at low gas velocities large liquid pockets were observed, while at high flow rates the formed slugs are smaller but more frequent. This effect influences the amplitude of the water level fluctuations significantly. Furthermore, the probability distributions of the water level present no visible difference in function of the injected water flow rate. Finally, at high air flow rates, the water level in the horizontal section was found to follow an overall linear trend, as assumed by simple models developed to predict CCFL.

The achieved high-resolution data and especially the visualisation of the probability distribution are of great use for the analysis of the flow conditions as well as for the validation of modelling approaches, in particular computational fluid dynamics (CFDs). Consequently, this new quality of data can help to better understand the processes governing counter-current flow limitation.

Acknowledgments

This work was realised within the frame of a PROMOS Scholarship of the Technische Universität Dresden found by the DAAD (German Academic Exchange Service) and received by the main author. This paper was presented in original form at the 14th International Topical Meeting on Nuclear Reactor Thermalhydraulics (NURETH-14), September 25–30, 2011, Toronto, ON, Canada.

References

- [1] H. J. Richter, G. B. Wallis, K. H. Carter, and S. L. Murphy, “Deentrainment and counter-current air-water flow in a model PWR hot leg,” Tech. Rep. NRC-0193-9, U.S. Nuclear Regulatory Commission Report, Hanover, NH, USA, 1978.
- [2] G. B. Wallis, *One-Dimensional Two-Phase Flow*, Mc Graw-Hill, New York, NY, USA, 1969.
- [3] S. M. Krolewski, *Flooding Limits in a Simulated Nuclear Reactor Hot Leg*, Massachusetts Institute of Technology, Cambridge, Mass, USA, 1980.
- [4] A. Ohnuki, “Experimental study of counter-current two-phase flow in horizontal tube connected to inclined riser,” *Journal of Nuclear Science and Technology*, vol. 23, no. 3, pp. 219–232, 1986.
- [5] P. A. Weiss and R. J. Hertlein, “UPTF test results: first three separate effect tests,” *Nuclear Engineering and Design*, vol. 108, no. 1-2, pp. 249–263, 1988.
- [6] H. T. Kim and H. C. No, “Assessment of RELAP5/MOD3.2.2y against flooding database in horizontal-to-inclined pipes,” *Annals of Nuclear Energy*, vol. 29, no. 7, pp. 835–850, 2002.
- [7] C. Vallée, T. Seidel, D. Lucas et al., “Counter-current flow limitation experiments in a model of the hot leg of a pressurised water reactor—comparison between high pressure steam/water experiments and low pressure air/water experiments,” in *Proceedings of the 13th International Topical Meeting on Nuclear Reactor Thermal Hydraulics (NURETH-13)*, Kanazawa, Japan, 2009, Paper no. 13P1107.
- [8] N. Minami, D. Nishiwaki, T. Nariai, A. Tomiyama, and M. Murase, “Countercurrent gas-liquid flow in a PWR hot leg under reflux cooling (I) air-water tests for 1/15-scale model of a PWR hot leg,” *Journal of Nuclear Science and Technology*, vol. 47, no. 2, pp. 142–148, 2010.
- [9] T. Nariai, A. Tomiyama, C. Vallée, D. Lucas, and M. Murase, “Counter-current flow limitation in a scale-down model of a PWR hot leg,” in *Proceedings of the 8th International Topical Meeting on Nuclear Thermal-Hydraulics, Operation and Safety (NUTHOS-8)*, Shanghai, China, 2010, Paper no. 8P0109.
- [10] M. A. Navarro, “Study of countercurrent flow limitation in a horizontal pipe connected to an inclined one,” *Nuclear Engineering and Design*, vol. 235, no. 10–12, pp. 1139–1148, 2005.

Research Article

Numerical Simulation of Size Effects on Countercurrent Flow Limitation in PWR Hot Leg Models

I. Kinoshita,^{1,2} M. Murase,¹ and A. Tomiyama²

¹*Institute of Nuclear Technology, Institute of Nuclear Safety System, Inc., 64 Sata, Mihama-cho, Mikata-gun, Fukui 919-1205, Japan*

²*Department of Mechanical Engineering, Graduate School of Engineering, Kobe University, 1-1 Rokkodai, Nada-ku, Kobe 657-8501, Japan*

Correspondence should be addressed to I. Kinoshita, kinoshita@inss.co.jp

Received 10 January 2012; Revised 6 March 2012; Accepted 6 March 2012

Academic Editor: Thomas Hoehne

Copyright © 2012 I. Kinoshita et al. This is an open access article distributed under the Creative Commons Attribution License, which permits unrestricted use, distribution, and reproduction in any medium, provided the original work is properly cited.

We have previously done numerical simulations using the two-fluid model implemented in the CFD software FLUENT6.3.26 to investigate effects of shape of a flow channel and its size on CCFL (countercurrent flow limitation) characteristics in PWR hot leg models. We confirmed that CCFL characteristics in the hot leg could be well correlated with the Wallis parameters in the diameter range of $0.05 \text{ m} \leq D \leq 0.75 \text{ m}$. In the present study, we did numerical simulations using the two-fluid model for the air-water tests with $D = 0.0254 \text{ m}$ to determine why CCFL characteristics for $D = 0.0254 \text{ m}$ were severer compared with those in the range, $0.05 \text{ m} \leq D \leq 0.75 \text{ m}$. The predicted CCFL characteristics agreed with the data for $D = 0.0254 \text{ m}$ and indicated that the CCFL difference between $D = 0.0254 \text{ m}$ and $0.05 \text{ mm} \leq D \leq 0.75 \text{ mm}$ was caused by the size effect and not by other factors.

1. Introduction

Reflux condensation by steam generators (SGs) is considered as one of the possible core cooling methods under hypothetical accident conditions in pressurized water reactors (PWRs). During the reflux condensation, the water condensed in SG U-tubes has to flow countercurrent to the steam generated in the reactor core. The core cooling performance heavily depends on the occurrence of countercurrent flow limitation (CCFL) in the hot leg which consists of a horizontal pipe, an elbow, and an inclined pipe. As reviewed by Al Issa and MacLan [1], many experiments have been conducted to investigate the CCFL characteristics in the hot leg, and empirical correlations have been proposed using Wallis parameters [2]. The review showed that many differences between CCFL data were simply due to geometrical effects. To compare CCFL characteristics in hot leg models, Vallée et al. [3] selected three geometrical factors: the horizontal pipe length to diameter ratio (L_H/D), the inclined pipe length to diameter ratio (L_I/D), and the elbow angle θ . They showed that even for similar geometrical factors, there was clear

deviation between CCFL characteristics due to size effects. In order to evaluate effects of size better, numerical simulation using CFD (computational fluid dynamics) software is expected to be useful.

In order to investigate effects of shape of a flow channel and its size on CCFL characteristics in hot leg models, we have previously done numerical simulations using a two-fluid model implemented in the CFD software FLUENT6.3.26 [4–6]. We found that the two-fluid model could reproduce CCFL characteristics under low-pressure conditions, and we confirmed that those in the hot leg could be well correlated with the Wallis parameters in the region of $0.05 \text{ m} \leq D \leq 0.75 \text{ m}$ [6]. On the other hand, CCFL characteristics for $D = 0.0254 \text{ m}$ measured by Ohnuki et al. [7] were severer compared with those in the range $0.05 \text{ m} \leq D \leq 0.75 \text{ m}$.

In this paper, we did numerical simulations using the two-fluid model for the air-water tests ($D = 0.0254 \text{ m}$) conducted by Ohnuki et al. [7] to evaluate whether the CCFL difference between $D = 0.0254 \text{ m}$ and $0.05 \text{ m} \leq D \leq 0.75 \text{ m}$ is because of the size effect or other factors.

TABLE 1: Test section dimensions and conditions.

Reference	D (m)	L_H/D (-)	L_I/D (-)	θ (deg)	Fluids	Pressure (MPa)
Ohnuki et al. [7]	0.0254	9.1	1.2	50	Air-water	0.1
Richter et al. [8]	0.2032	4.5	0	45	Air-water	0.1
Mayinger et al. [9]	0.750	9.0	1.1	50	Steam-water	0.3, 1.5
Geffraye et al. [10]	0.351	7.5	3.0	50	Air-water	0.1
Navarro [11]	0.054	9.3	1.9	50	Air-water	0.1
Minami et al. [12]	0.050	8.4	1.2	50	Air-water	0.1

D : diameter, L_H : length of horizontal pipe, L_I : length of inclined pipe, θ : angle of elbow.

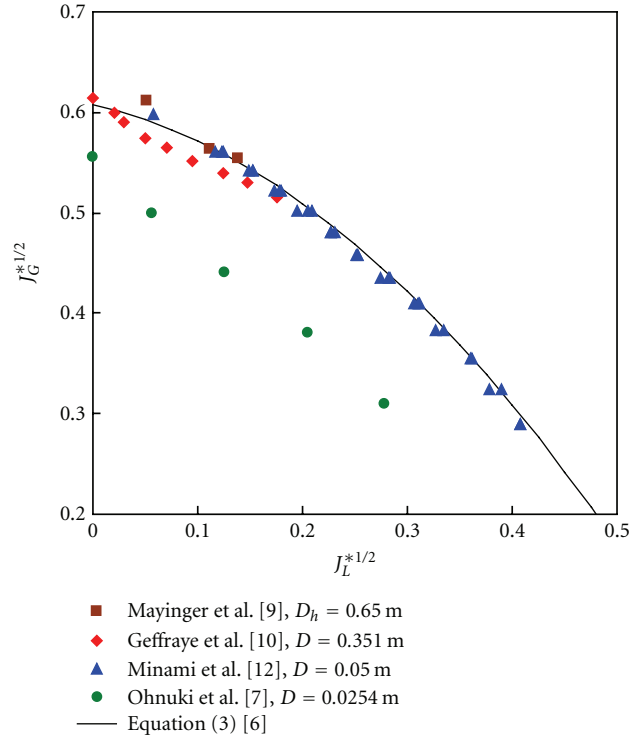


FIGURE 1: CCFL characteristics.

2. CCFL Characteristics in a Hot Leg Geometry

CCFL characteristics in a PWR hot leg are generally expressed by using the Wallis correlation or Wallis parameters which are respectively defined by [2]

$$(J_G^*)^{1/2} + m(J_L^*)^{1/2} = C, \quad (1)$$

$$J_k^* = J_k \left\{ \frac{\rho_k}{g \cdot \ell \cdot (\rho_L - \rho_G)} \right\}^{1/2}, \quad (2)$$

$\ell = D \text{ or } H$ ($k = G \text{ or } L$),

where J (m/s) is the volumetric flux in the hot leg, m and C are empirical constants, ℓ (m) is the characteristic length, D (m) is the diameter of the hot leg, H (m) is the height of a hot leg model with a rectangular channel, g (m/s²) is the gravity acceleration, and ρ (kg/m³) is the density.

Al Issa and MacIain [1] classified CCFL data according to the horizontal pipe length to diameter ratio into four

groups: (L_H/D) = 0–5, 5–10, 10–25, and >40. Vallée et al. [3] selected experimental studies using the horizontal pipe length to diameter ratio of (L_H/D) = 7–10 to compare CCFL characteristics in hot leg models. Major test conditions in previous studies are listed in Table 1. The empirical constant C in (1) by Richter et al. [8] was about 0.7, and CCFL was mitigated compared with other cases where C was about 0.6, because the horizontal pipe length to diameter ratio (L_H/D) was small.

Figure 1 compares the CCFL data listed in Table 1. The solid line in Figure 1 was an empirical correlation obtained by fitting the data of the 1/15-scale test given by [6]

$$(J_G^*)^{1/2} = 0.608 - 0.238(J_L^*)^{1/2} - 1.28(J_L^*). \quad (3)$$

In the UPTF tests (Mayinger et al. [9]), the diameter of the hot leg was $D = 0.75$ m, and the hydraulic diameter in the region with the ECC (emergency core cooling) injection tube was $D_h = 0.65$ m. As can be seen in Figure 1, there

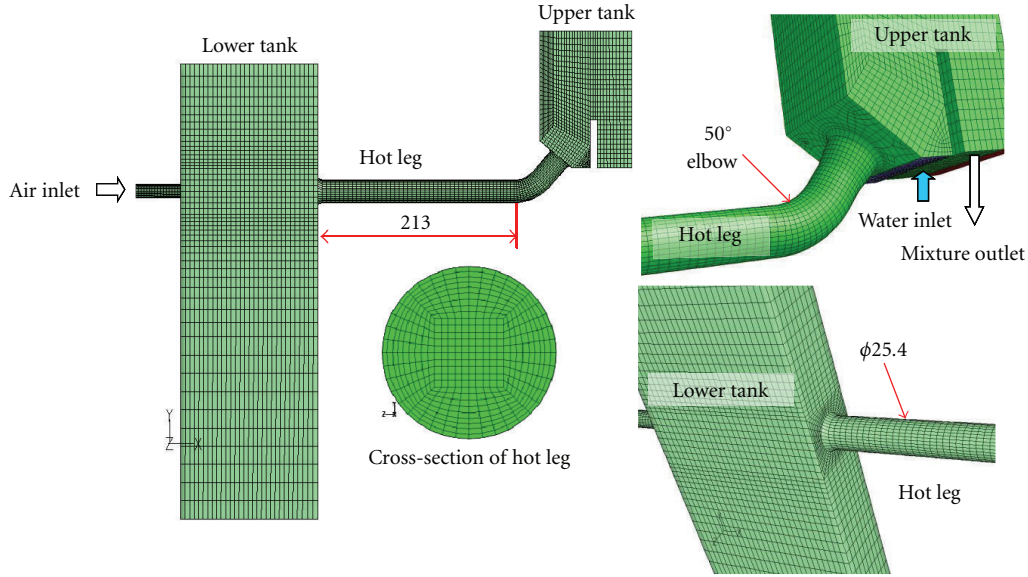


FIGURE 2: Computational grids (unit: mm).

were no significant differences between CCFL characteristics obtained under conditions of $0.05 \text{ m} \leq D \leq 0.75 \text{ m}$. However, the empirical constant C by Ohnuki et al. [7] was about 0.55, and CCFL became severer compared with other cases. The objective of this study was to evaluate the reason why CCFL for $D = 0.0254 \text{ m}$ became severer.

3. Simulation Method

In the numerical simulations, the two-fluid model and the standard $k-\varepsilon$ turbulence model implemented in FLU-ENT6.3.26 were used. Conservation equations for momentum, volume fraction, turbulent kinetic energy, and turbulent dissipation rate of the gas and liquid phases were solved using the first-order upwind scheme, because calculations with the second-order upwind scheme became unstable. The phase-coupled-SIMPLE method was used for the pressure-velocity coupling.

3.1. Computational Grid. Figure 2 shows the computational grid for the air-water tests with the $D = 0.0254 \text{ m}$ [7], which was reduced from the computational grid for a full-scale PWR hot leg [6]. Because velocity distributions of gas and liquid at both ends of the hot leg affect hydraulic behavior, the calculation region included the lower tank simulating the upper plenum in the reactor vessel and the upper tank simulating the SG inlet plenum. There were 460 calculation cells in the cross-section of the hot leg and about 120,000 calculation cells in total. The diameter of the hot leg and the length of the horizontal pipe were $D = 0.0254 \text{ m}$ and $L_H = 0.213 \text{ m}$ ($L_H/D = 8.4$). The length of the tapered section was not included in the length of the horizontal pipe (including the tapered section, $L_H/D = 8.6$). (L_H/D) in the computational grid was a little smaller than that ($L_H/D = 9.1$) in the tests conducted by Ohnuki et al. [7].

Gas was supplied from the side wall into the lower tank and flowed into the upper tank through the hot leg. Water was supplied from the bottom of the upper tank. Some water gravitationally flowed into the lower tank through the hot leg. The water flow rate through the hot leg was calculated from the increasing rate of water volume in the lower tank. The boundary condition of constant velocity was used at the inlets of gas and water, and the boundary condition of constant pressure was used at the outlet of the gas-water mixture.

3.2. Interfacial Drag Coefficient. In the two-fluid model, we implemented the interfacial drag coefficients as a user function of FLUENT. In the momentum equation, the interfacial drag force F_i (N/m^3) is defined by

$$F_i = -\frac{1}{2} C_D A_i \rho_G |u_r| u_r, \quad (4)$$

where u_r (m/s) is the relative velocity between the gas and liquid phases and A_i (m^2/m^3) is the interfacial area concentration. We used a combination of the following three correlations of the interfacial drag coefficients ($C_D A_i$) as a function of local void fraction α [4]:

$$C_D A_i = \min[(C_D A_i)_L, \max\{(C_D A_i)_M, (C_D A_i)_H\}], \quad (5)$$

$$(C_D A_i)_L = 2\alpha(1-\alpha)g/V_{gi}^2, \quad (6)$$

$$(C_D A_i)_M = 9.8(1-\alpha)^3(4.5\alpha/D_h), \quad (7)$$

$$(C_D A_i)_H = 0.02\{1 + 75(1-\alpha)\}\alpha^{0.5}/D_h, \quad (8)$$

where D_h (m) is the hydraulic diameter. Equation (6) was originally proposed by Andersen [13] for one-dimensional two-phase flow, and Minato et al. [14] applied it to three-dimensional calculations. Equations (7) and (8) are based

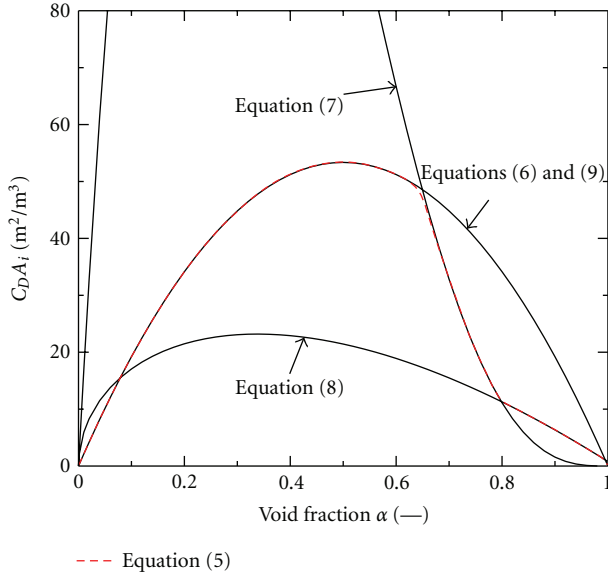


FIGURE 3: Interfacial drag coefficients ($D_h = 0.0254$ m).

on correlations for slug flow [15] and annular flow [2], respectively. Equation (7) was simplified from the original correlation by Ishii and Mishima [15] using $\alpha_{gs} = 0$, where α_{gs} is void fraction of small bubbles. In (6), drift velocity V_{gj} (m/s) for stagnant liquid, which was simplified from the original correlation [16], was used:

$$V_{gi} = 1.4(D_h^*)^{0.125} \left\{ \frac{g\sigma(\rho_L - \rho_G)}{\rho_L^2} \right\}^{1/4}, \quad (9)$$

$$D_h^* = D_h \left\{ \frac{g(\rho_L - \rho_G)}{\sigma} \right\}^{1/2},$$

where σ (N/m) is the surface tension.

The combination of (5) through (9) was verified by numerical simulations [4–6] for the 1/5-scale rectangular channel tests and the 1/15-scale circular channel tests conducted at Kobe University and the full-scale UPTF tests [9]. The two-fluid model with the combination of (5) through (9) could reproduce CCFL characteristics under low pressure conditions. In this study, the two-fluid model with the combination of (5) through (9) and the computational grid shown in Figure 2 were used in numerical simulations conducted for the air-water tests with the diameter of 0.0254 m. In order to evaluate the size effect, the simulated results were compared with the data [7] as well as the simulated results for $D = 0.05$ m [5] and 0.75 m [6], which were predicted by the same method used in this study except for size.

Figure 3 shows the interfacial drag coefficients ($C_D A_i$) calculated using (5) through (9) for the air-water system at 0.1 MPa with the diameter of 0.0254 m. Equations (7) and (8) are functions of void fraction and the hydraulic diameter. These are inversely proportional to the hydraulic diameter. On the other hand, (6) is a function of void fraction and drift velocity, which depends on fluid properties as expressed by (9). However, the effect of fluid properties on (6) is not large.

4. Results and Discussion

4.1. Flow Patterns. Figure 4 shows predicted flow patterns for $D = 0.0254$ m compared with a flow pattern observed in the Ohnuki experiments ($D = 0.0254$ m) [7] versus flow patterns observed [12] and predicted [4] for the 1/15-scale air-water tests ($D = 0.05$ m). Under CCFL conditions in the Ohnuki experiments, an instable roll wave grew near the elbow in the horizontal section. Some roll waves grew up, and those waves were blown up to the upper tank by air upflow. The depth of the water layer near the agitated region was thicker than that near the lower tank. The predicted flow patterns for $D = 0.0254$ m were quite similar to the observed ones. At higher J_G , a water slug fell through the inclined section, where the two flows combined and formed a roll wave near the elbow, and CCFL took place at the junction of the elbow and the horizontal section. The water flow was mainly limited at this location. Accordingly, the water depth was the highest at the junction and decreased toward the lower tank. As J_G decreased, water depth in the horizontal section became higher, and the falling water flow rate through the hot leg became larger.

As shown in Figures 4(c) and 4(d), the above mentioned findings about flow patterns for $D = 0.0254$ m were almost the same as the observed and predicted flow patterns for the 1/15-scale hot leg model ($D = 0.05$ m). Thus, there was no qualitative difference between the flow patterns for $D = 0.0254$ m and $D = 0.05$ m.

4.2. CCFL Characteristics. Figure 5 shows the predicted CCFL characteristics for $D = 0.0254$ m compared with the CCFL data measured by Ohnuki et al. [7]. The zero liquid penetration limits (i.e., CCFL constants C of the Wallis correlation, (2)) agreed very well with each other. On the other hand, the numerical simulation slightly underestimated the slope m of the CCFL correlation compared with the measured data [7]. This may be due to the difference of (L_H/D) between the two hot leg models.

Figure 5 also shows the CCFL characteristics predicted by the two-fluid model for the 1/15-scale hot leg model [5] as well as a full-scale hot leg model [6]. The geometric characteristics of these hot leg models are summarized in Table 2. As can be seen in Figure 5, the CCFL characteristics were well correlated with the Wallis parameters for $0.05 \text{ m} \leq D \leq 0.75 \text{ m}$, and the best-fit CCFL correlation was expressed by (3). However, the present predicted CCFL characteristics for $D = 0.0254$ m were severer compared with those for $0.05 \text{ m} \leq D \leq 0.75 \text{ m}$, which were predicted by the same calculation model and method except for size. It follows from these results that the measured CCFL difference between $D = 0.0254$ m and $0.05 \text{ m} \leq D \leq 0.75 \text{ m}$ was caused by the size effect and not by other factors.

4.3. Discussion. In the experiments, there are many differences such as specification and characteristics of the test facility and test section, test methods and conditions, and measurements and data evaluation methods, which may affect CCFL characteristics. Therefore, it is very important to

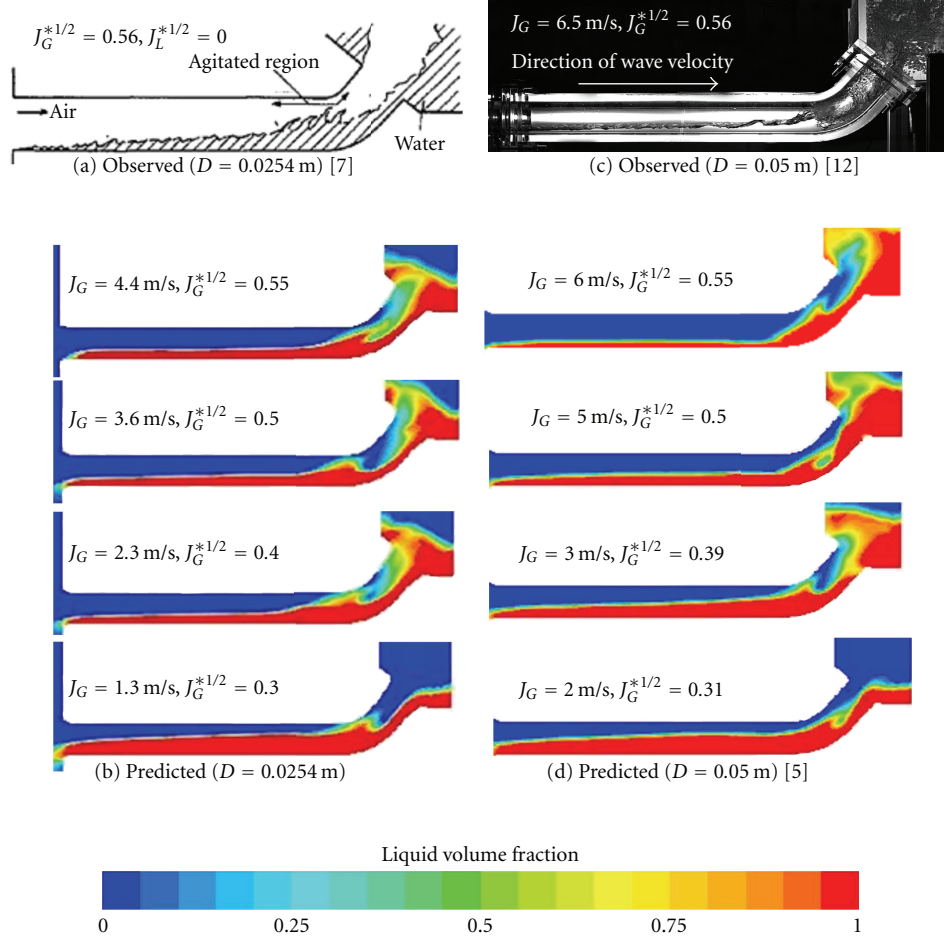


FIGURE 4: Predicted flow patterns.

TABLE 2: Test section dimensions and experimental and simulation conditions.

Reference	D (m)	L_H/D (-)	L_I/D (-)	θ (deg)	Fluids	Pressure (MPa)
<i>Experiments</i>						
Ohnuki et al. [7]	0.0254	9.06	1.18	50	Air-water	0.1
<i>Simulations</i>						
Present study	0.0254	8.40	1.20	50	Air-water	0.1
Minami et al. [5]	0.05	8.40	1.20	50	Air-water	0.1
Kinoshita et al. [6]	0.75	8.40	1.20	50	Air-water and steam-water	0.1

D : diameter, L_H : length of horizontal pipe, L_I : length of inclined pipe, θ : angle of elbow.

reproduce the trend of test results by numerical simulations using the same calculation model and schemes to verify numerical methods and also confirm test results.

In Figure 6, the CCFL constants C for hot leg models listed in Tables 1 and 2 were arranged according to diameters D or hydraulic diameters D_h of the cross-sections. For the UPTF data (Mayinger et al. [9]), the inner diameter without Hutze ($D = 0.75$ m) as well as the hydraulic diameter at the location of Hutze ($D_h = 0.65$ m) were used as the characteristics lengths of Wallis parameters, (2). Judging from the experiments of Ohnuki et al. [7], the CCFL constant for $D =$

0.75 m without Hutze was estimated to be between the UPTF data for $D = 0.75$ m and $D_h = 0.65$ m. As shown in Figure 6, the CCFL constants of the measurements for $D_h \geq 0.05$ m were almost the same and approximately 0.61 on average.

Accordingly, the CCFL constant for a real PWR hot leg ($D = 0.75$ m) was estimated to be 0.61, which agreed well with 0.608 in (3). On the contrary, for small hydraulic diameters ($D_h = 0.0254$ m), the CCFL constants became small (i.e., CCFL became severe). As can be seen by comparing the simulation results with measured results, the two-fluid model simulation well reproduced the CCFL

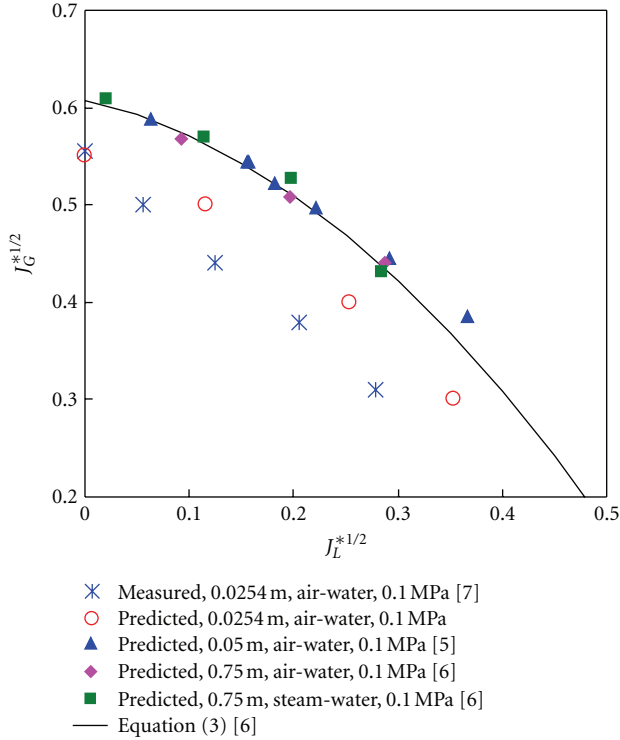


FIGURE 5: Predicted CCFL characteristics.

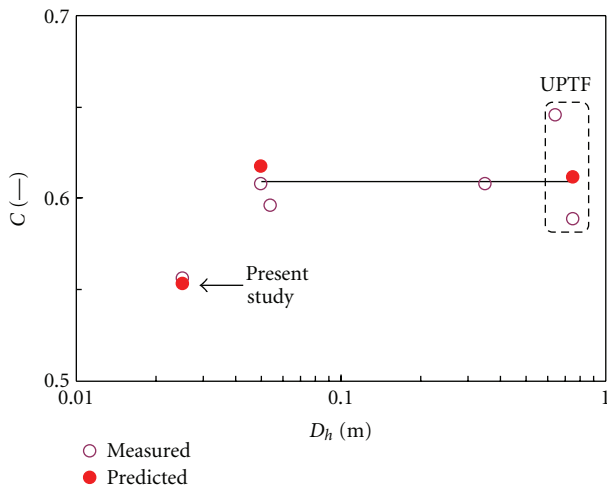


FIGURE 6: CCFL constants arranged by hydraulic diameters.

constants of hot leg models in the wide range of $D_h = 0.0254$ m to 0.75 m.

5. Conclusions

In order to evaluate whether the CCFL difference between $D = 0.0254$ m and 0.05 m is because of the size effect or other factors, we did numerical simulations using the two-fluid model for the air-water tests ($D = 0.0254$ m) conducted by Ohnuki et al.

The numerical simulations well reproduced the flow patterns observed in the air-water test ($D = 0.0254$ m) and the measured discrepancy in the CCFL constants seen between $D = 0.0254$ m and $0.05 \text{ m} \leq D \leq 0.75$ m. This indicated that the CCFL difference between $D = 0.0254$ m and $0.05 \text{ m} \leq D \leq 0.75$ m was caused by the size effect and not by the other factors.

References

- [1] S. Al Issa and R. Maclan, "A review of CCFL phenomenon," *Annals of Nuclear Energy*, vol. 38, no. 9, pp. 1795–1819, 2011.
- [2] G. B. Wallis, *One-dimensional Two-phase Flow*, McGraw Hill, New York, NY, USA, 1969.
- [3] C. Vallée, T. Seidel, D. Lucas, A. Tomiyama, and M. Murase, "Comparison of counter-current flow limitation experiments performed in two different models of the hot leg of a pressurized water reactor with rectangular cross-section," *Journal of Engineering for Gas Turbines and Power*, vol. 133, article 052917, 2011.
- [4] N. Minami, M. Murase, D. Nishiwaki, and A. Tomiyama, "Countercurrent Gas-Liquid Flow in a Rectangular Channel Simulating a PWR Hot Leg (2) Analytical Evaluation of Countercurrent Flow Limitation," *Japanese Journal of Multiphase Flow*, vol. 22, no. 4, pp. 413–422, 2008 (Japanese).
- [5] N. Minami, M. Murase, and A. Tomiyama, "Countercurrent gas-liquid flow in a PWR hot leg under reflux cooling (II) numerical simulation of 1/15-scale air-water tests," *Journal of Nuclear Science and Technology*, vol. 47, no. 2, pp. 149–155, 2010.
- [6] I. Kinoshita, M. Murase, Y. Utanohara, N. Minami, and A. Tomiyama, "Numerical simulation of countercurrent gas-liquid flow in a PWR hot leg under reflux cooling," *Journal of Nuclear Science and Technology*, vol. 47, no. 10, pp. 963–972, 2010.
- [7] A. Ohnuki, H. Adachi, and Y. Muraio, "Scale effects on countercurrent gas-liquid flow in a horizontal tube connected to an inclined riser," *Nuclear Engineering and Design*, vol. 107, no. 3, pp. 283–294, 1988.
- [8] H. J. Richter, G. B. Wallis, K. H. Carter, and S. L. Murphy, "Deentrainment and Countercurrent Air-water Flow in a Model PWR Hot-leg, NRC-0193-9," U. S. Nuclear Regulatory Commission, 1978.
- [9] F. Mayinger, P. Weiss, and K. Wolfert, "Two-phase flow phenomena in full-scale reactor geometry," *Nuclear Engineering and Design*, vol. 145, no. 1-2, pp. 47–61, 1993.
- [10] G. Geffraye, P. Bazin, P. Pichon, and A. Bengaouer, "CCFL in hot legs and steam generators and its prediction with the CATHARE code," in *Proceedings of the 7th International Topical Meeting on Nuclear Reactor Thermal Hydraulics (NURETH '95)*, pp. 815–826, Saratoga Springs, NY, USA, September 1995.
- [11] M. A. Navarro, "Study of countercurrent flow limitation in a horizontal pipe connected to an inclined one," *Nuclear Engineering and Design*, vol. 235, no. 10–12, pp. 1139–1148, 2005.
- [12] N. Minami, D. Nishiwaki, T. Nariai, A. Tomiyama, and M. Murase, "Countercurrent gas-liquid flow in a PWR hot leg under reflux cooling (I) air-water tests for 1/15-scale model of a PWR hot leg," *Journal of Nuclear Science and Technology*, vol. 47, no. 2, pp. 142–148, 2010.

- [13] J. G. M. Andersen, "Interfacial shear for two-fluid models," *American Nuclear Society Transactions*, vol. 41, pp. 669–671, 1982.
- [14] A. Minato, K. Takamori, and N. Ishida, "An extended two-fluid model for interface behavior in gas-liquid two-phase flow," in *Proceedings of the 8th International Conference on Nuclear Engineering (ICONE '00)*, Baltimore, Md, USA, 2000.
- [15] M. Ishii and K. Mishima, "Two-fluid model and hydrodynamic constitutive relations," *Nuclear Engineering and Design*, vol. 82, no. 2-3, pp. 107–126, 1984.
- [16] Y. Kataoka, H. Suzuki, and M. Murase, "Drift-flux parameters for upward gas flow in stagnant liquid," *Journal of Nuclear Science and Technology*, vol. 24, no. 7, pp. 580–586, 1987.

Research Article

Countercurrent Flow Limitation at the Junction between the Surge Line and the Pressurizer of a PWR

Taiga Doi,¹ Takashi Futatsugi,¹ Michio Murase,² Kosuke Hayashi,¹ Shigeo Hosokawa,¹ and Akio Tomiyama¹

¹Department of Mechanical Engineering, Faculty of Engineering, Kobe University, 1-1 Rokkodai, Nada, Kobe, Hyogo 657-8501, Japan

²Institute of Nuclear Technology, Institute of Nuclear Safety System, Inc. (INSS), 64 Sata, Mihama, Fukui 919-1205, Japan

Correspondence should be addressed to Akio Tomiyama, tomiyama@mech.kobe-u.ac.jp

Received 13 October 2011; Revised 17 January 2012; Accepted 19 January 2012

Academic Editor: Deendarlianto

Copyright © 2012 Taiga Doi et al. This is an open access article distributed under the Creative Commons Attribution License, which permits unrestricted use, distribution, and reproduction in any medium, provided the original work is properly cited.

An experimental study on countercurrent flow limitation (CCFL) in vertical pipes is carried out. Effects of upper tank geometry and water levels in the upper and lower tanks on CCFL characteristics are investigated for air-water two-phase flows at room temperature and atmospheric pressure. The following conclusions are obtained: (1) CCFL characteristics for different pipe diameters are well correlated using the Kutateladze number if the tank geometry and the water levels are the same; (2) CCFL occurs at the junction between the pipe and the upper tank both for the rectangular and cylindrical tanks, and CCFL with the cylindrical tank occurs not only at the junction but also inside the pipe at high gas flow rates and small pipe diameters; (3) the flow rate of water entering into the vertical pipe at the junction to the rectangular upper tank is lower than that to the cylindrical tank because of the presence of low frequency first-mode sloshing in the rectangular tank; (4) increases in the water level in the upper tank and in the air volume in the lower tank increase water penetration into the pipe, and therefore, they mitigate the flow limitation.

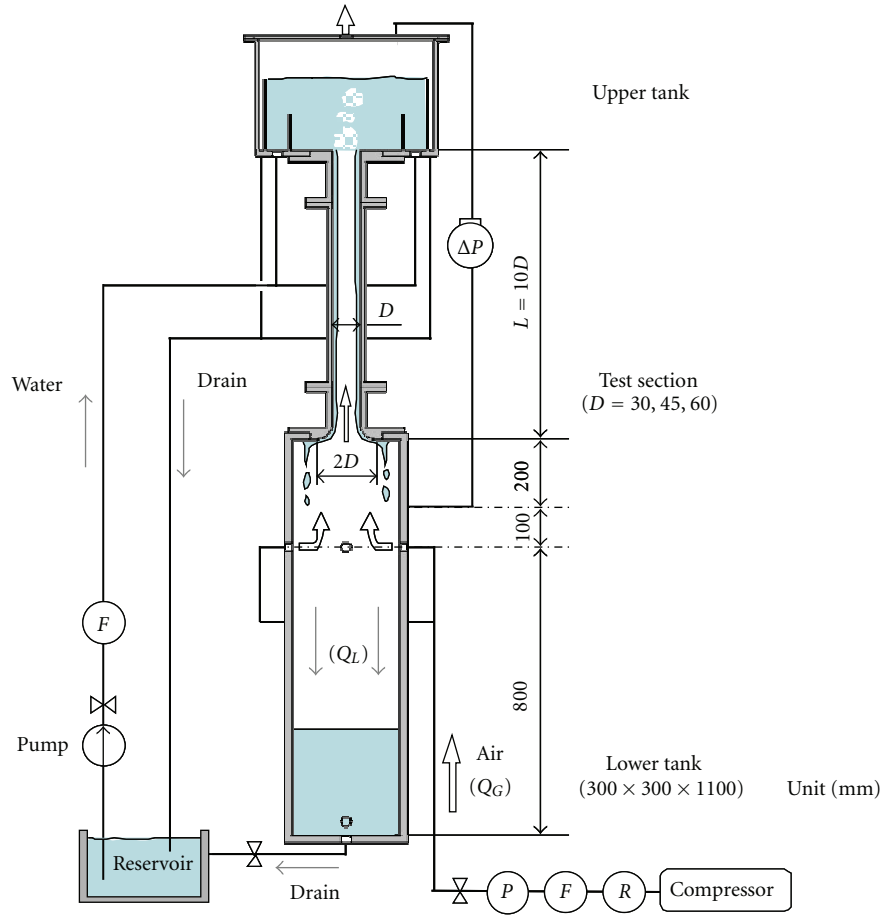
1. Introduction

During a PWR plant outage for maintenance and refueling, the reactor coolant is cooled by a residual heat removal (RHR) system. For a certain period, the reactor coolant level is kept around the primary loop center in order to carry out operations like aeration, attachment, or detachment of the steam generator (SG) nozzle dam. This operation mode is called mid-loop operation. If a failure of the RHR system occurs during the mid-loop operation, there is a possibility of boiling of the reactor coolant. One of the effective methods to cool the reactor core in this event is reflux cooling by the SG. During the reflux condensation, steam generated in the reactor core and water condensed in a pressurizer due to heat transfer to its vessel wall may form a countercurrent flow in a surge line connecting the hot leg and the pressurizer. The ROSA-IV/LSTF (Rig-of-Safety-Assessment No. 4/Large Scale Test Facility) experiment [1] for the loss of RHR systems during mid-loop operation showed that water accumulates in the pressurizer due to the limitation of liquid flow in the

countercurrent flow in the surge line. Thus, understanding the characteristics of countercurrent flow limitation (CCFL) in the surge line is of great importance for safety evaluation of the mid-loop operation.

In our previous study [2], countercurrent flow limitation (CCFL) in a scale-down model of a PWR surge line, which consists of a vertical pipe and an inclined pipe with several elbows, was investigated by measuring the relationship between the water and gas flow rates in the surge line. The relationship is referred to as CCFL characteristics. The CCFL takes place at three locations in the experiments, that is, at the junction between the vertical pipe and the bottom of the pressurizer, in the inclined pipe and at the junction between the inclined pipe and the hot leg. The CCFL characteristics strongly depend on the location of CCFL. The experiments imply that the CCFL at the junction between the vertical pipe and the bottom of the pressurizer plays an important role in the actual surge line under the reflux cooling.

Many studies on CCFL in vertical pipes have been carried out [3–11] using the experimental apparatus consisting of a



P: Pressure gage
F: Flowmeter

R: Regulator
 ΔP : Differential pressure transducer

FIGURE 1: Experimental setup.

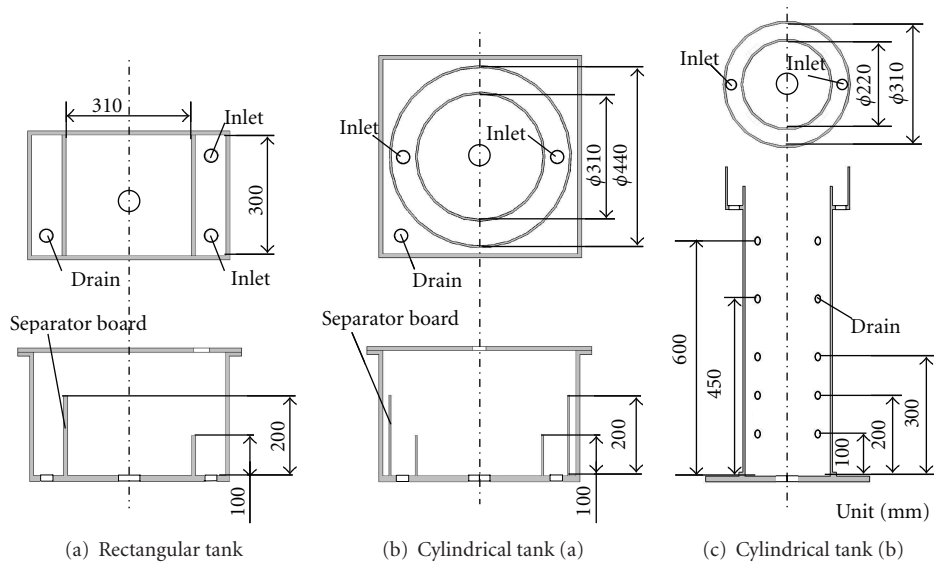
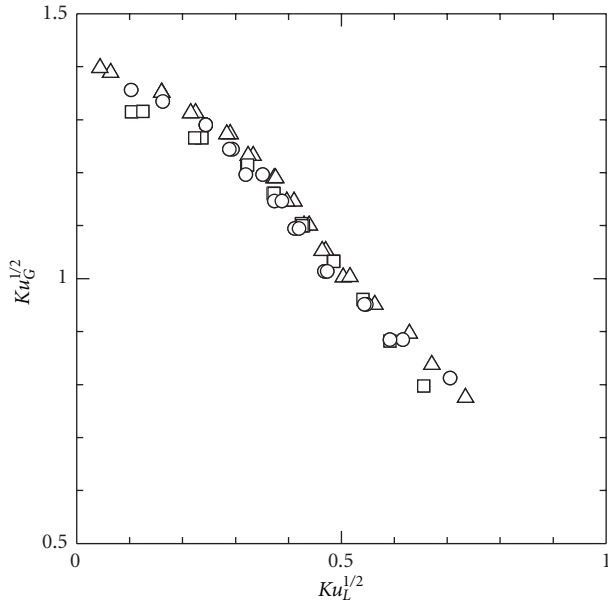
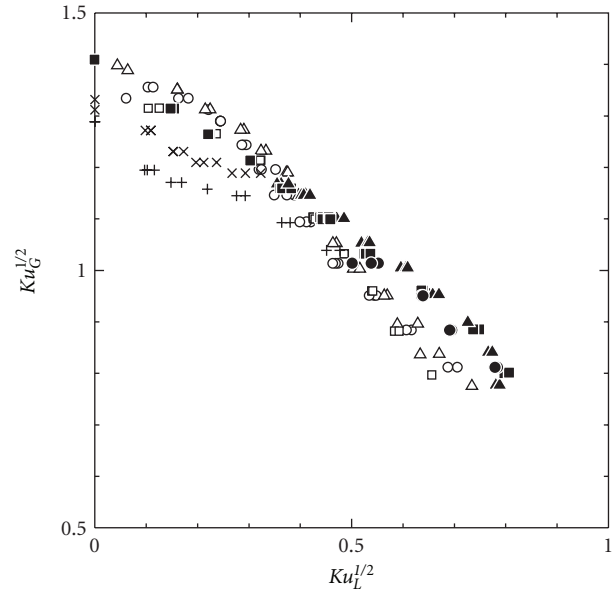


FIGURE 2: Upper tanks.

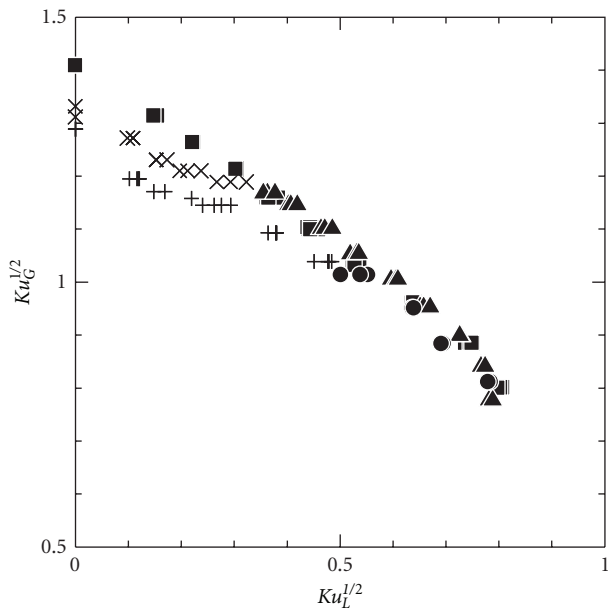


CCFL-U	D
○	30 mm
△	45 mm
□	60 mm

(a) Rectangular tank



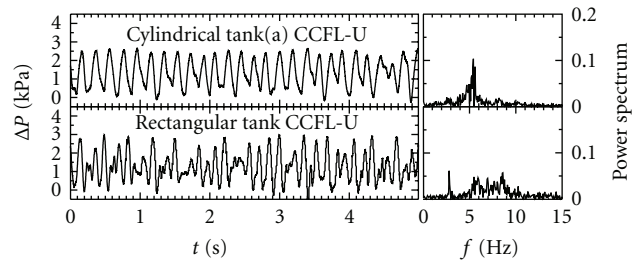
Cylindrical tank (a)		Rectangular tank	
CCFL-U	D	CCFL-U	D
●	30 mm	○	30 mm
▲	45 mm	△	45 mm
■	60 mm	□	60 mm
CCFL-P			
+	30 mm		
×	45 mm		



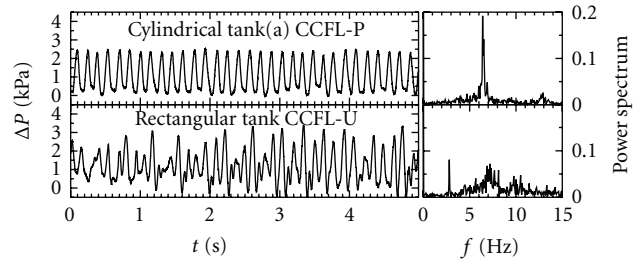
CCFL-U	D	CCFL-P	D
●	30 mm	+	30 mm
▲	45 mm	×	45 mm
■	60 mm		

(b) Cylindrical tank (a)

FIGURE 5: Effects of upper tank geometry on CCFL characteristics.



(a) $J_G = 4.8 \text{ m/s}$ ($Ku_G^{1/2} = 1.00$)



(b) $J_G = 7.3 \text{ m/s}$ ($Ku_G^{1/2} = 1.23$)

FIGURE 4: CCFL characteristics for rectangular and cylindrical tanks on $Ku_G^{*1/2} - Ku_L^{*1/2}$ plane.

FIGURE 6: Pressure difference ΔP between upper and lower tanks ($D = 45 \text{ mm}$).

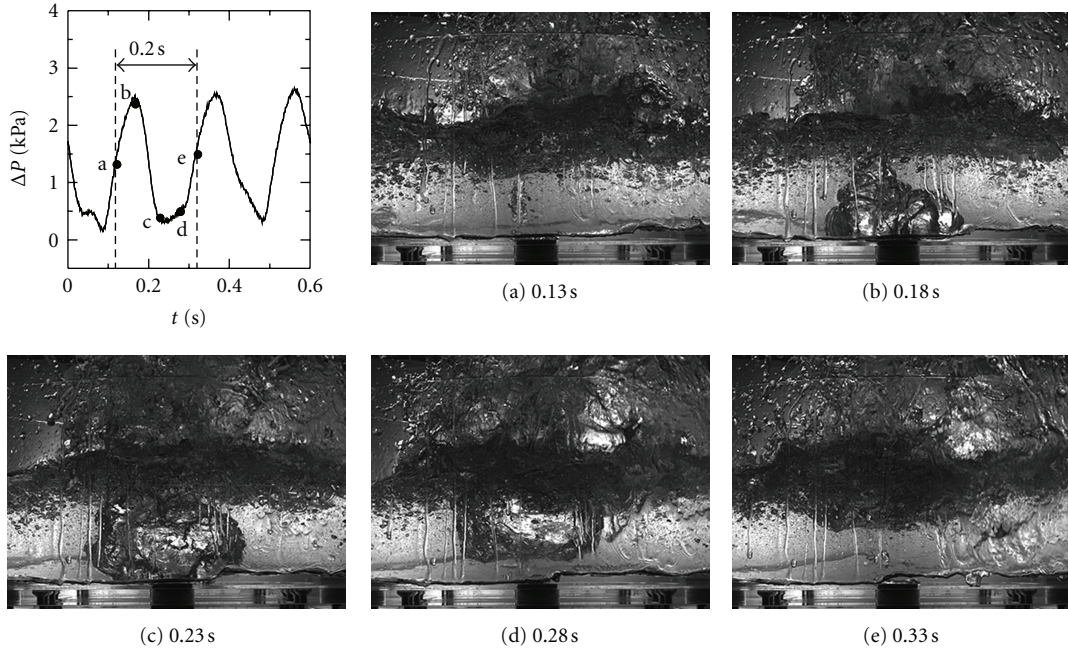


FIGURE 7: Bubble generation process in the cylindrical tank (a) ($J_G = 4.9$ m/s, $J_G^{*1/2} = 0.50$, $Ku_G^{1/2} = 1.0$, and $D = 45$ mm).

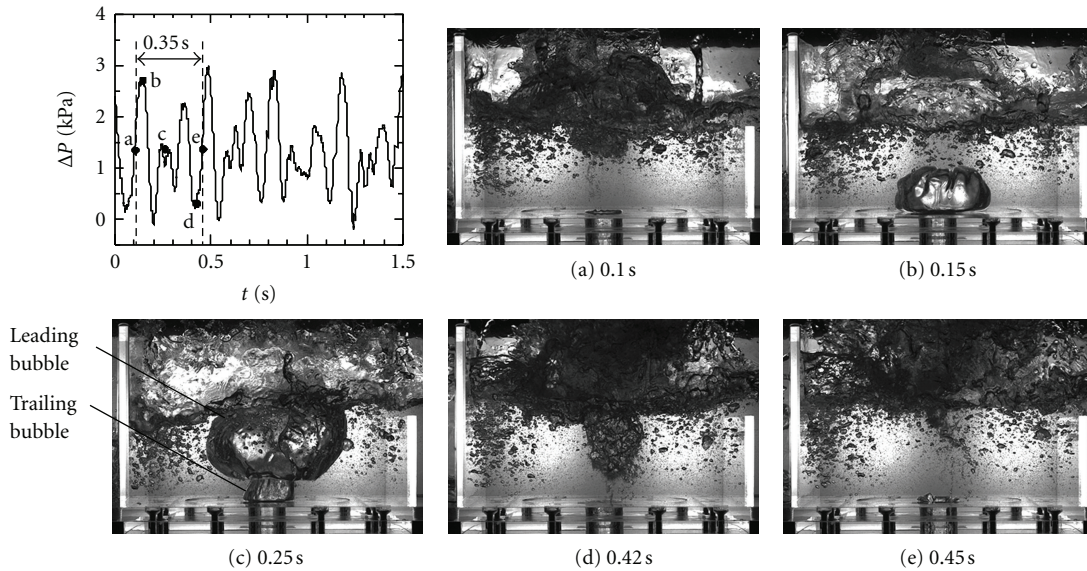


FIGURE 8: Bubble generation process in the rectangular tank ($J_G = 4.9$ m/s, $J_G^{*1/2} = 0.50$, $Ku_G^{1/2} = 1.0$, and $D = 45$ mm).

holes on its wall at various elevations. The drain holes used in each experiment were changed to test various water levels in the upper tank.

2.2. Experimental Method

2.2.1. CCFL Characteristics. CCFL characteristics were investigated by measuring the time-averaged flow rate, Q_L , of water entering into the lower tank at constant gas flow rates, Q_G . The Q_L was calculated from the rise speed of water level

in the lower tank. The ranges of the liquid and gas volume fluxes, J_L and J_G , tested were $0 \leq J_L \leq 0.118$ m/s and $2.40 \leq J_G \leq 16.4$ m/s, respectively, where J_L and J_G are defined by

$$J_k = \frac{Q_k}{A} \quad (k = L, G). \quad (1)$$

Here A is the cross-sectional area of the vertical pipe and the subscripts L and G denote the liquid and gas phases, respectively. The uncertainties in measured J_L and J_G estimated at 95% confidence were $\pm 3.0\%$ and $\pm 2.5\%$, respectively.

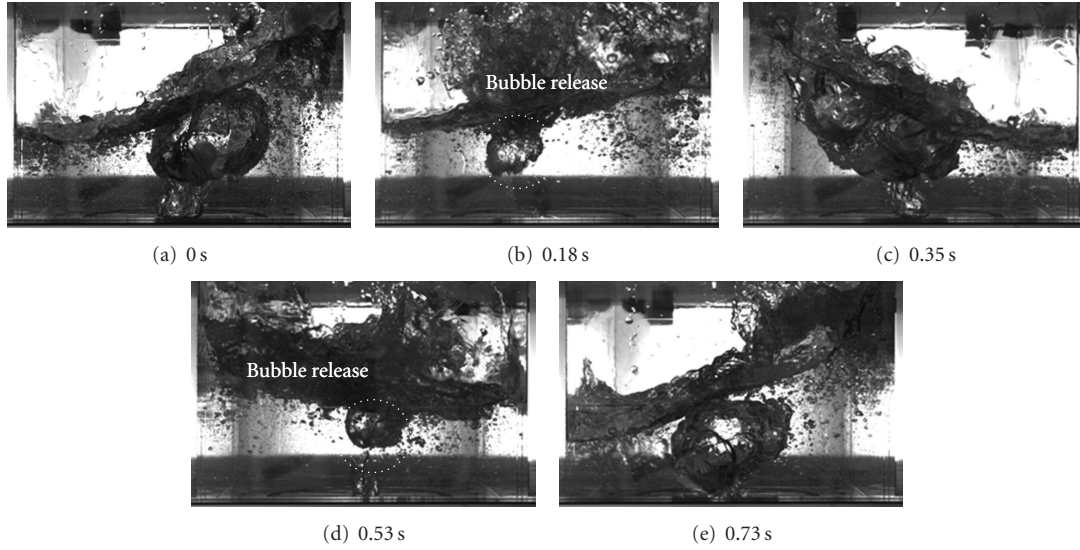


FIGURE 9: First-mode sloshing in the rectangular tank ($J_G = 7.7$ m/s, $J_G^{*1/2} = 0.70$, $Ku_G^{1/2} = 1.3$, and $D = 30$ mm).

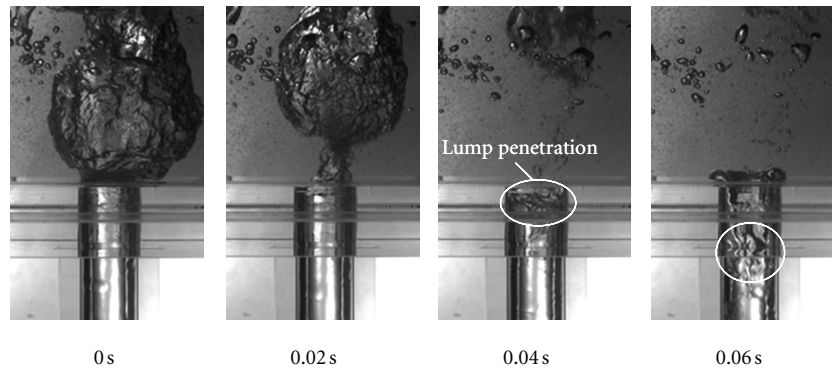


FIGURE 10: Relation between bubble release and water penetration ($J_G = 5.8$ m/s, $J_G^{*1/2} = 0.60$, $Ku_G^{1/2} = 1.1$, and $D = 30$ mm).

2.2.2. Pressure Difference. The pressure difference ΔP ($=P_{\text{Lower}} - P_{\text{Upper}}$, where P_{Lower} and P_{Upper} are the pressures in the lower and upper tanks, resp.) was measured using a differential pressure transducer (DP45, Valydine, Ltd. natural frequency > 600 Hz). It was connected between the top of the upper tank and the side wall of the lower tank as shown in Figure 1. The sampling rate was 1.0 kHz, and the measurement time was 30 seconds. The uncertainty in measured ΔP was less than 0.5% of the full scale (6 kPa). Flows in the upper tank were observed by using a high-speed video camera (Dantec Dynamics, Nano sence Mk3) to understand the relation between ΔP and the flow behavior in the upper tank. The frame rate was 100 fps and the recording time was 30 s.

3. Results and Discussion

3.1. Effects of Upper Tank Geometry. Flow visualization with the high-speed video camera showed that, under all the test conditions, the CCFL with the rectangular tank occurred only at the junction between the vertical pipe and the upper tank, that is, some water flows into the pipe from the upper

tank, but the remaining water does not and returns to the reservoir, and then the water entering the pipe forms liquid film and flows down to the lower tank without flooding in the pipe. This CCFL taking place at the upper junction is referred to as CCFL-U. The CCFL characteristics measured using the rectangular tank are plotted in Figure 3(a), where J_L^* and J_G^* are the Wallis parameters [14] defined by

$$J_k^* = J_k \left[\frac{\rho_k}{gD(\rho_L - \rho_G)} \right]^{1/2} \quad (k = L, G), \quad (2)$$

where ρ is the density, g the acceleration of gravity and D the pipe diameter. At constant J_G^* , J_L^* becomes smaller with increasing D , that is, the flow limitation becomes stronger. Figure 3(b) shows the CCFL characteristics for the cylindrical tank (a). The CCFL occurs only at the junction at low J_G^* , whereas at high J_G^* and $D \leq 45$ mm, some water penetrating into the vertical pipe intermittently flowed back into the upper tank due to flooding, that is, the CCFL occurs not only at the junction but also inside the pipe. This CCFL is referred to as CCFL-P. Thus, the CCFL characteristics clearly

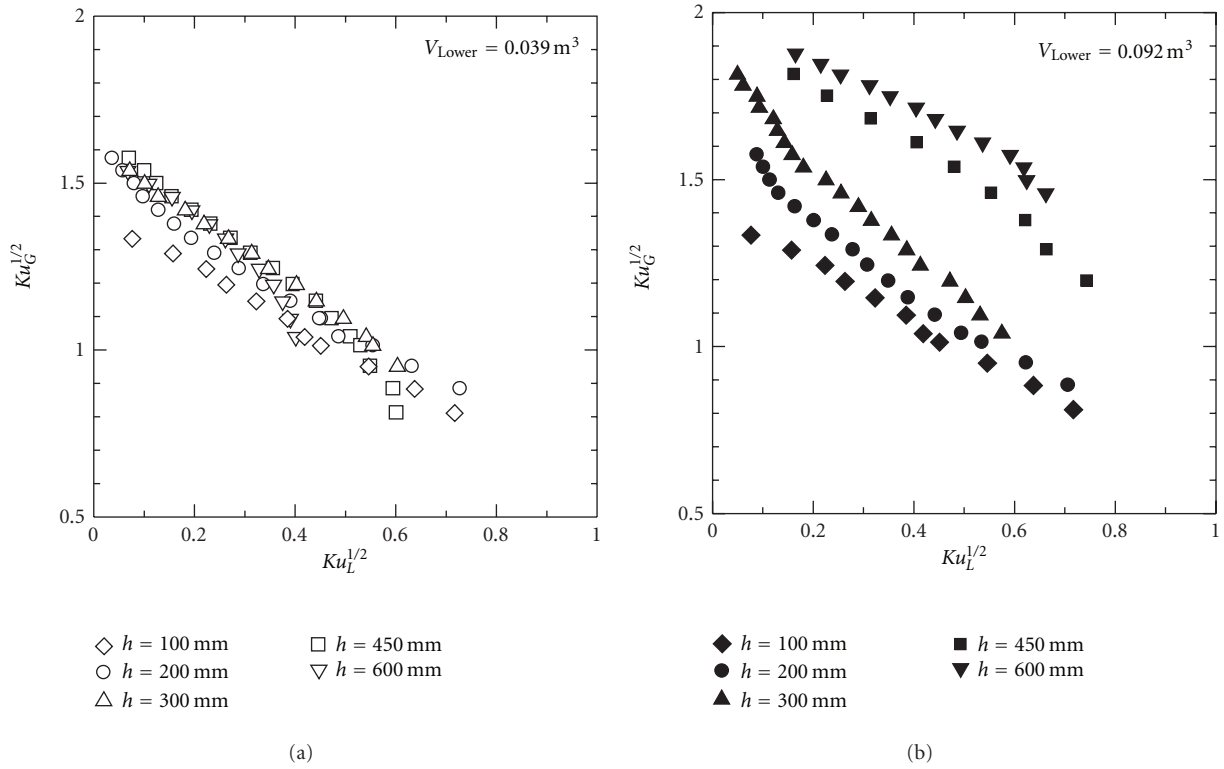


FIGURE 11: Effects of water level, h , in upper tank on CCFL characteristics ($D = 30 \text{ mm}$).

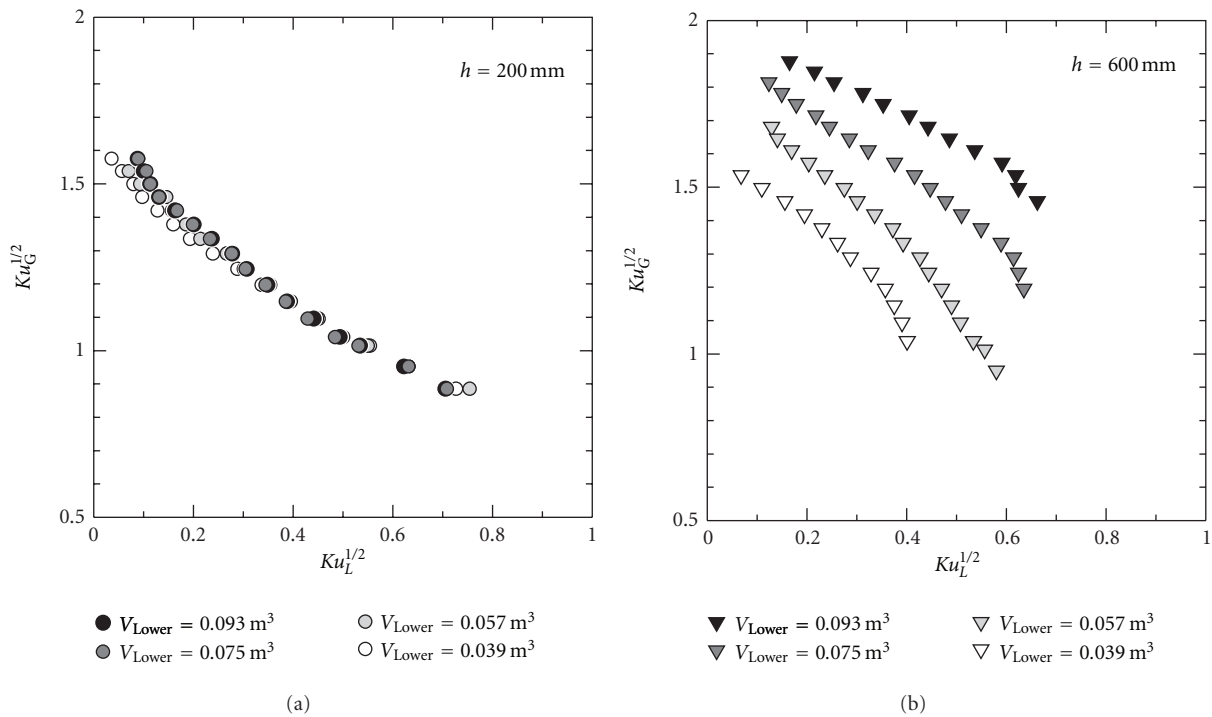


FIGURE 12: Effects of air volume, V_{Lower} , in lower tank on CCFL characteristics ($D = 30 \text{ mm}$).

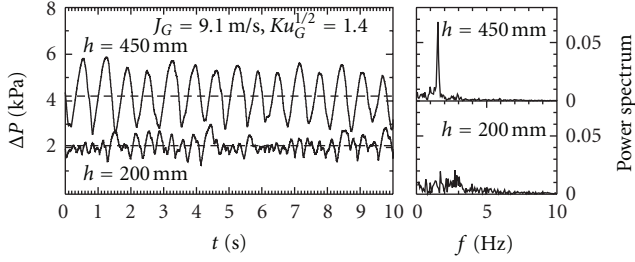


FIGURE 13: Pressure difference ΔP between upper and lower tanks (Cylindrical tank (b), $D = 30$ mm, $V_{\text{Lower}} = 0.092$ m³ and $J_G = 9.1$ m/s).

depend on the pipe diameter and the location where CCFL takes place.

Richter [7] and Jayanti et al. [15] suggested that, for prediction of flooding, the Wallis parameter, J^* , is appropriate for small diameter pipes, whereas the Kutateladze number, Ku , [16] is better for large diameter pipes. Vijayan et al. [17] carried out flooding experiments using vertical pipes of $D = 25$, 67, and 99 mm and confirmed that J^* is better for small D (25 mm), whereas Ku is better for large D (67 and 99 mm). The Kutateladze number is defined by

$$Ku_k = J_k \left[\frac{\rho k^2}{g\sigma(\rho_L - \rho_G)} \right]^{1/4} \quad (k = L, G), \quad (3)$$

where σ is the surface tension. The Wallis parameter includes D but the Kutateladze number does not. Therefore, the pipe diameter plays an important role in flooding for small D , whereas the mechanism of flooding is less dependent on D in large pipes. The CCFL characteristics are replotted on the $Ku_L^{1/2} - Ku_G^{1/2}$ plane as shown in Figure 4. The CCFL characteristics for different pipe diameters are well correlated with the Kutateladze numbers both for the rectangular and cylindrical tanks when the CCFL occurs only at the junction (CCFL-U). Therefore, the diameter effect on the CCFL characteristics is not so significant in these cases. The CCFL characteristics for the two tanks are compared in Figure 5. The flow limitation with the cylindrical tank (a) is stronger than that with the rectangular tank at high Ku_G because of the CCFL occurrence inside the pipe. On the other hand, at low Ku_G , the CCFL with the rectangular tank is stronger. This will be discussed later based on the observation of bubble motions in the upper tanks.

Figure 6 shows the pressure differences, ΔP , for the cylindrical and rectangular tanks and their power spectrums obtained by the fast Fourier transform analysis. The pressure fluctuations for the cylindrical tank (a) mainly consist of waves in the range of 5–7 Hz. On the other hand, those for the rectangular tank consist of single peaks at 3 Hz and broad peaks in the range of 5–10 Hz. Figure 7 shows a typical bubble generation process in the cylindrical tank (a) and ΔP at $J_G = 4.9$ m/s and $D = 45$ mm. There is no bubble at the junction at $t = 0.13$ s. The ΔP increases as a bubble starts to be generated at the junction until $t = 0.18$ s. The ΔP then decreases as the bubble grows for $t = 0.18$ –0.23 s. The bubble is released from the junction at $t = 0.28$ s, and then, the next

bubble starts to be generated at 0.33 s. The period and the frequency of this process are about 0.20 s and 5 Hz, which corresponds to the peak frequency.

A bubble generation process in the rectangular tank at $J_G = 4.9$ m/s and $D = 45$ mm is shown in Figure 8. The ΔP increases as the bubble grows at the junction for $t = 0.10$ –0.15 s. For $t > 0.15$ s, a trailing bubble is formed behind the leading bubble. The fluctuation of ΔP for $0.15 < t < 0.42$ s must be due to these trailing bubbles. The next leading bubble starts to grow at $t = 0.45$ s. The period of the generation of leading bubbles is 0.35 s. The single peak at 3 Hz and the broad peak in the range of 5–10 Hz in Figure 5, therefore, correspond to the leading-bubble generation cycle and the fluctuation due to the trailing bubbles, respectively. The first mode sloshing shown in Figure 9 was observed only for the rectangular tank. The free surface in the tank took the maximum inclination at $t = 0$ s as shown in Figure 9(a). Then the water moved to the left side, and the bubble was detached from the junction due to water movement in the horizontal direction (Figure 9(b)). Two leading bubbles were released during one period of the sloshing (Figures 9(a)–9(e)). The natural frequency of the first mode sloshing in a two-dimensional rectangular tank is given by [18]

$$f = \frac{\sqrt{gk \tanh kH}}{2\pi} \quad \left(k = \frac{\pi}{L} \right), \quad (4)$$

where H is the height of the free surface and L the width of the tank. According to (4), the frequency for the rectangular tank used is 1.53 Hz, which is about half of the bubble release frequency. The bubble release frequency is, therefore, strongly governed by the sloshing in the tank.

Figure 10 shows images of flows in the rectangular tank and the pipe. Water lump penetrated into the pipe when a bubble detached. The CCFL is, therefore, mitigated when the bubble release frequency is high. This might be the main reason why the CCFL with the rectangular tank is stronger than that with the cylindrical tank (a) at low Ku_G as shown in Figure 5.

3.2. Effects of Water Level in Tank. The CCFL characteristics measured using the cylindrical tank (b) shown in Figure 2(c) are discussed in this section. Various water levels in the upper and the lower tanks were tested. The water level in the lower tank was kept constant throughout each experiment by manually controlling the drain cock opening. In this case, Q_L was calculated from the amount of drain water. Figure 11 shows the CCFL characteristics for various water levels in the upper tank at constant water levels in the lower tank, where V_{Lower} is the air volume in the lower tank and h the elevation of the drain holes in the upper tank. The CCFL becomes stronger as h decreases at $V_{\text{Lower}} = 0.039$ m³. The difference in the CCFL characteristics is, however, not so significant. On the other hand, the CCFL characteristics strongly depend on h at $V_{\text{Lower}} = 0.092$ m³. Effects of V_{Lower} are shown in Figure 12. The CCFL characteristics do not depend on V_{Lower} at $h = 200$ mm, whereas the influence of V_{Lower} is significant at $h = 600$ mm, that is, the increase in V_{Lower} mitigates the CCFL.

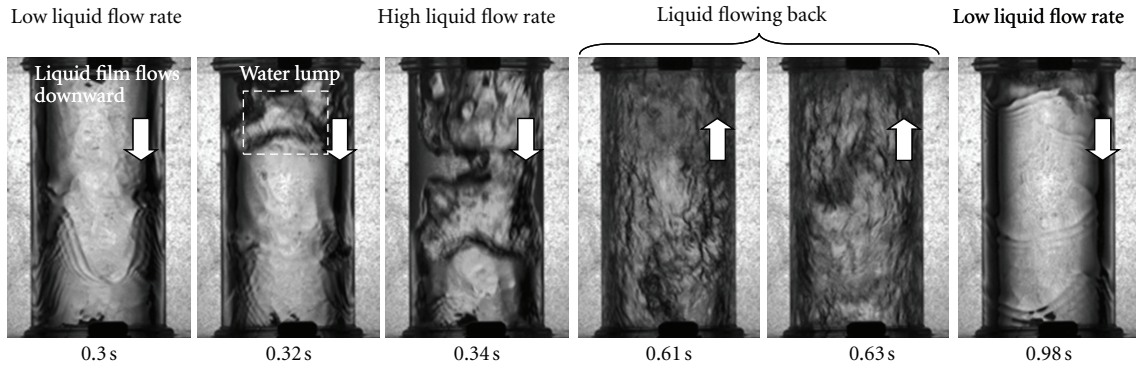


FIGURE 14: Flow patterns at the middle of the vertical pipe (Cylindrical tank (b), $D = 30$ mm, $h = 450$ mm, $V_{\text{Lower}} = 0.092$ m³, and $J_G = 9.1$ m/s).

Figure 13 shows the pressure differences for the cylindrical tank (b) and their power spectrums. The time-averaged ΔP increases with the water level in the upper tank, which corresponds to the water head in the upper tank. The amplitude of the pressure fluctuation at $h = 450$ mm is larger than that at $h = 200$ mm, and the fluctuation frequency at $h = 450$ mm is lower than that at $h = 200$ mm. Images of flow patterns in the middle part of the vertical pipe for $h = 450$ mm and $V_{\text{Lower}} = 0.039$ m³ are shown in Figure 14. The amount of falling liquid film is small at $t = 0.30$ s. The large water lump falls for $0.32 < t < 0.34$ s. The ΔP increases during the water lump falling. Then the liquid film flows back to the upper tank and the ΔP decreases. The liquid film restarts to fall at $t = 0.98$ s. The amount of the falling water lump is small at low h and low V_{Lower} , and it becomes larger as h and V_{Lower} increase. This is the main cause of the difference in the CCFL characteristics for different values of h and V_{Lower} .

4. Conclusions

Countercurrent flow limitation (CCFL) in vertical pipes are measured using an apparatus consisting of the vertical pipe, the upper tank, and the lower tank to understand effects of tank geometry and water level in the tanks. The tank shapes used were rectangular and cylindrical. The pipe diameters tested were 30, 45, and 60 mm. Air and water at room temperature and atmospheric pressure were supplied from the upper tank and from the lower tank, respectively. The flow rate of water entering into the lower tank was measured to obtain CCFL characteristics. Flow patterns in the upper tanks were observed by using a high-speed video camera and pressure differences between the upper and lower tanks were measured to understand relations between CCFL characteristics and the flow patterns in the tanks. The main conclusions obtained under the present experimental conditions are as follows.

- (1) The CCFL characteristics for different pipe diameters are well correlated using the Kutateladze number if the tank geometry and the water levels in the tanks are the same.

- (2) CCFL takes place at the junction between the pipe and the upper tank both for the rectangular and cylindrical tanks. In addition, CCFL with the cylindrical tank (a) takes place not only at the junction but also inside the pipe when the gas flow rate is high and the pipe diameter is small.
- (3) The flow rate of water entering into the vertical pipe at the junction for the rectangular upper tank is lower than that for the cylindrical tank (a) because of the presence of low frequency first-mode sloshing in the rectangular tank.
- (4) Water penetration into the pipe increases with the water level, h , in the cylindrical upper tank and the air volume, V_{Lower} , in the lower tank, and, therefore, the flow limitation is to be mitigated with increasing h and V_{Lower} .

These experimental results clearly show that not only the pipe geometry but also tank geometry and water levels in the tanks must be taken into account when modelling characteristics of CCFL in vertical pipes.

References

- [1] H. Nakamura, J. Katayama, and Y. Kukita, "Loss of Residual Heat Removal (RHR) event during PWR mid-loop operation: ROSA-IV/LSTF experiment without opening on primary loop pressure boundary," *ASME FED Power Plant Transients*, vol. 140, pp. 9–16, 1992.
- [2] C. Yanagi, T. Nariai, T. Futatsugi, A. Tomiyama, I. Kinoshita, and M. Murase, "Countercurrent air-water tests using a scale model of a pressurizer surge line," in *Proceedings of the 19th International Conference on Nuclear Engineering (ICONE19-43222)*, 2011.
- [3] G. B. Wallis, A. S. Karlin, C. R. Clark III, D. Bharathan, Y. Hagi, and H. J. Richter, "Countercurrent gas-liquid flow in parallel vertical tubes," *International Journal of Multiphase Flow*, vol. 7, no. 1, pp. 1–19, 1981.
- [4] D. Bharathan, G. B. Wallis, and H. J. Richter, *Air Water Countercurrent Annular Flow in Vertical Tubes*, EPRI NP-786, Electric Power Research Institute, 1978.

- [5] C. L. Tien and C. P. Liu, *Survey on Vertical Two-Phase Countercurrent Flooding*, EPRI NP-984, Electric Power Research Institute, 1979.
- [6] D. J. Nicklin and J. F. Davidson, "The onset of instability in two-phase slug flow," in *Proceedings of the Institute of Mechanical Engineers Symposium on Two-Phase Flow*, no. 4, 1962.
- [7] H. J. Richter, "Flooding in tubes and annuli," *International Journal of Multiphase Flow*, vol. 7, no. 6, pp. 647–658, 1981.
- [8] C. P. Liu, C. L. Tien, and G. E. McCarthy, *Flooding in Vertical Gas-Liquid Countercurrent Flow through Parallel Path*, EPRI-NP-2262, Electric Power Research Institute, 1982.
- [9] Y. Sudo, T. Usui, and M. Kaminaga, "Experimental study of falling water limitation under a counter-current flow in a vertical rectangular channel," *JSME International Journal, Series B*, vol. 34, no. 2, pp. 169–174, 1991.
- [10] J. H. Jeong and N. C. No, "Experimental study of the effect of pipe length and pipe-end geometry on flooding," *International Journal of Multiphase Flow*, vol. 22, no. 3, pp. 499–514, 1996.
- [11] F. Kaminaga, Y. Okamoto, and Y. Shibata, "Evaluation of Entrance Geometry Effect on Flooding," in *Proceedings of the 1st JMSE/ASME Joint International Conference on Nuclear Engineering*, vol. 95, 1991.
- [12] G. B. Wallis, D. C. deSiewes, R. J. Rosselli, and J. Lacombe, *Countercurrent Annular Flow Regimes for Steam and Subcooled Water in a Vertical Tube, NP-1336, Research Project 443-2*, EPRI, Palo Alto, Calif, USA, 1980.
- [13] D. Bharathan and G. B. Wallis, "Air-water countercurrent annular flow," *International Journal of Multiphase Flow*, vol. 9, no. 4, pp. 349–366, 1983.
- [14] G. B. Wallis, *One-Dimensional Two-Phase Flow*, McGraw Hill, 1969.
- [15] S. Jayanti, A. Tokarz, and G. F. Hewitt, "Theoretical investigation of the diameter effect on flooding in countercurrent flow," *International Journal of Multiphase Flow*, vol. 22, no. 2, pp. 307–324, 1996.
- [16] S. S. Kutateladze, "Elements of the Hydraulics of Gas-Liquid System," *Fluid Mechanics Soviet Research*, vol. 1, no. 4, pp. 29–50, 1972.
- [17] M. Vijayan, S. Jayanti, and A. R. Balakrishnan, "Effect of tube diameter on flooding," *International Journal of Multiphase Flow*, vol. 27, no. 5, pp. 797–816, 2001.
- [18] O. R. Jaiswal, S. Kulkarni, and P. Pathak, "A study on sloshing frequencies of fluid-tank system," in *Proceeding of the 14th World Conference on Earthquake Engineering*, 2008.

Research Article

Image-Processing-Based Study of the Interfacial Behavior of the Countercurrent Gas-Liquid Two-Phase Flow in a Hot Leg of a PWR

Gustavo A. Montoya,¹ Deendarlianto,² Dirk Lucas,³
Thomas Höhne,³ and Christophe Vallée³

¹ Chemical Engineering Department, Simon Bolivar University, Valle de Sartenejas, Baruta, 1080A Caracas, Venezuela

² Department of Mechanical and Industrial Engineering, Faculty of Engineering, Gadjah Mada University, Jalan Grafika No. 2, Yogyakarta 55281, Indonesia

³ Helmholtz-Zentrum Dresden-Rossendorf e.V., Institute of Safety Research, P.O. Box 510 119, 01314 Dresden, Germany

Correspondence should be addressed to Thomas Höhne, t.hoehne@hzdr.de

Received 20 September 2011; Revised 12 December 2011; Accepted 13 December 2011

Academic Editor: Michio Murase

Copyright © 2012 Gustavo A. Montoya et al. This is an open access article distributed under the Creative Commons Attribution License, which permits unrestricted use, distribution, and reproduction in any medium, provided the original work is properly cited.

The interfacial behavior during countercurrent two-phase flow of air-water and steam-water in a model of a PWR hot leg was studied quantitatively using digital image processing of a subsequent recorded video images of the experimental series obtained from the TOPFLOW facility, Helmholtz-Zentrum Dresden-Rossendorf e.V. (HZDR), Dresden, Germany. The developed image processing technique provides the transient data of water level inside the hot leg channel up to flooding condition. In this technique, the filters such as median and Gaussian were used to eliminate the drops and the bubbles from the interface and the wall of the test section. A Statistical treatment (average, standard deviation, and probability distribution function (PDF)) of the obtained water level data was carried out also to identify the flow behaviors. The obtained data are characterized by a high resolution in space and time, which makes them suitable for the development and validation of CFD-grade closure models, for example, for two-fluid model. This information is essential also for the development of mechanistic modeling on the relating phenomenon. It was clarified that the local water level at the crest of the hydraulic jump is strongly affected by the liquid properties.

1. Introduction

One hypothetical accident scenario in which two-phase countercurrent flow may occur in a PWR hot leg is a loss-of-coolant accident (LOCA), which is caused by the leakage at any location in the primary circuit. During this scenario it is considered that the reactor will be depressurized and vaporization will take place, thereby creating steam in the PWR primary side. Should this lead to “reflux condensation,” which may be a favorable event progression, the generated steam will flow to the steam generator through the hot leg. This steam will condense in the steam generator, and the condensate will flow back through the hot leg to the reactor, resulting in countercurrent steam/water flow. In some scenarios, the success of core cooling depends on the behavior of this countercurrent flow.

The stratified countercurrent flow of steam and condensate is only stable for a certain ranges of steam and water mass flow rates. For a given condensate flow rate, if the steam mass flow rate increases to a certain value, a portion of the condensate will exhibit a partial flow reversal and will be entrained by the steam in the opposite flow direction towards the steam generator. This phenomenon is known as countercurrent flow limitation (CCFL) or the onset of “flooding.” In case of an additional increase of the steam flow, the condensate is completely blocked and the reflux cooling mode ends. In this situation the cooling of the reactor core from the hot leg is impossible but may be continued by coolant drained through the cold leg to the downcomer. Figure 1 illustrates the countercurrent flow in the hot leg under reflux condensation conditions.

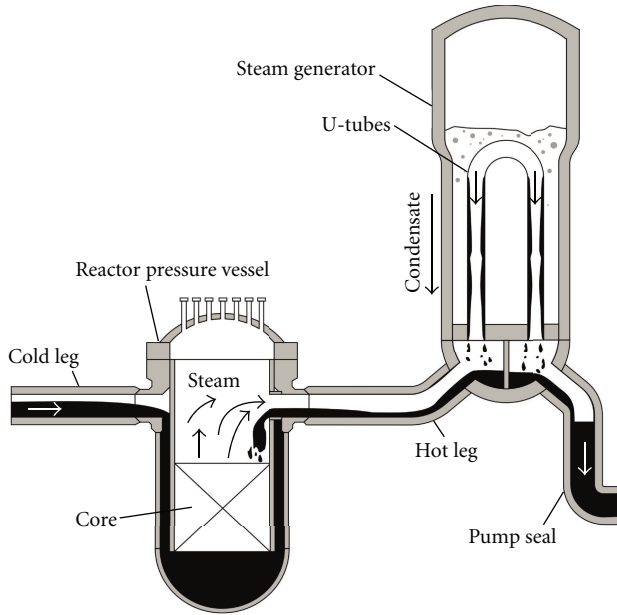


FIGURE 1: Konvoi German PWR piping configuration and reflux condensation flow paths [1].

In order to understand safety-related issues in nuclear power plants, analytical simulations using computational fluids dynamics (CFD) tools have been done, expecting to enhance the accuracy of the simulation predictions compared to the established one-dimensional thermal hydraulic analyses. Compare to the traditional thermal hydraulic codes, CFD would supply a more reliable scale up to the reactor scale, as well as a more flexible behavior in terms of transferability of models to changes in geometry and thermodynamic boundary conditions. This due to its ability to reveal the interactions between the phases, which are determined by interfacial transfers, and the ability to substitute geometry-dependent empirical closure relations with more physically justified closure laws formulated at the scale of the structures of the interface.

To support the theoretical model development and to validate the CFD codes, a horizontal rectangular channel connected to an inclined riser was constructed, as a model of a PWR hot leg, where air/water countercurrent two-phase flow experiments were performed. This equipment was installed in the pressure chamber of the TOPFLOW test facility (transient two-phase flow) of *Helmholtz-Zentrum Dresden-Rossendorf* (HZDR), Dresden, Germany. This model allows the investigation of co- and countercurrent flows under reactor typical boundary conditions (steam/water at pressures up to 5.0 MPa and saturation temperature). This has become the major experimental facility of the German CFD-network, initiated by the GRS (*Gesellschaft für Anlagen und Reaktorsicherheit mbH*).

For the CFD validation, it is of great importance to ensure a good access for measurements of distributed flow parameters, more than to create an exact geometrical similarity with the original equipment. Also, there is no need to quantify the critical mass flow rate since it was done

in the past (e.g., *UPTF, Germany, in UPTF-Fachtagung IV* [2]). In previous experiments, the recognition of bubbles and droplets as detailed structures was not possible mainly because the optical access was limited, and so the observation of the flow was mainly used to support the interpretation of results.

Since investigations in the past, performed in pipes [3–5], were limited by the three-dimensional shape of the interfacial structure, the new test section has been optimized for the application of optical observation using a flat channel model of a PWR hot leg. In order to accelerate the CFD code validation program, the high-resolution pictures were analyzed by own developed image-processing algorithms. In the present paper, experimental procedure and developed image-processing technique will be presented firstly. Next, the time variation of water level inside the hot leg channel around the CCFL will be given. By using this data, the development of the waves around the CCFL can be clarified. Next, the statistical treatment of the data will be presented on the basis of the average parameters. Finally, the effect of fundamental parameters such as liquid mass flow rate, system pressure, and liquid properties will be discussed.

2. Experimental System and Image Processing Technique

2.1. Experimental Setup. A schematic view of the hot leg model test section is shown in Figure 2. It consists of the test section, the reactor pressure vessel (RPV) simulator located at the lower end of the horizontal channel, and the steam generator (SG) separator connected to the inlet chamber. This test section is a reproduction of the diameter of PWR hot leg of a German *Konvoi* type at a 1:3 scale. In order to provide better viewing conditions, the test section is not composed of pipes as in the original plant, but rather is a channel of about 50 mm (wide) which represents a vertical cut through the midplane of the hot leg and the inlet chamber of the steam generator. By using a flat section the error produced by the three-dimensional interface in high-speed videos is eliminated, allowing a closer look of the interface, including dispersed structures (drops and bubbles) that cannot be observed in a common pipe. Consequently, the test section is composed of a horizontal rectangular channel, a bend that connects it to an upward inclined and expanded channel, and a quarter of a circle representing the steam generator inlet chamber. The horizontal part of test section is 2.12 m long and has a rectangular cross-section of 0.05 m × 0.25 m. The SG and RPV simulators are identical vessels with 0.8 m × 0.5 m × 1.55 m (D × W × H) cubic shape.

Unfortunately, due to the overall dimensions of the hot leg model (3 m long), it was not possible to visualize the complete test section. Therefore, a region of observation had to be chosen. Previous investigations (e.g., [3]) indicate that the most agitated flow region is located near the bend and that a recirculation zone is formed there. Consequently, it was chosen to observe the bended region of the hot leg and the steam generator inlet chamber as shown in Figure 2. The

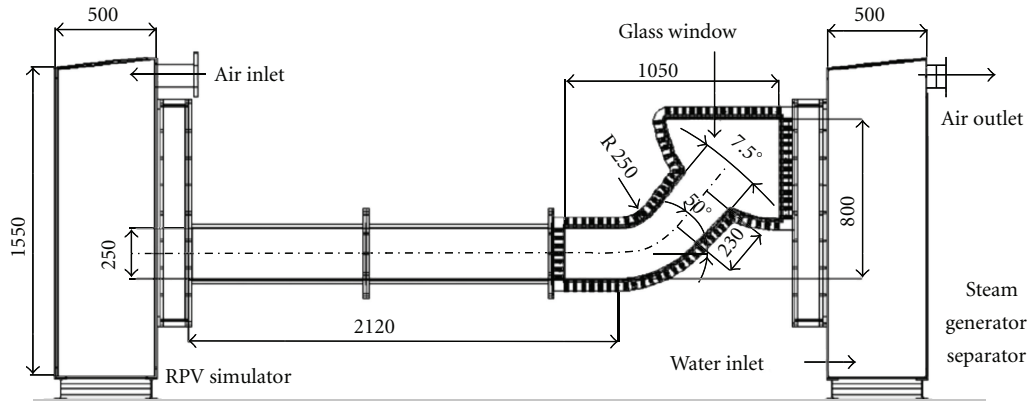


FIGURE 2: Schematic view of the hot leg model test section (dimension in mm).

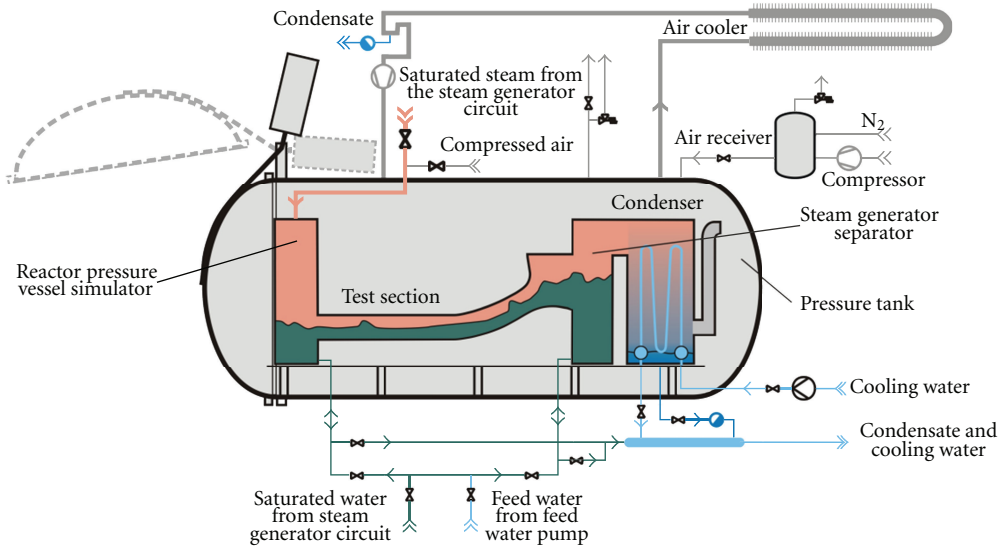


FIGURE 3: Schematic diagram of the experimental apparatus.

flow behavior was recorded by a high-speed video camera at frequencies of 60 to 100 Hz and a shutter speed of 1/1000 s.

The test section was placed in a pressure chamber, in which it was operated in pressure equilibrium with the inner atmosphere of the tank in TOPFLOW (transient two-phase flow) facility as shown in Figure 3. A special heat exchanger condenses the exhaust vapor from the test section directly in the pressure vessel, when steam/water experiments are made. As shown in Figure 3, the cold end of this condenser and the inside atmosphere of the vessel are permanently connected, in order to guarantee full pressure equilibrium at all times [6]. The vessel can be pressurized up to 5 MPa either with air for cold experiments or with nitrogen for steam experiments. Using this method allowed to design the equipment with thin materials.

The injected water mass flow rate was measured by a vortex meter. The injected air mass flow rate was measured and controlled using thermal mass flow meters. The steam flow rate over the pressure drop was measured through a venturi's tube. The temperatures of the fluids were measured

by thermocouples at various positions in the facility. The water levels in both tanks were determined by the measurement of the differential pressure between the top and the bottom of the vessels with differential pressure transducers. The pressure drop over the test section was measured by a differential pressure transducer placed between the SG simulator and the RPV separator. These global parameters were measured via a data acquisition system running at 1 Hz, which was synchronized with the high-speed video camera.

In this experiment, the air was injected in the RPV simulator and flowed through the test section to the SG separator, from which it was released to the inner atmosphere of the pressure tank. The water from the feed water pump was injected in the SG separator, from where it can flow in countercurrent to the air flow through the test section to the RPV simulator. The onset of flooding was obtained by a stepwise increase of the gas mass flow rate with a small increment (9–35 g/s), under a constant water mass flow rate. Due to the internal buffer of the high-speed camera that was limited to 8 GB, a compromise had to be found in each run

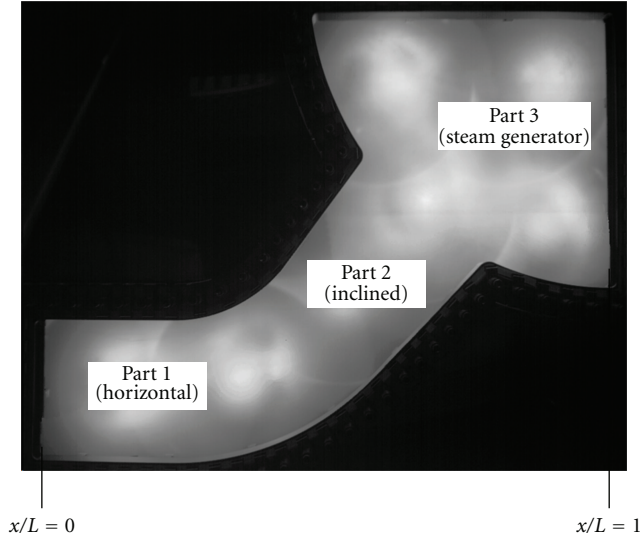


FIGURE 4: Submatrix segmentations in the image processing.

between the number and duration of the plateau of air flow rate. The number of plateau realized during one run was varied between 4 and 8, with a duration of each between 15 and 35 s [7].

The onset of flooding was defined as the limiting point of stability of the countercurrent flow, indicated by the maximum air mass flow rate at which the down-flowing water mass flow rate is equal to the inlet water mass flow rate. This is a method used previously by Zabaras and Dukler [8] and Deendarlianto et al. [9]. The experiments were carried out until the point of zero liquid penetration occurs, when the down-flowing water mass flow rate was equal to zero [7].

During the onset of flooding, the water level reached in the horizontal segment of the hot leg, obstructs the passage of steam enough to generate waves at the interface, which are eventually transform into slugs. Consequently, the pressure difference between the separators increase and become unstable. Then, the gas that impedes the water to flow into the RPV accumulates in the SG separator. The average pressure drop through the test section increases with the level of water in the steam generator, and the slug increases until the zero liquid penetration point occurs.

2.2. Image Process Techniques. For the analysis of the high-speed video data obtained from the TOPFLOW experiments, two programs based on image processing techniques were used. These programs were written in MATLAB code along with simulink files. First the program will cut a submatrix from the original data, which becomes separate in a horizontal, inclined, and steam generator segments of the image as shown in Figure 4. An example of one image before processing can be seen in Figure 5(a).

A pre-processing stage is begun in the horizontal segment of the image in order to improve the interface in this part. Next step is to eliminate the drops and bubbles in the interface and the water that is stick in the walls of the test

TABLE 1: Analyzed experimental data.

Gas	Pressure (MPa)	Experimental running			
Steam	5.00	06-15			
Steam	3.00	15-07	15-10		
Steam	2.36				11-07
Steam	1.50	11-01		11-04	
Air	0.30	18-09	30-05		
Air	0.15	19-02	30-09		
		0.15	0.3	0.6	Water (kg/s)

section. Here the bubbles and drops were considered as noise and possible reason of error. In order to correct this, the smooth filters were used to eliminate any salt and pepper noise.

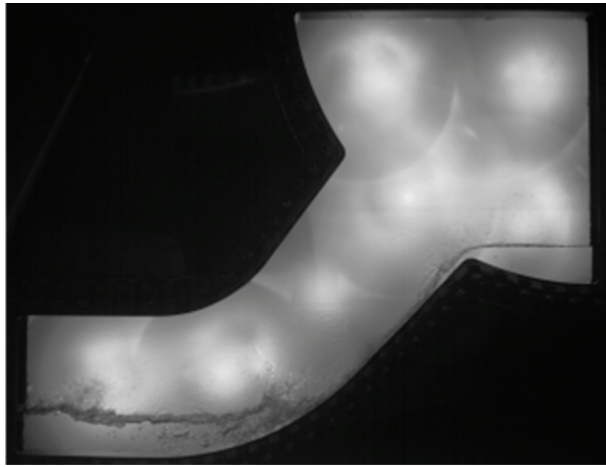
In order to improve the uneven light conditions found in the data before processing, a background was created using the first image obtained from the Gaussian filter. After this, the background image is subtracted from the one before the background development. Next, an image enhancement function was implemented to improve the contrast. Finally, the image quality can be improved. An example of the processing steps of the horizontal segment can be found in Figure 5(b).

When analyzing the inclined segment, the original image is rotated about -50 degrees in order to make it become a horizontal approximation as in Figure 5(c). For the steam generator, the raw image is cut into a submatrix leaving only the part of interest. When the preprocessed of the steam generator segment ends, then all the obtained data is send from the workspace to a simulink file. In this file, the raw image is binarized in order to detect the borders of the hot leg channel. Finally, the water level can be calculated. An example of the processing steps for the steam generator segment can be found in the Figure 5(d).

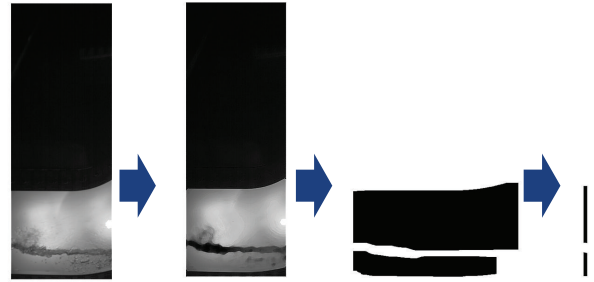
To obtain the local information, the picture was divided into twelve points for the horizontal segment, nine points for inclined segment, and ten points for the steam generator segment. The program for analyzing the steam-water data works on the same philosophy as the air-water data. Finally, an example of the detected water level for the steam-water case is shown in Figures 6(a) and 6(b).

Ten experimental data series of HZDR in total were studied. Six of them were steam-water, and four of them were air-water. These sets of data were chosen in order to obtain a wide variety of parameters' combinations for pressure and mass flow rate, where XY-WZ represents the name of the specific experiment based on the date in which the experiment was made. The selected series are shown in Table 1.

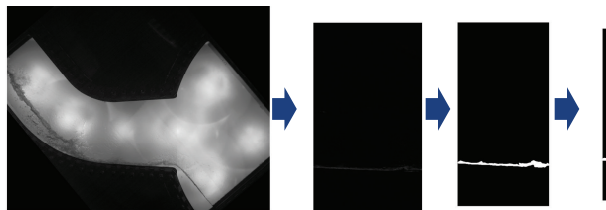
Extensive checks were made in order to analyze the quality of the algorithm, but the most useful method in order to verify the reliance of the code is an automated one inside the same algorithm. When the water level's values are found in pixels, the algorithm creates markers that are drawn in the exact place in the original gray-level images where the water level point was calculated. This allows verifying each



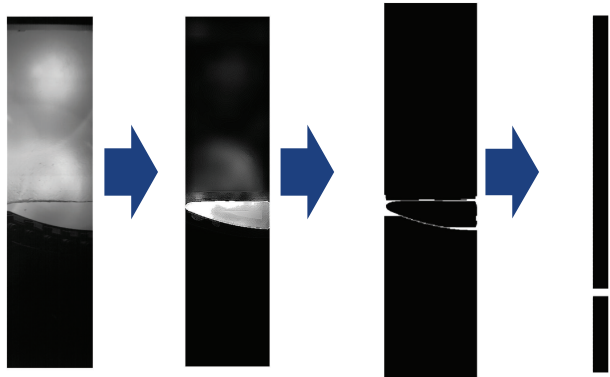
(a) Example of an original image of steam-water



(b) Image processing, contrast enhancement, and binarization of the horizontal section for the steam-water data

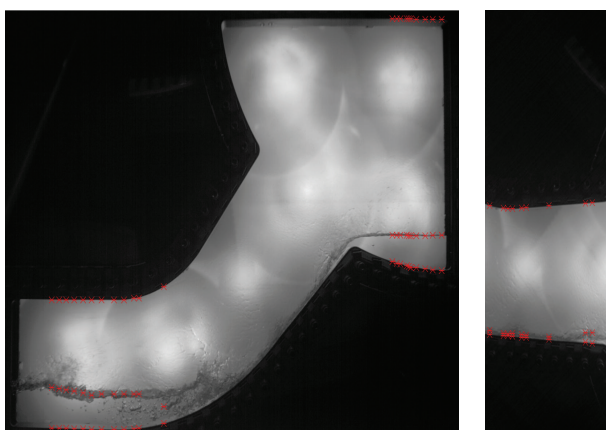


(c) Image processing, contrast enhancement, and binarization of the inclined section for the steam-water data



(d) Image processing, contrast enhancement, and binarization of the steam generator section for the steam-water data

FIGURE 5: Detected water level and boundaries of the hot leg channel (steam-water).



(a) Horizontal and steam generator (b) Inclined

FIGURE 6: Detected water level and boundaries of the hot leg channel (steam-water).

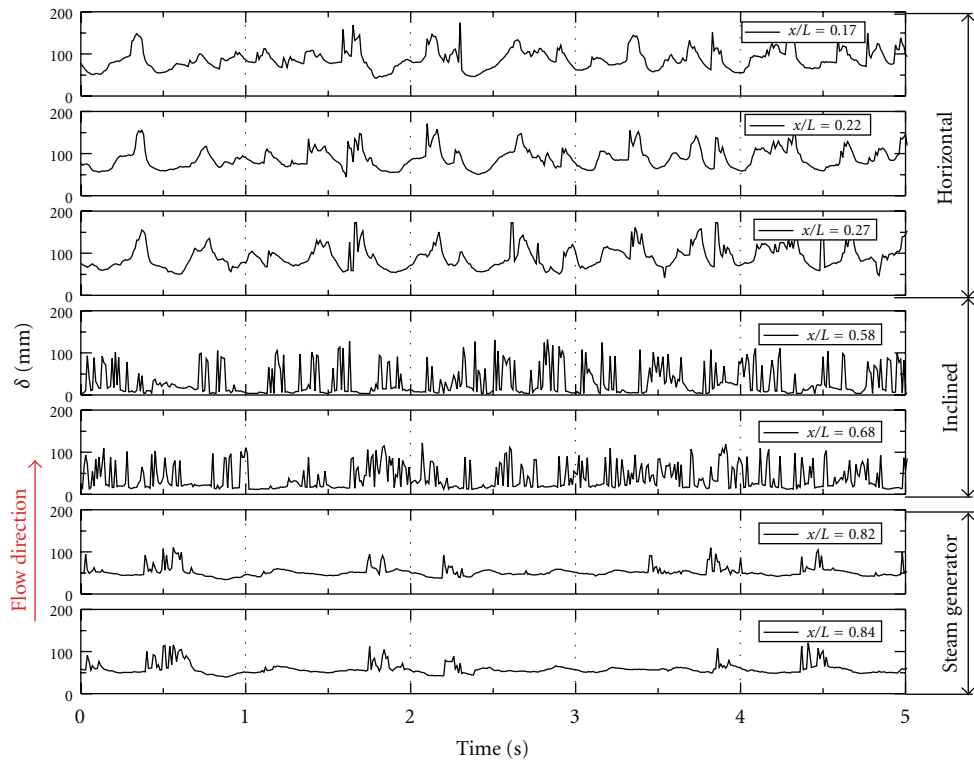
exact value that is calculated for each water level in every image. This is made automated, and the result images with

the markers are saved in a separate folder, which allow the possibility of verifying the results during any point after the processing of a set of images.

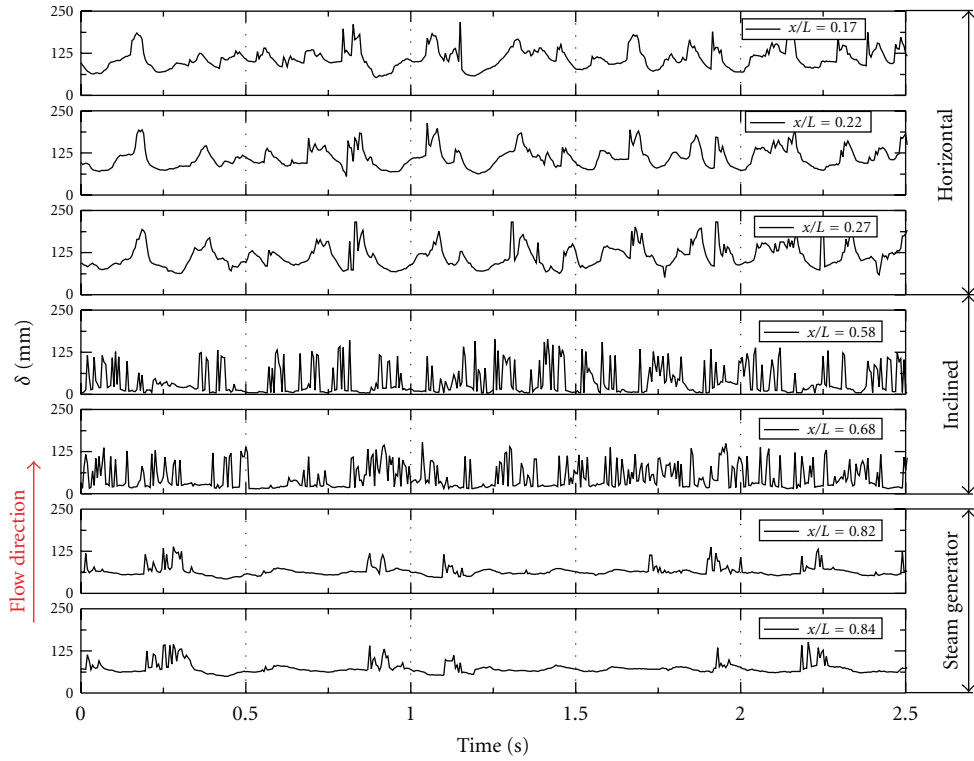
Analyzing a representative set of data of 5000 pictures after using the image processing algorithm on them, allowed to find that 233 points out of 155000 were deviated from the actual interphase, which represents a discrepancy of 0.15%.

3. Results and Discussions

Figures 7(a) and 7(b) show the time variation of the water level during the CCFL of air-water and steam-water, respectively. The injected liquid mass flow rate was 0.3 kg/s. The temperature of the fluids for the experiments with air/water was 18–24°C (room temperature) and for steam/water was saturation temperature. As shown in the figure, the water level in the horizontal and inclined parts exhibits notable oscillations, and the shape of the wave varies along the channel. This indicates that the wave patterns during the CCFL are space and time dependent. Next, it can be seen that the successive waves do not follow the direction of liquid injection, and for that matter the CCFL can be identified.



(a) Air-water ($P = 0.15$ MPa, $m_L = 0.30$ kg/s, $m_G = 0.28$ kg/s)



(b) Steam-water ($P = 1.5$ MPa, $m_L = 0.30$ kg/s, $m_G = 0.53$ kg/s)

FIGURE 7: Time variation of water level inside the hot leg channel during CCFL.

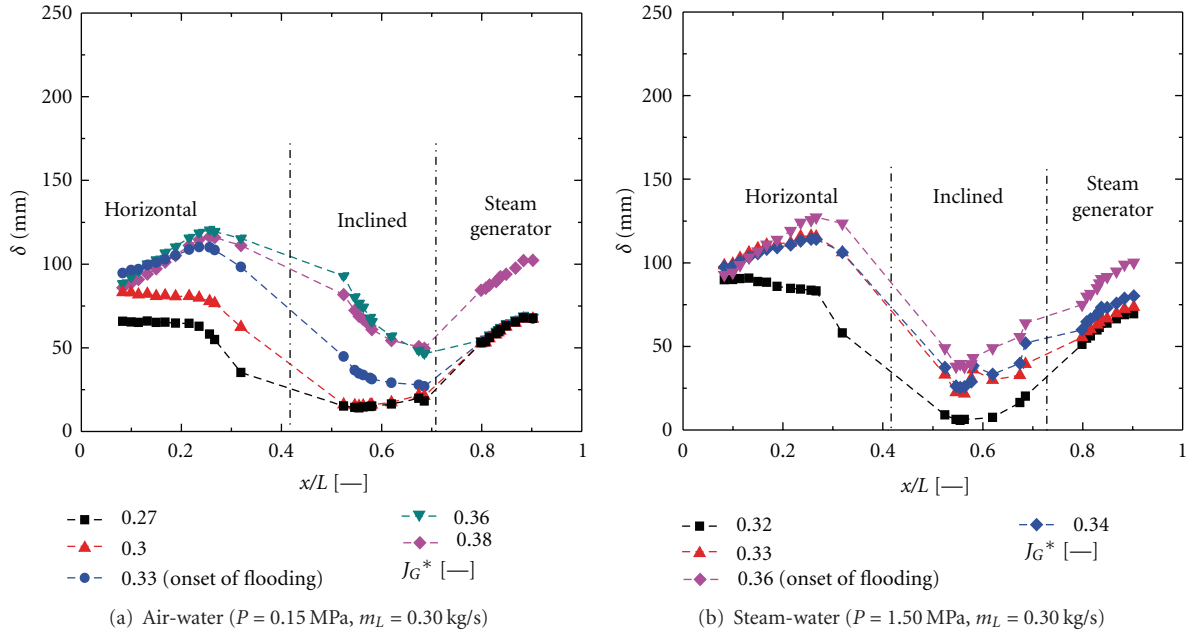


FIGURE 8: Time average of the water level distribution inside the hot leg channel.

In addition, the maximum of the water level was lower than 250 mm. This indicates that there is no total blockage of the water inside the channel during the CCFL.

3.1. Average Parameters. Figure 8 illustrates the distribution of the water level inside the hot leg channel. Figures 8(a) and 8(b) correspond to the cases of air-water and steam-water, respectively. The injected liquid mass flow rate was 0.3 kg/s of each case. For a meaningful comparison, a nondimensional gas superficial velocity J_G^* , namely, as gas Wallis parameter, is used. Here the gas Wallis parameter in Figure 8 is defined as follows:

$$J_k^* = J_G \sqrt{\frac{1}{gH} \cdot \frac{\rho_G}{(\rho_L - \rho_G)}}, \quad (1)$$

where J_G indicates the superficial gas velocity, ρ the density, g the acceleration of gravity, and H the height of the channel. Close inspection of Figure 8 reveals that before the onset of flooding the water levels in horizontal and inclined parts increase with the increase of the gas Wallis parameter. Meanwhile it is almost constant in the steam generator until the onset of flooding. Next, it shows also that the water level in the horizontal part decreases when x/L closes to the inclined part. The decrease of water level at the beginning of the inclined part indicates the change of the liquid film profile from the subcritical to supercritical condition as described by Deendarlianto et al. [7]. Meanwhile this profile changes dramatically when the gas mass flow rate approaches the onset flooding. This means that the change of wave direction is begun here. Next, it is noticed the observed phenomenon of air-water is the same as of the steam-water.

Figure 9 illustrates the standard deviation of water level inside the hot leg channel. The flow condition was similar to

that of Figure 8. The figure shows that the standard deviation in horizontal and inclined parts increases with the increase of gas Wallis parameter. This means that wave fluctuations increase also with the increase of the gas superficial velocity. On the other hand, the wave in the steam generator begins fluctuating near the onset of flooding.

A small algorithm to calculate the probability distribution function was created. The probability distribution of a random variable can be defined as a function that assigns the probability that an event occurs to each defined variable. The program computed the *normpdf* (X, μ, σ). This function determines the PDF for each value of X , using the data, the average, and standard deviation. The mathematical function that defined this is

$$y = f(x | \mu, \sigma) = \frac{1}{\sigma\sqrt{2\pi}} e^{-(x-\mu)^2/2\sigma^2}. \quad (2)$$

After the calculation of the PDF, the obtained values are ordered from highest to lowest to get the PDF chart with the values placed in a corresponding manner, without requiring any subsequent operation. This operation is performed for the 31 data points (x/L).

At the end of the program, the results for the 31 points of the PDF are stored in two vectors to be used or transferred to another cell's working program in the future (e.g., Excel).

Figure 10 shows the example of the probability distribution function (PDF) of the water level at the horizontal segment. This figure reveals that the PDF begins to spread when the gas velocity approaches the onset of flooding. From this result, it is possible to notice that the spread of PDF in the horizontal position under this flow condition can be used as a good indicator to detect the occurrence of flooding.

When J_G^* is small compared with the other values studied in this case, the probability function is represented

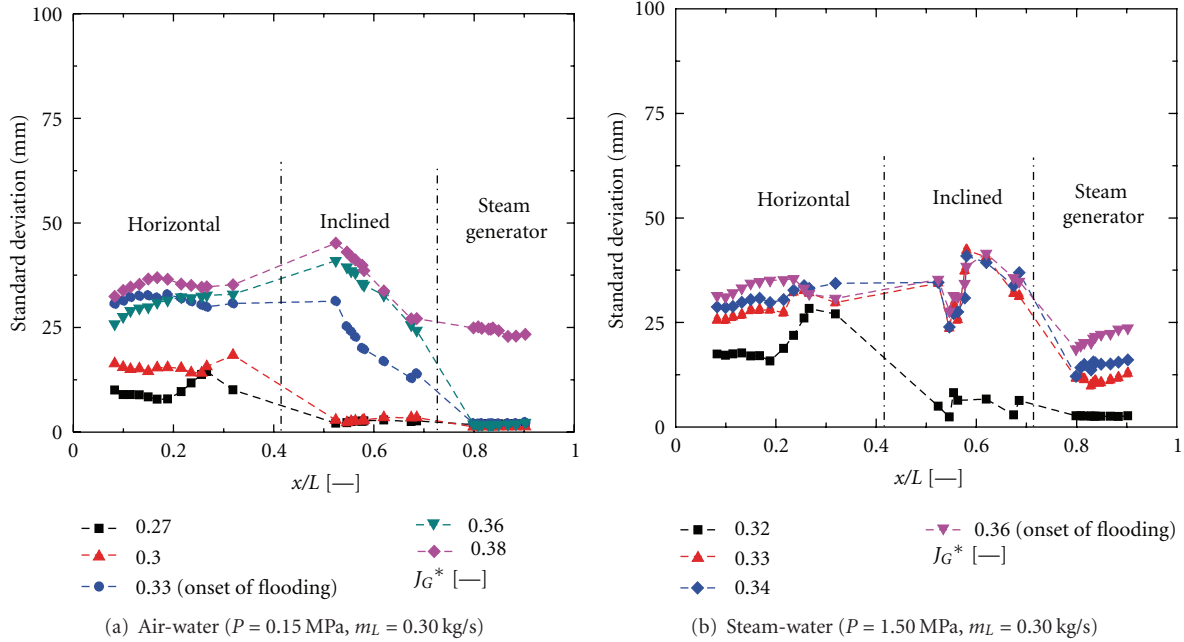


FIGURE 9: Distribution of the standard deviation of the water level inside the hot leg channel.

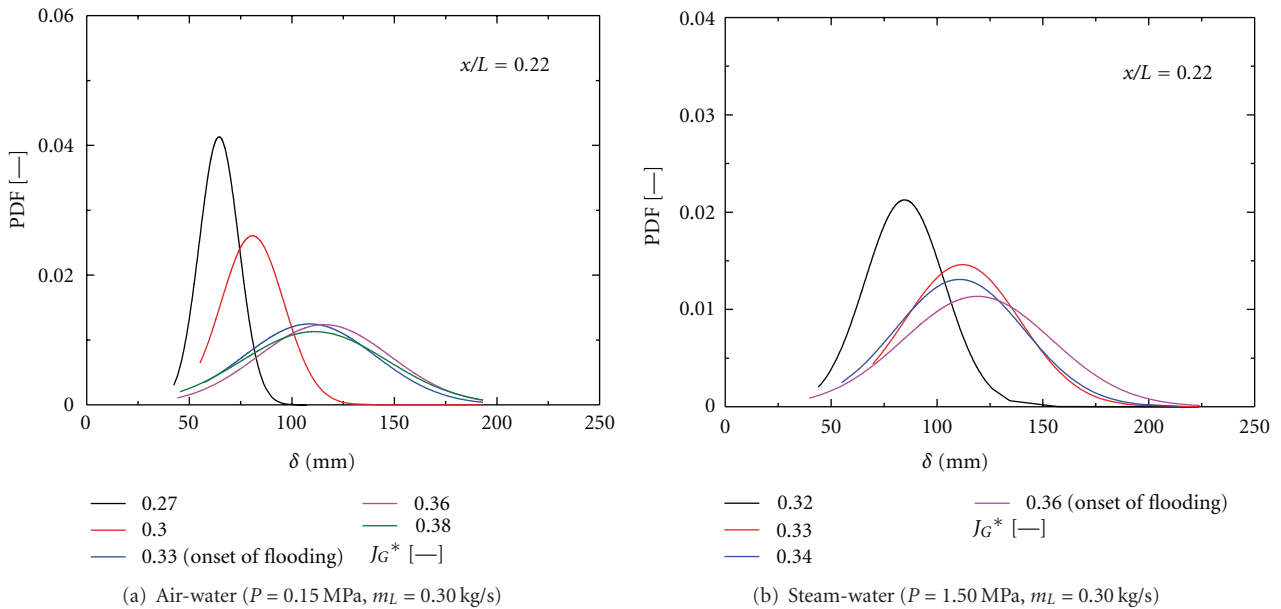


FIGURE 10: Probability distribution function ($x/L = 0.22$, $m_L = 0.3$ kg/s).

by a curve with the smallest dispersion of water levels in comparison with the rest. This curve is equivalent to a stratified and almost laminar flow. As J_G^* increases, the curve opens and the dispersion of probabilities on the water level rises. This means that as J_G^* increases, the flow becomes more turbulent and less stratified, which is why it can be seen an opening of the probability to multiple values of water level instead of tending to one.

In the case of Figure 10(a), before reaching the CCFL ($J_G^* < 0.33$), the values of the liquid phase level in which the

probabilities are greater are displaced to the left, indicating a lower water level at this point. Then, when the CCFL occurs ($J_G^* = 0.33$), the values became more scattered (less stratified flow), and the level of the phase is most likely to become greater in the region near the elbow. It can be seen that, once the onset of flooding is reached, the curves for higher J_G^* are maintained around the same values.

While in Figure 10(b) could be difficult to find the point for the onset of flooding, it can be noticed that, based on the same principle, the values keep changing, becoming

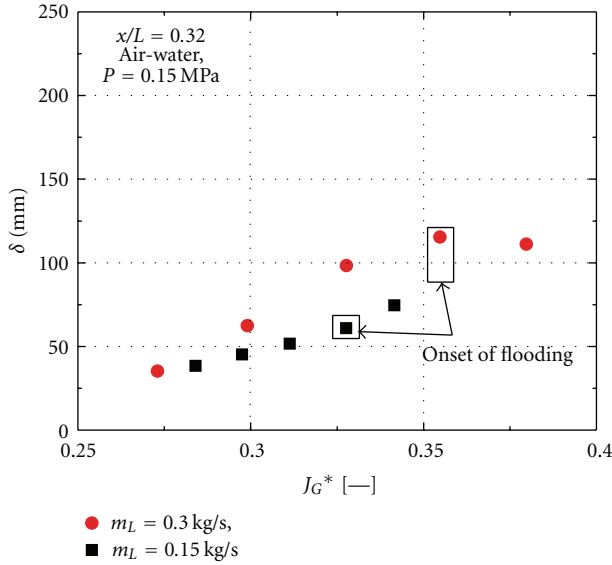


FIGURE 11: Effect of injected liquid mass flow rate on the water level.

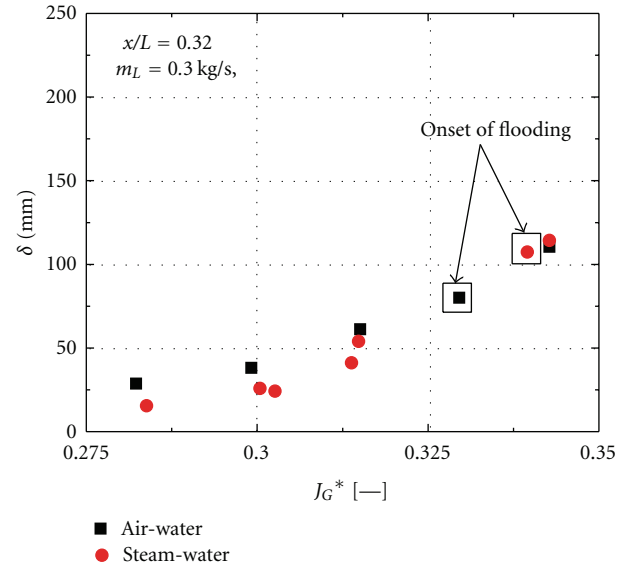


FIGURE 13: Effect of physical properties on the water level.

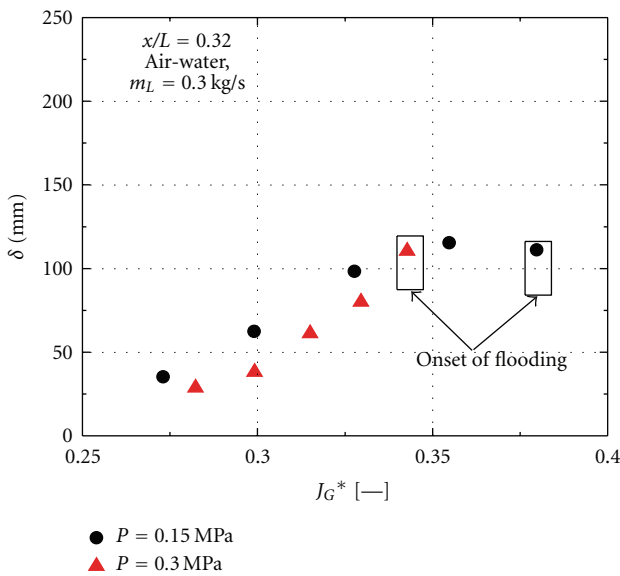


FIGURE 12: Effect of system pressure on the water level.

increasingly dispersed until $J_G^* = 0.36$. This same pattern repeats for all the other experimental conditions. One of the main differences between air/water and steam/water experiments when analyzing the PDF is that because the steam/water interphase is not completely laminar since low values J_G^* , then the change to the onset of flooding seems more drastic in the air/water experiments.

Figures 11 to 13 show the effects of the fundamental parameters such as the injected liquid mass flow rate, system pressure, and liquid properties on the water level inside the hot leg channel, respectively. The shown data is the water level at the horizontal part of $x/L = 0.32$, which is the closest location to the elbow. It was taken due to the consideration

that the flooding coincides to the slugging inception in the lower leg of the elbow close to the bend [10, 11].

Figure 11 shows that for the conditions presented, when every parameter but the liquid mass flow rate is fixed, the water level will depend of this last value. When $m_L = 0.30$ kg/s, the water level will be approximately 100 mm greater than that when a liquid mass flow rate of 0.15 kg/s is used.

In Figure 12, the effect of system pressure of water level is shown. It can be seen that, when every parameter is fixed but the system pressure, the water phase is maintained almost at the same level. Finally, Figure 13 shows the effect of physical properties over the water level, where it can be seen that when air-water are used as the fluids for the experiments, the water level in the onset of flooding increases in around 80 mm when compared to the experiment in which the steam-water are the working fluids. The same pattern repeats when other experiments are analyzed. This clearly indicates that the liquid mass flow rate and the physical properties greatly affect the onset of flooding in the experiments, while the pressure is a parameter that would not affect the water level in a drastic way when changed.

Then, it is shown that before the onset of flooding the water level increases with the increase of gas superficial velocity. Meanwhile, at the onset of flooding, it is dependent on the injected liquid mass flow rate and the physical properties. Those effects were not considered by previous researches; therefore, the proposed flooding correlations in their literature were not successful.

4. Conclusions

An image-processing technique was developed to analyse the sequence video images of the countercurrent gas-liquid two-phase flow of air-water and steam-water in a model of PWR hot leg. The data images were taken from the experimental

series of TOPFLOW facility, HZDR, Dresden, Germany. This technique allows us to access the quantitative local flow information; therefore, a detailed CFD-grade data for the water level evolution inside the hot leg channel including its statistic characteristics were set up. Extensive checks were also made with regard to the quality of the method. The data can be used to validate the CFD code, and physics behind the observed phenomenon were clarified by being able to understand more in deep the behavior of the system and the particular properties that affected the water level during the onset of flooding, as well as the effect of the J_G^* in the water level and the time-dependent interfacial behavior of the flow.

Acknowledgments

This work is carried out within the frame work of a current research project funded by the German Federal Ministry of Economics and Technology, Project number 1501329. The authors would like to thank also the TOPFLOW team for their work on the test facility and the preparation of the experiments. Dr. Deendarlianto is an Alexander von Humboldt Fellow in the Institute of Safety Research, Helmholtz-Zentrum Dresden-Rossendorf e.V., Germany. The present research is also supported by the Alexander von Humboldt Foundation in Germany.

References

- [1] T. Seidel, C. Vallée, D. Lucas, M. Beyer, and Deendarlianto, "Two-Phase Flow Experiments in a Model of the Hot Leg of a Pressurised Water Reactor," Wissenschaftlich-Technische Berichte/Forschungszentrum Dresden-Rossendorf; FZD-531, 2010.
- [2] UPTF-Fachtagung IV, Versuchsergebnisse, Analysen, Mannheim 25. Marz , Siemens AG, KWU, KWU R 11/93/005, 1993.
- [3] A. Ohnuki, H. Adachi, and Y. Murao, "Scale effects on countercurrent gas-liquid flow in a horizontal tube connected to an inclined riser," *Nuclear Engineering and Design*, vol. 107, no. 3, pp. 283–294, 1988.
- [4] S. Wongwises, "Experimental investigation of two-phase countercurrent flow limitation in a bend between horizontal and inclined pipes," *Experimental Thermal and Fluid Science*, vol. 8, no. 3, pp. 245–259, 1994.
- [5] M. A. Navarro, "Study of countercurrent flow limitation in a horizontal pipe connected to an inclined one," *Nuclear Engineering and Design*, vol. 235, no. 10–12, pp. 1139–1148, 2005.
- [6] H. M. Prasser, M. Beyer, H. Carl et al., "The multipurpose thermalhydraulic test facility TOPFLOW: an overview on experimental capabilities, instrumentation and results," *Kern-technik*, vol. 71, no. 4, pp. 163–173, 2006.
- [7] Deendarlianto, C. Vallée, D. Lucas, M. Beyer, H. Pietruske, and H. Carl, "Experimental study on the air/water counter-current flow limitation in a model of the hot leg of a pressurized water reactor," *Nuclear Engineering and Design*, vol. 238, no. 12, pp. 3389–3402, 2008.
- [8] G. J. Zabaras and A. E. Dukler, "Counter-current gas-liquid annular flow, including the flooding state," *AIChE Journal*, vol. 34, no. 3, pp. 389–396, 1988.
- [9] Deendarlianto, A. Ousaka, A. Kariyasaki, and T. Fukano, "Investigation of liquid film behavior at the onset of flooding during adiabatic counter-current air-water two-phase flow in an inclined pipe," *Nuclear Engineering and Design*, vol. 235, no. 21, pp. 2281–2294, 2005.
- [10] K. H. Ardron and S. Banerjee, "Flooding in an elbow between a vertical and a horizontal or near-horizontal pipe. Part II: theory," *International Journal of Multiphase Flow*, vol. 12, no. 4, pp. 543–558, 1986.
- [11] S. Wongwises, "Two-phase countercurrent flow in a model of a pressurized water reactor hot leg," *Nuclear Engineering and Design*, vol. 166, no. 2, pp. 121–133, 1996.

Research Article

Experimental Investigation of Rising Gas Bubble Characteristics from a Vertical Tube under CCFL Condition

Kunihito Matsumura and Fumito Kaminaga

Faculty of Engineering, Ibaraki University, 4-12-1 Nakanarusawa, Hitachi Ibaraki 316-8511, Japan

Correspondence should be addressed to Kunihito Matsumura, kunimatsu@mx.ibaraki.ac.jp

Received 11 November 2011; Accepted 10 January 2012

Academic Editor: Michio Murase

Copyright © 2012 K. Matsumura and F. Kaminaga. This is an open access article distributed under the Creative Commons Attribution License, which permits unrestricted use, distribution, and reproduction in any medium, provided the original work is properly cited.

This paper describes an experimental study of gas/liquid countercurrent flow in a vertical circular tube. CCFL experiments were carried out with three different water levels in the upper plenum, two different tube diameters. Measurements were made for liquid and gas flow rates, time variations of pressure at locations of the upper entry of the tube and lower plenum. Visual observations were also conducted to investigate the relationship between rising gas bubble characteristics and time variation of gas pressure at the upper entry of the tube. The results indicate that one bubble formation cycle (e.g., bubble growth, expansion, and detachment into the water pool) corresponds to one pressure fluctuation cycle. For the 20 mm diameter tube, it was confirmed that there was a characteristic waiting time between bubble cycles in which no bubble was formed at the upper entry of the tube. The waiting time is a favorable time for a liquid introduction into the tube from the upper plenum. The bubble volumes are compared with existing bubble formation correlations.

1. Introduction

Countercurrent gas/liquid flow is generally characterized by an interaction between a gas flowing upwards inside a conduit and a liquid falling counter-currently along its wall. It has been an important design criterion in a variety of industrial equipments, such as chemical reaction in a chemical reactor, evaporators, reflux condensers, and two phase heat exchangers. The departure from stable countercurrent gas/liquid flow is of major importance in the operation of Emergency Core Cooling System (ECCS) during a postulated loss of coolant accident in light water nuclear reactor. There is a possibility that the downward flow of emergency coolant may be limited by uprising steam generated from coolant evaporation, therefore, accurate prediction of CCFL is a significant aspect for evaluating the performance of core cooling devices. Countercurrent flow has been studied both experimentally and theoretically for a long time by many researchers. Although many studies have been made on the

fundamental processes of the countercurrent flow, there is still some uncertainty about the precise mechanism in countercurrent flow transition.

The countercurrent flow transition can be classified into two regimes. One is generally called flooding which means the flow transition from the annular flow to the mixing flow occurred through an entire length of a flow channel and initiated by a large liquid entrainment due to choking of the gas flow path in the channel on increasing gas flow rate and/or liquid flow rate. The other is called the countercurrent flow limiting, CCFL, which occurs locally at an upper end of a channel connecting to a liquid pool besides a steady annular flow indicated on the other locations inside the channel. The most widely used empirical correlation for air/water countercurrent flow was proposed by Wallis [1]. This correlation derived from experiments in vertical small diameter tubes and it can be expressed as follows:

$$j_g^{*0.5} + m j_l^{*0.5} = C, \quad (1)$$

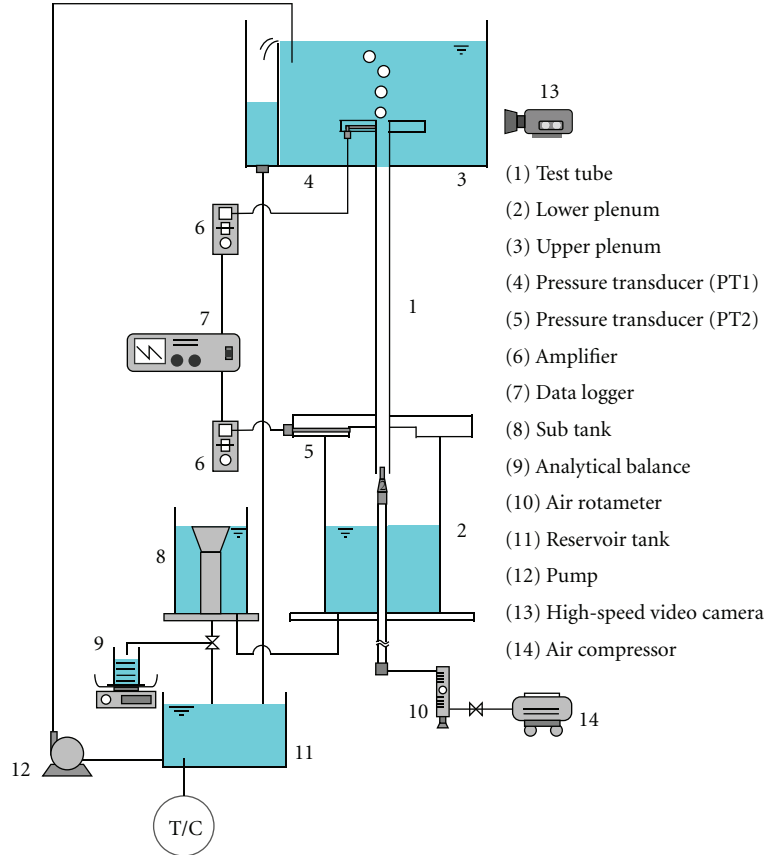


FIGURE 1: Schematic diagram of experimental apparatus.

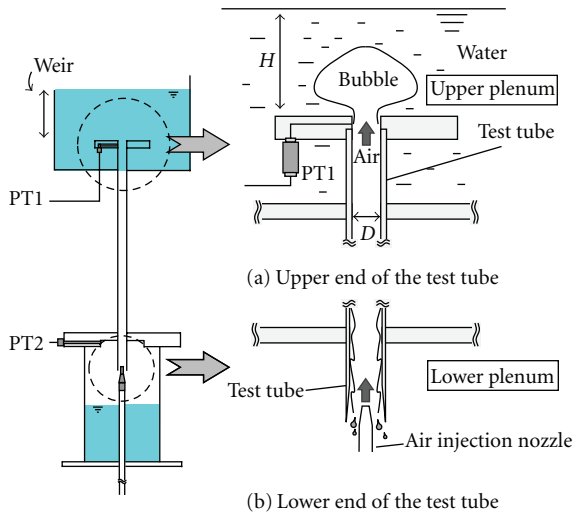
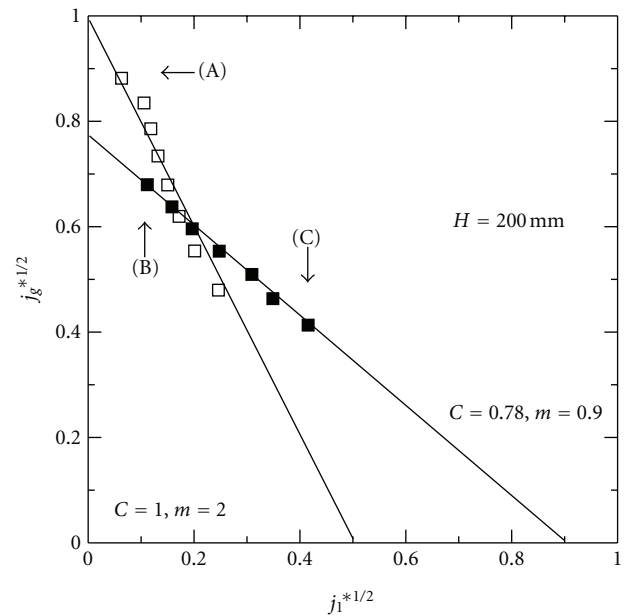


FIGURE 2: Details of the upper and lower end geometries.

where j_g^* and j_l^* are the dimensionless gas and liquid superficial velocities given by

$$j_g^* = j_g \sqrt{\frac{\rho_g}{gD(\rho_l - \rho_g)}}, \quad (2)$$



□ $D = 12 \text{ mm}$
 ■ $D = 20 \text{ mm}$

FIGURE 3: Dimensionless downward liquid flow rate against gas flow rate in CCFL condition for different tube diameter.

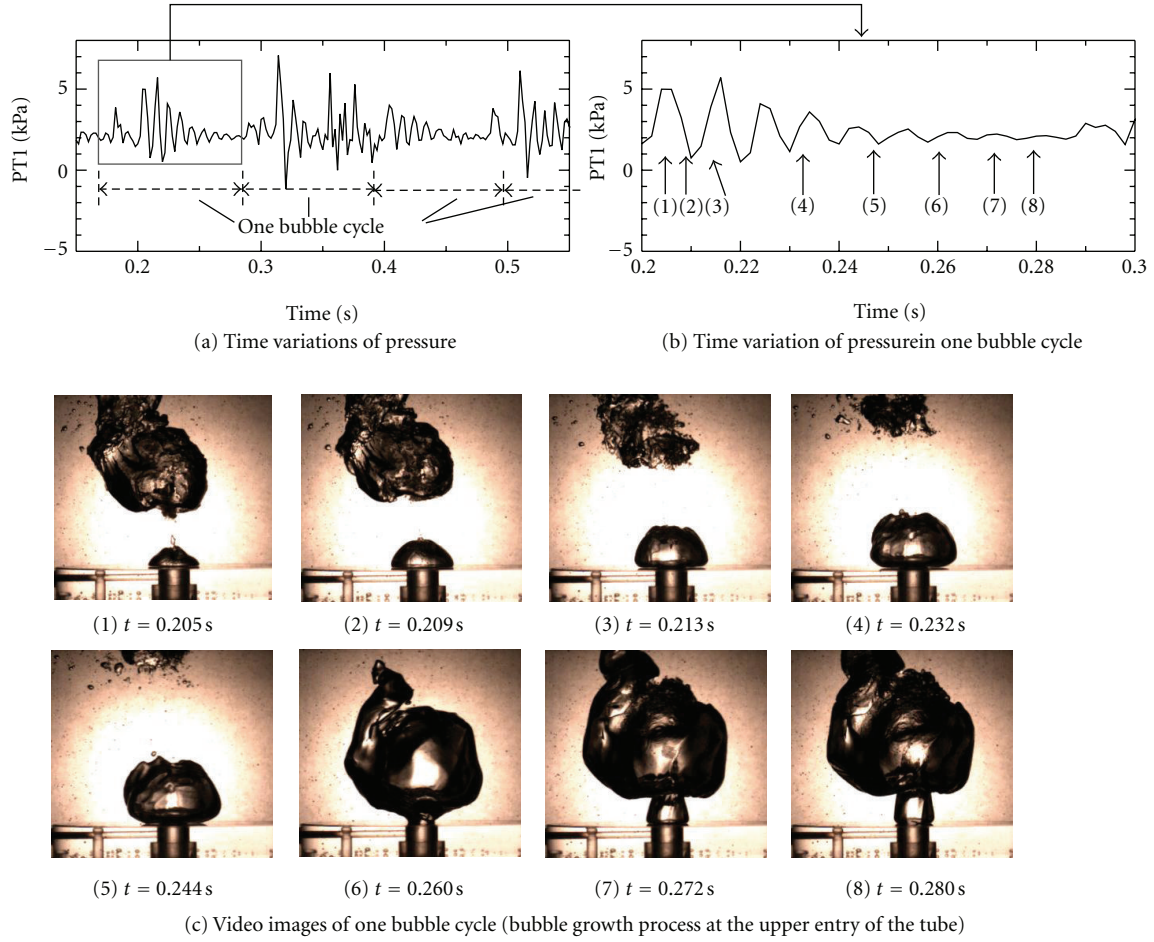


FIGURE 4: Time variations of pressure at the upper entry of the tube (PT1) and corresponding bubble formation and expansion process (tube diameter $D = 12$ mm, $J_g^{*0.5} = 0.88$, indicated as (a) in Figure 3).

$$j_l^* = j_l \sqrt{\frac{\rho_g}{gD(\rho_l - \rho_g)}}. \quad (3)$$

In (1), m and C are nondimensional constants which mainly depend on geometry, such as the liquid inlet and exit and tube diameter. In general, the value of m is equal to 1.0 approximately and the value of C lies between 0.6 to 1.0. Since most of the proposed correlations are not based on the physical mechanisms that cause flooding, a satisfactory correlation appreciable over a wide range of operating condition, fluid properties, and pipe geometry is still lacking. In addition, it is known that most analytical models used a forced balance equation for wall shear, interfacial shear, and gravity to determine a downward liquid flow rate flowing against an upward gas flow rate (Richter [2] and No and Jeong [3]). In the analysis, however, the interfacial shear force has a predominant effect on the predicted results and all established correlation for the interfacial shear were empirically obtained to be applicable to limited conditions. Therefore, even in update thermal-hydraulic computer codes like TRAC and RELAP, the Wallis-type empirical correlation

is still used with the optional constant values, m and C , to predict downward liquid flow rate.

In a laboratory scale gas/liquid countercurrent flow experiments, typical equipments consist of upper and lower plenums connected by a vertical tube, in which liquid flow downward by gravity from the upper to the lower plenum. Gas is introduced into the lower plenum and flows upward counter-currently through the vertical tube. A pool of liquid in the upper plenum above the upper end of the tube provides the liquid penetrate into downward. Investigations using this experimental configuration include those of Kaminaga et al. [4], Imura et al. [5], Bharathan and Wallis [6], and Lu et al. [7]. In this experimental configuration, although the constant static head is kept in the upper plenum, the downward liquid flow rate is not generally kept constant. The downward liquid flow rate is influenced by not only flow behavior, such as interfacial shear or wall shear in the vertical tube but also bubble dynamics, such as bubble formation, growth, and departure at the upper end of the tube. Therefore, in order to predict countercurrent flow limit, it is important to clarify the relationship between rising

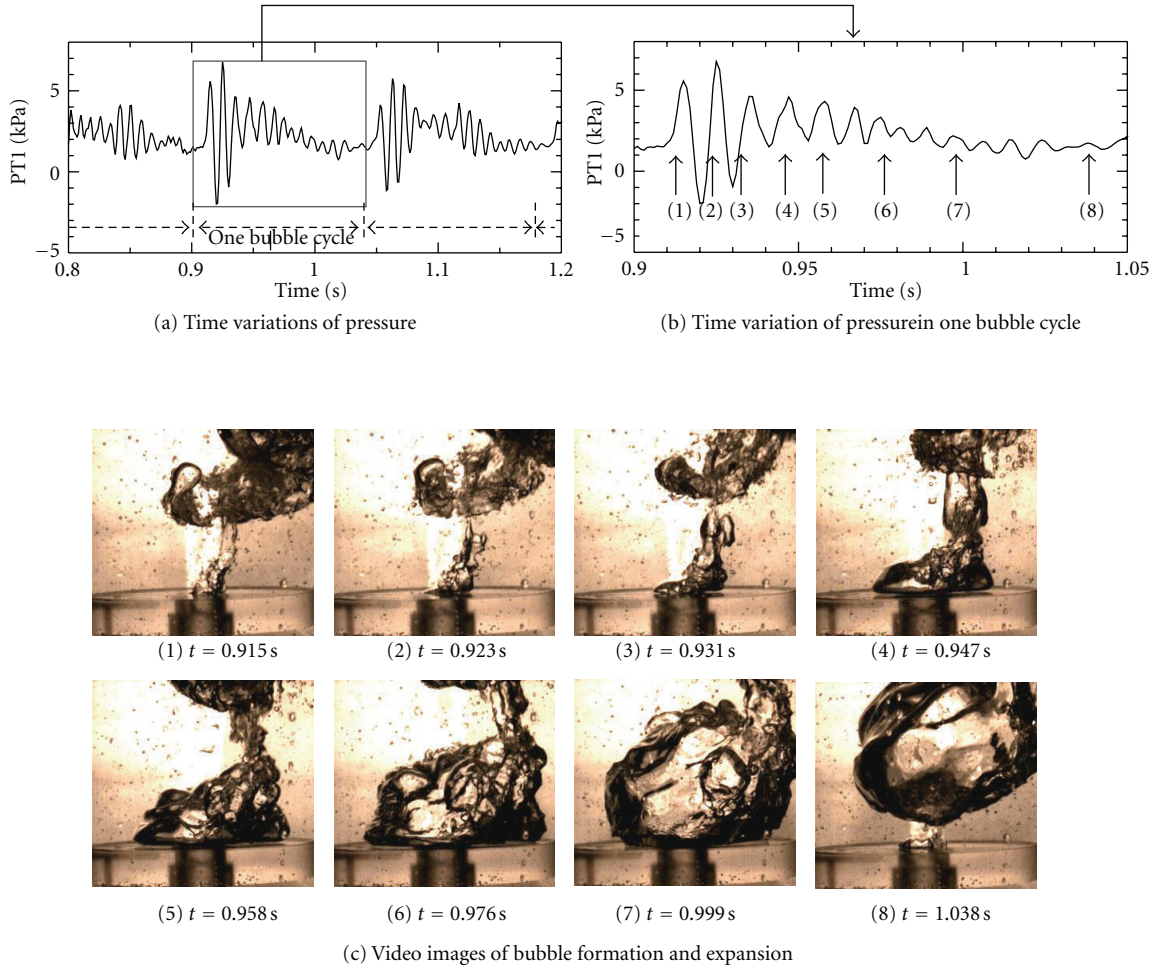


FIGURE 5: Time variations of pressure at the upper entry of the tube (PT1) and corresponding bubble formation and expansion process (tube diameter $D = 20$ mm, $j_g^{*0.5} = 0.68$, indicated as (b) in Figure 3).

bubble behavior at the upper end of the tube and downward liquid flow rate leading to flow transition.

Consequently, the purposes of this study are to experimentally examine adiabatic air/water countercurrent flow focusing on relationship between the downward liquid flow rate and behaviors of bubbles purged into the liquid pool. In this study, the experimental results from simultaneous measurements of the time variations of pressure inside the upper end of the tube and visual observations of bubble formation are presented.

2. Experimental Apparatus

A schematic diagram of the experimental apparatus is shown in Figure 1. It consists of a test tube an upper plenum, a lower plenum an air supply system, and data acquisition system. The test tube is made of circular transparent acrylic resin to facilitate visual observation and has a length of 1000 mm. The upper plenum (430 mm long, 320 mm wide, and 500 mm high) and the lower circular plenum (200 mm i.d. and 500 mm high) are interconnected by the vertical test

tube. In order to examine the tube diameter effect on bubble formation, the tubes having 12 and 20 mm in diameter were used.

For the experiments, water at 293 K (± 3 K) is pumped from a reservoir tank and is fed into the upper plenum. In the upper plenum, the water level was maintained to be constant by a weir and overflow water is fed back to the reservoir tank by gravity. The downward water flow rate through the vertical test tube was determined by collecting it in a measuring sub tank over a certain period of time. Air is directly fed to the lower plenum from the air compressor via a needle valve and air flow meter and allowed to flow upwards through the test tube.

Details of the upper and lower end geometries are shown in Figure 2. The upper end of the tube is sharp-edged geometry that a horizontal circular plate is attached at the end of the test tube. As shown in Figure 2(b), compressed air enters directly into the tapered tube bottom, through a small injection nozzle (i.d. = 4 mm) in the lower plenum. The injection nozzle is aligned accurately with the center of the vertical test tube. This air entrance section is designed to

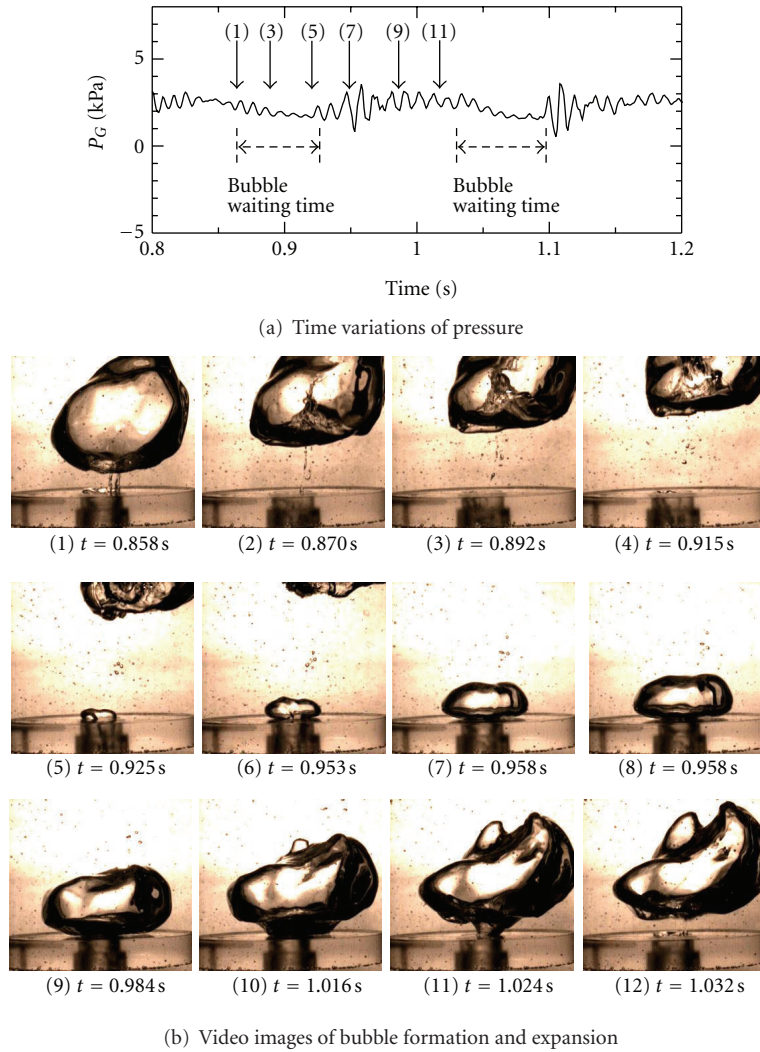


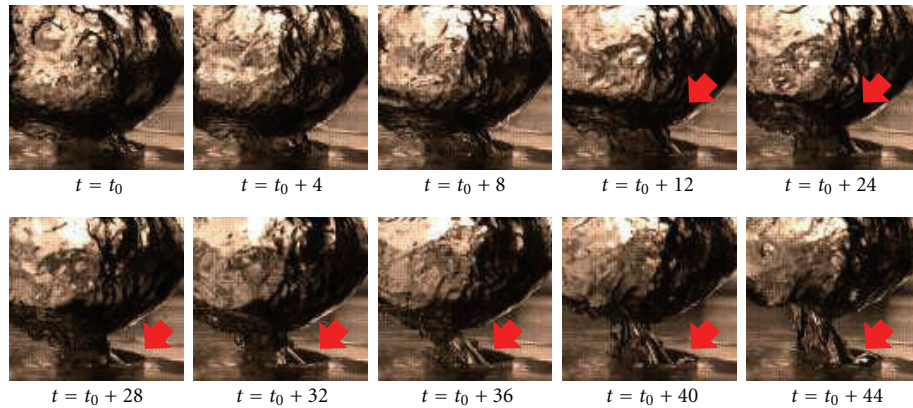
FIGURE 6: Time variations of pressure at the upper entry of the tube (PT1) and bubble formation and expansion process including waiting time (tube diameter $D = 20$ mm, $j_g^{*0.5} = 0.41$, indicated as (c) in Figure 3).

minimize the interaction between the falling water and the air near the lower end and make the flow controlled only by the flow behavior near the upper entry of the tube. The air supplied from the bottom injection nozzle goes up in the tube with a countercurrent flow regime and purged into the water pool with a large bubble regime. The water level is varied from 50 mm to 200 mm to examine an effect of the water level on a downward liquid flow rate in the CCFL condition. The water level in the upper plenum was controlled by the height of weir. In the present experiment, three different heights of weirs were used.

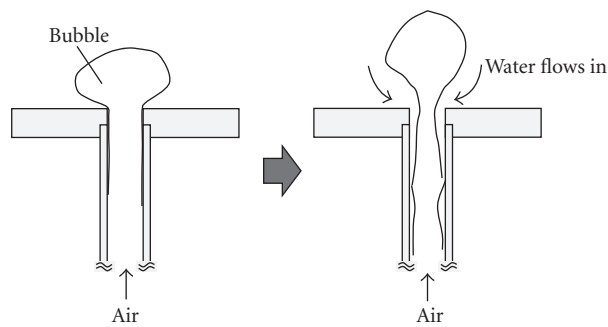
In each experiment, initially some amount of air only flows in the test section and then the water level in the upper plenum is set at a specified level to make a steady state countercurrent flow in the test section. During the steady-state, the air and downward water flow rates, the pressure at the upper entry of the tube (PT1), and the lower plenum pressure (PT2) were recorded. Both pressures of PT1 and

PT2 are measured by a piezo electric pressure transducer. Datasets of pressure are collected for a period of 40 sec with a sampling frequency of 1 kHz. Since one of the aims of the experiments is to examine the bubble characteristics in the CCFL condition, visualization experiments were also carried out using a high-speed camera. The camera was fixed on a stand very close to the upper entry of the test tube to visualize both the bubble formation process and the behavior of the water. In the present experiments, pictures were taken at a speed of 250 frames per second and a shutter rate of 1/2000. After steady-state measurements were over, the air flow rate was progressively increased by small steps. These measurements and bubble observations were conducted at several air flow rates until the reversal of the liquid flow was initiated. Initiation of liquid flow reversal was observed by naked eye.

The two pressure transducers were calibrated using digital pressure gage before experiments. The air flow meter was



(a) Video images of bubble “neck” in the detachment process (tube diameter $D = 12$ mm, $j_g^{*0.5} = 0.61$, $H = 200$ mm)



(b) Schematic of water flow at the upper entry

FIGURE 7: Video images of bubble “neck” at the upper entry of tube and sequence of water flow at the upper entry.

also calibrated using a dry-type gas flow meter. From these calibrations, the uncertainties of pressure measurements and air flow rate are $\pm 5\%$ and $\pm 7\%$, respectively. The reproducibility and uncertainties of water flow rate was confirmed by repeating the measurements under the same air flow rate. From these measurements, the uncertainties of water flow rate are $\pm 6\%$.

3. Experimental Results and Discussions

3.1. Effect of Tube Diameter. Figure 3 indicates relationship between a downward liquid flow and an upward gas flow rates. In the figure, the data are plotted in square terms of dimensionless superficial gas velocity j_g^* versus the corresponding dimensionless liquid superficial velocity j_l^* . The figure shows that, for both tubes, the slopes are almost linear throughout the entire range and can be fitted by straight lines by (1). It is clearly shown that the slopes of lines are affected by the tube diameter in the present countercurrent flow condition. The values of m and C obtained by fitting the present data with (1) were indicated in the figure.

Figure 4(a) shows typical time variations of pressure measured at the upper entry of the tube for the diameter of 12 mm. Here, the dimensionless gas velocity $j_g^{*0.5}$ was set at 0.88. As shown in this figure, there are four pressure

fluctuation cycles ranging in peak height from 4 to 7 kPa. One of pressure fluctuation cycles is shown in Figure 4(b). Some of video images at the upper entry of the tube are shown in Figure 4(c) to illustrate this bubble cycle. The corresponding video images in Figure 4(c) are indicated as (1) to (8) in Figure 4(b). It can be seen that at the initial stage of bubble formation, the bubble size gradually increases with large pressure fluctuation. The bubble gradually changes with a hemispherical shape at the upper entry surface (Figure 4(c), (1) to (3)). As the bubble size increases, the buoyancy force is dominant, and then the bubble gradually became oblate spheroid (Figure 4(c), (4) to (6)) as it rises towards upward. At this stage, the pressure fluctuation gradually decreases. It should be noted that in Figure 4(c) (6), the “neck” can be seen in the bottom of the bubble.

Figures 5(a), 5(b), and 5(c) also show time variations of pressure and video images taken for the 20 mm tube diameter. The dimensionless gas velocity $j_g^{*0.5}$ was set at 0.68. As shown in Figure 5(a), the time variation of pressure fluctuation also consists of the fluctuation cycles. One of the fluctuation cycle is shown in Figure 5(b), and some of the corresponding video images are shown in Figure 5(c). As shown in Figure 5(c), the bubble appears to be more deformed and its size became larger than that of 12 mm tube diameter. Similar to the 12 mm diameter tube, at the

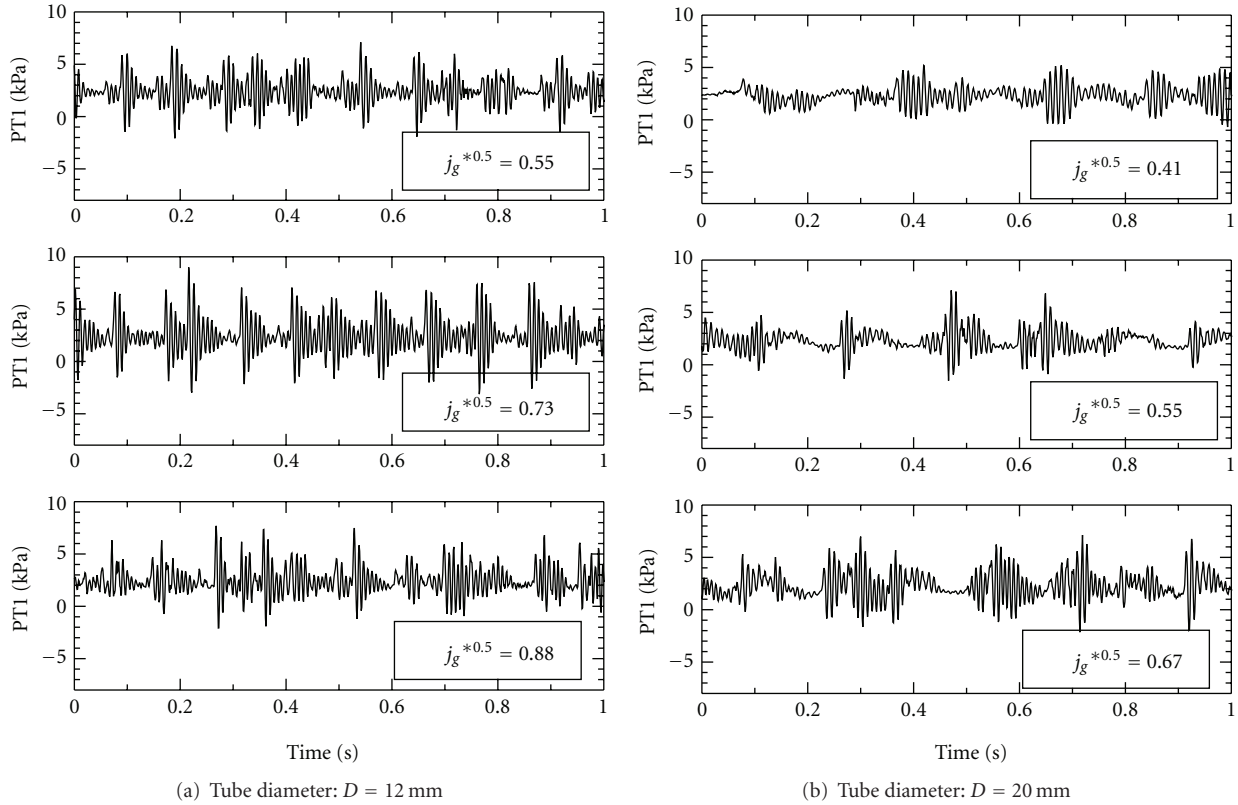


FIGURE 8: Typical time traces of pressure at the upper entry of the tube (PT1).

initial stage of the bubble growth (Figure 5(c) (1)–(5)), the pressure fluctuation is relatively large. As the bubble volume increases and it moves upward, the pressure fluctuation gradually decreased (Figure 5(c) (8)). As shown in the figure, the bubble clearly detached from the surface (Figure 5(c) (8)). This means that there is a discrete time interval between one bubble and next bubble formation. This discrete time interval, named a “waiting time,” was observed only in the 20 mm diameter tube.

Typical video images including the waiting time are shown in Figure 6. As shown in Figure 6, the waiting time (indicated as (1) to (4) in Figure 6(b)) is characterized by the period in which no bubble is newly formed into the pool. It is noted that the water enters the tube in this waiting time between the bubble detachment and an initiation of next bubble formation. In addition, the waiting time was observed especially low air flow rate condition below $j_g^{*0.5} = 0.6$.

Above observations indicate the importance of relationship between the bubble formation and the behavior of the water in the upper plenum. Particularly, the bubble deformation during detachment process is important. Figure 7(a) includes the sequence of pictures showing “neck,” where the bubble diameter gradually decreases at the tube entry. The time interval between two frames is 4 msec (1/250). Moreover, the water in the upper plenum continues to move downwards until next bubble will be formed at the upper entry. Sequence of this process is shown in Figure 7(b). When

the gas bubble fully covers the tube diameter, the water cannot penetrate into the tube. However, as the bubble volume increased and the “neck” formed during detachment process, the water in the upper plenum can flow into the test tube.

Examples of the time variations of measured pressure at the location of the upper entry of the tube (PT1) are summarized in Figure 8. Although the measured data have similar time variations, the pressure of 12 mm diameter tube indicates larger fluctuations with a high frequency than that of 20 mm diameter tube. Typical power spectral densities (PSDs) of pressure fluctuations for the 12 mm diameter tube are shown in Figure 9 for three different values of air flow rates. The PSD data are corresponding to the locations of upper entry of the tube (PT1) and lower plenum (PT2), respectively. For the case of the upper entry of the tube, it appears that as increasing the gas flow rate, the peak of PSD is observed at frequencies between 13 and 15 Hz, while for the lower plenum pressure, this maximum corresponds to a frequencies between 5 and 11 Hz. The PSD of the pressure fluctuations measured in the 20 mm diameter tube is shown in Figure 10. For the larger tube diameter, the figure clearly shows sharp distinct peak both upper and the lower pressure fluctuations. Although the time variations of measured pressure shows similar trend, the calculated values of PSD are quite different. In particular, the calculated “Power” of 20 mm diameter tube is much larger than that of 12 mm diameter tube. This fact suggests that the bubble

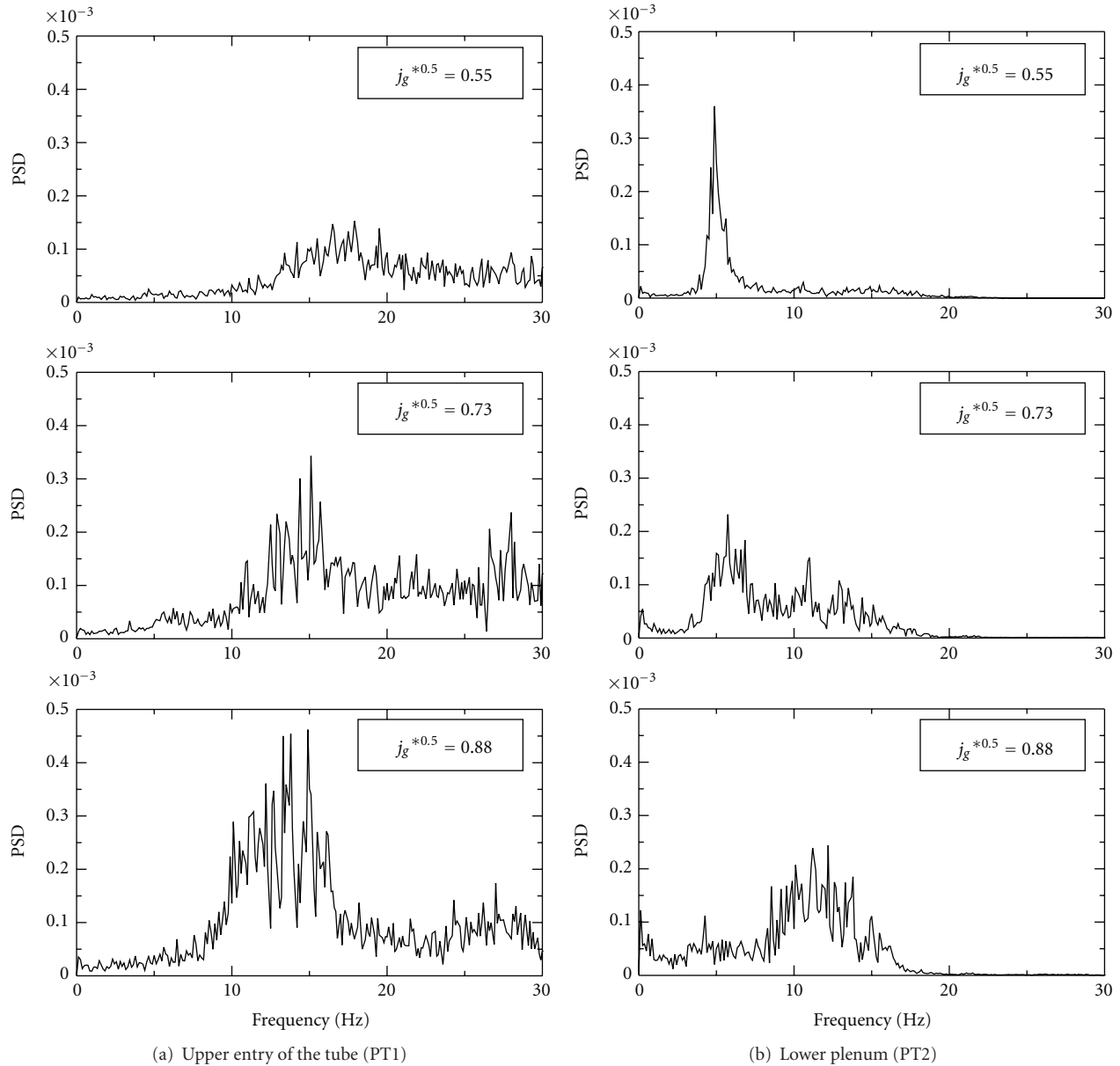


FIGURE 9: Power spectrum density (PSD) of pressure fluctuations for various air flow rate (tube diameter, $D = 12$ mm).

formation cycle of 20 mm diameter tube is more repeatedly and periodically than that of 12 mm diameter tube.

3.2. Effect of Water Level in the Upper Plenum. In order to investigate the water level effect on the downward liquid flow rate in the CCFL condition, experiments are performed for three different water levels: 50, 100, and 200 mm, respectively. For the 12 mm diameter tube, relationship between dimensionless fluxes for three different water levels is shown in Figure 11(a). It seems that the water level effect on the liquid flow rate is small at high gas flow rate. It can be seen that although the parameter C in (1) is the same, the slope of the line slightly depends on water heights. On the other hand, the m and C are almost constant for the tube

diameter of 20 mm as shown in Figure 11(b). This water level effect on downward liquid flow rate is found to occur only in the 12 mm diameter tube and not in 20 mm diameter tube. For the 20 mm diameter tube, since the bubble formation including the “waiting time” periodically occurs, the water in the upper plenum smoothly flows into the tube. Therefore, the downward liquid flow rate is not influenced by the water level in the upper plenum. On the other hand, for the 12 mm diameter tube, the downward liquid flow rate depends on the “neck” formation during bubble detachment process. Therefore, if the water level is small, the bubble reaches the free surface before the detachment occurs. Thus, the downward liquid flow rate for 12 diameter tube is affected by the water level in the upper plenum.

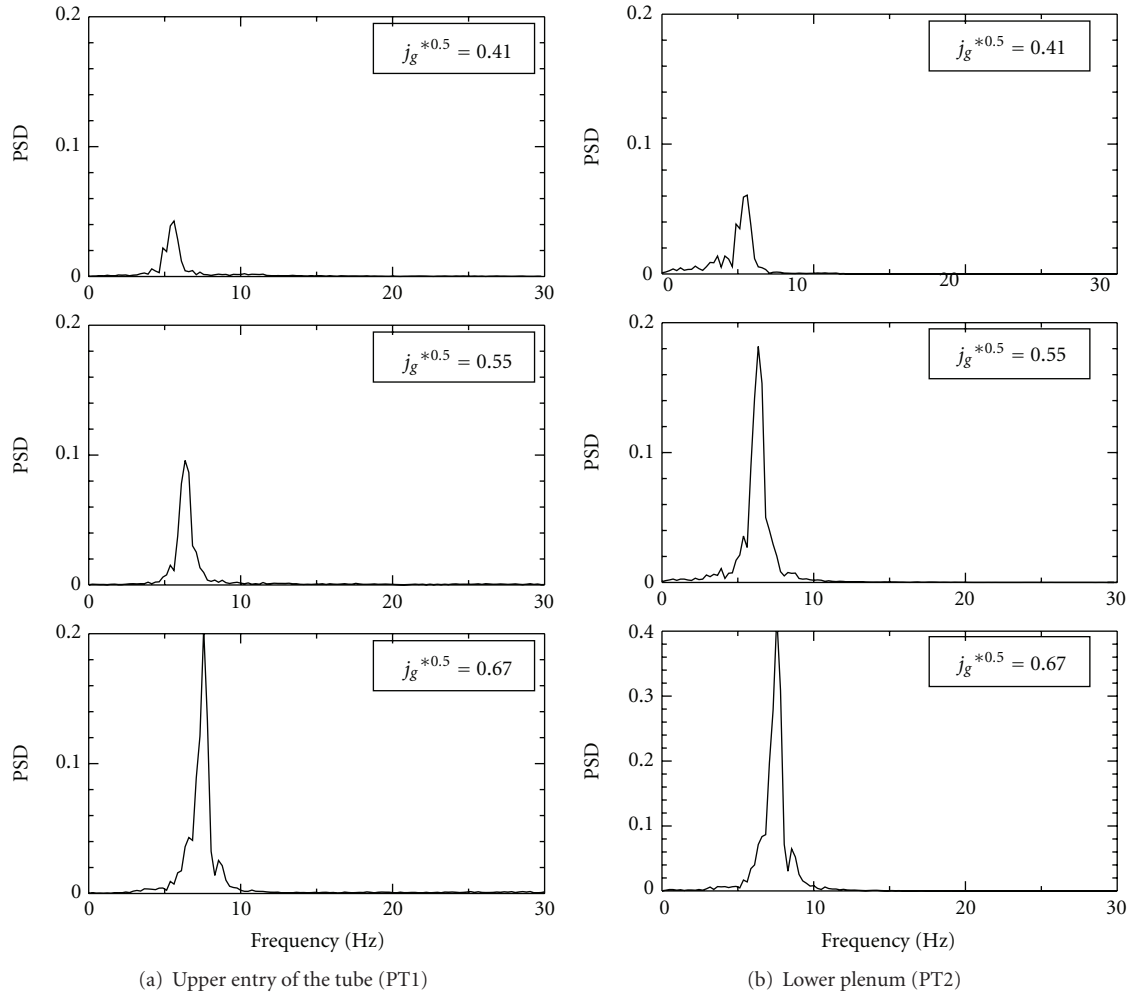


FIGURE 10: Power spectrum density (PSD) of pressure fluctuations for various air flow rate (tube diameter, $D = 20$ mm).

The pressure difference and the downward liquid flow rate measured in the 12 mm tube diameter are plotted as a function of superficial air velocity in Figure 12(a). Here, the pressure difference indicates the difference of pressure between the upper entry of the tube (PT1) and the lower plenum pressure (PT2). The figures show that the pressure difference does not change appreciably, the downward flow rate decreases gradually as increasing the gas flow rate. Since the downward liquid flow rate depends on the bubble frequency at the upper entry of the tube, it gradually decreases as increasing the superficial air velocity. In addition, since the amount of downward liquid flow rate is small for 12 mm diameter tube, the liquid film in the tube is thin, and the pressure difference ΔP may not be influenced by the air superficial velocity.

The pressure difference and downward liquid flow rate measured in the 20 mm diameter tube is also presented in Figure 12(b). It is seen that for the 20 mm diameter tube, the pressure difference gradually increases as increasing the air flow rate. The downward liquid flow rate is almost inversely proportional to air superficial velocity. Since the bubble

volume of the 20 mm tube diameter is much larger than that of the 12 mm tube diameter, the bubble detachment at the upper entry of the tube produces large pressure fluctuation in the lower plenum (PT2). Therefore, the dependence of ΔP on air superficial velocity is slightly different for two tube diameters.

Figures 13(a) and 13(b) show the power spectral density (PSD) measured in the 12 mm diameter tube for the upper entry of the tube and lower plenum, respectively. As shown in Figure 13(a), a distinct peak is not evident at the lowest air flow rate. However, as increasing the air flow rate, the peak gradually appears between 10 to 15 Hz. On the contrary, the PSD of the lower plenum indicates different tendency. When the air flow rate is relatively small, the frequency peak appears between 5 and 8 Hz. However, at the largest air flow rate, the peak is not clear except water height of 50 mm. The PSD for the 20 mm diameter tube is also shown in Figure 14 for the upper entry of the tube and the lower plenum, respectively. For this condition, it is apparent that the distinct peak clearly can be seen for all experimental conditions. The dominant

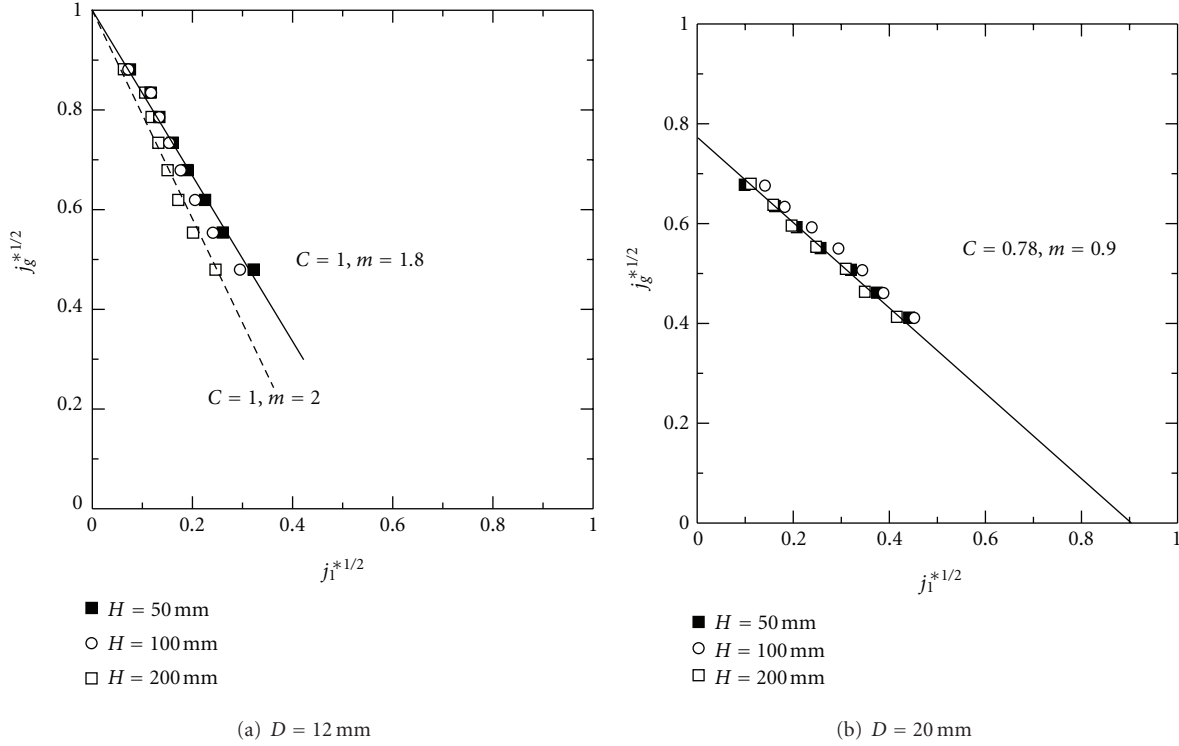


FIGURE 11: Effect of water level on dimensionless liquid flow rate against gas flow rate in CCFL condition.

frequency is slightly dependent on the water height in the upper plenum.

Figure 15 shows the dominant frequency in the PSD as a function of gas flow rate for different three water levels. The dominant frequency was calculated using least-square method in the frequency ranges below 30 Hz. According to the visual observation, the bubble formation frequency, much less than 30 Hz, therefore, this frequency range was selected. As shown in Figure 15(a), the dominant frequency in the 12 mm diameter tube decreases with increasing gas flow rate. On the contrary, as shown in Figure 15(b), the dominant frequency of 20 mm diameter tube increases as increasing the gas flow rate.

Figures 15(a) and 15(b) show that the dependence of dominant frequency on the gas flow rate is quite different for two diameter tubes. One of the reasons of this difference depends on the bubble formation cycle. As shown in Figures 5, 6, and 14, the single bubble was periodically formed for 20 mm diameter tube. On the contrary, for the 12 mm diameter tube, the bubble detachment process is very complicated and two or three bubbles coalescence was observed at the upper entry as shown in Figure 4(c) (8). It should be noted that the bubble flow pattern at the upper entry of the tube becomes more complicated one as increasing the gas flow rate.

3.3. Comparison of Bubble Frequency Data with the Prediction.
 In the present experiment, visual images show that the bubble formation, expansion, and its detachment from the upper entry of the tube apparently occurred repeatedly. It is

well known that there are number of correlations to predict the bubble formation from the orifice. Since the bubble formation significantly affects the downward liquid flow rate in the CCFL condition, the present results were compared with the proposed bubble formation correlations.

Davidson and Shuler [8] proposed the theoretical model for the periodic formation of bubbles due to the flow of gas into an inviscid liquid. The bubble formation expansion by an air injection into a pool might be controlled by forces of buoyancy, inertia due to momentum change of the liquid surrounding the bubble, drag, and surface tension. For a constant pressure condition, bubble is expanded very rapidly just after the pressure exceeds the required value for the bubble to advance into a pool. Therefore, the buoyancy and liquid inertia forces were considered in the force balance.

The buoyancy force is

$$(\rho_l - \rho_g)gV_B \approx \rho_l gV_B, \quad (4)$$

where, V_B means the bubble volume and the liquid inertia force is

$$\frac{d}{dt} \left(m \frac{ds}{dt} \right), \quad (5)$$

where s is a distance from the air injection point to a gravity center of the bubble and m is a virtual mass added to the bubble by the surrounding fluid and assumed as follows [8]:

$$m = \frac{11}{16} \rho_l V_B. \quad (6)$$

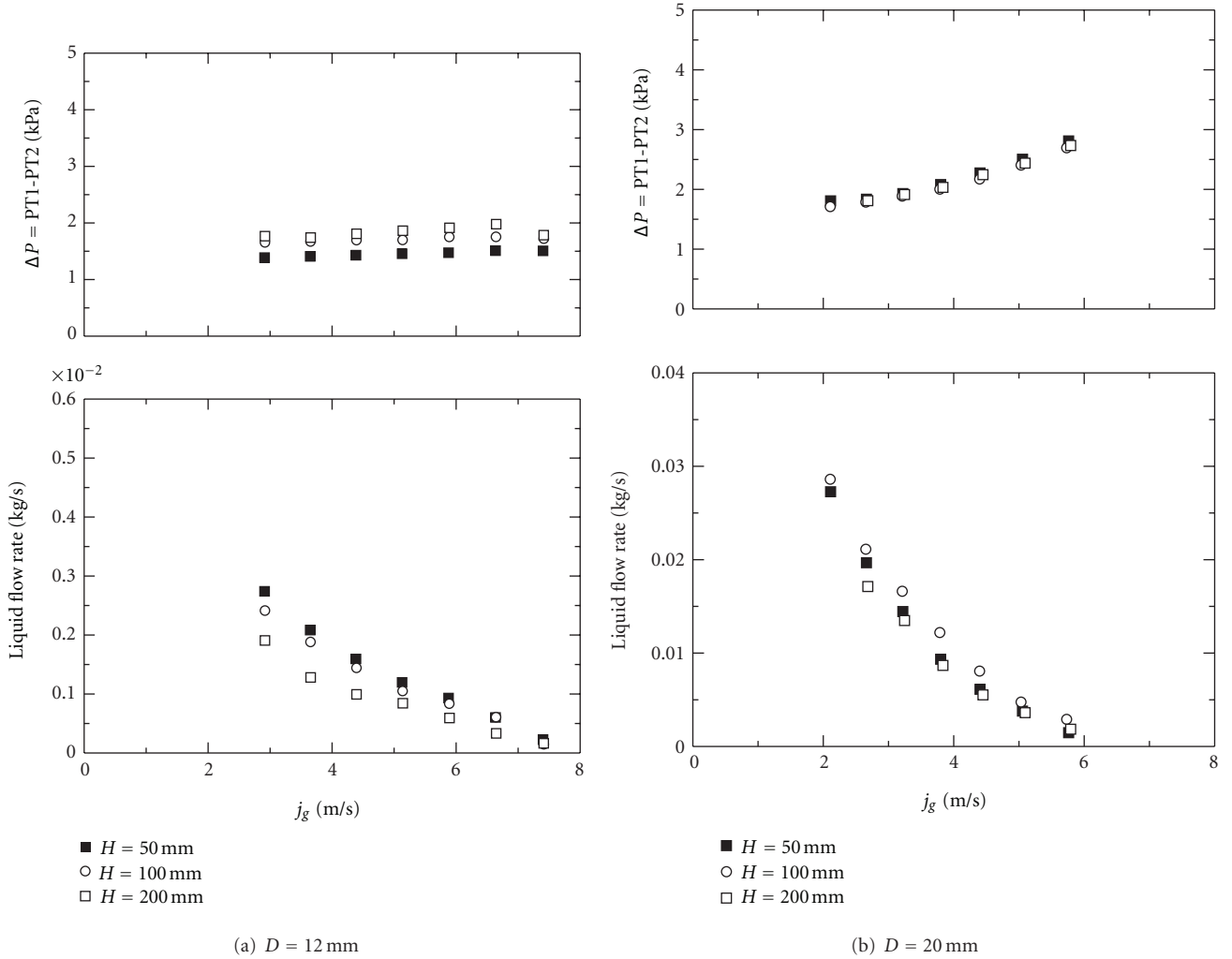


FIGURE 12: Variation of the pressure difference (PT1-PT2) and the downward liquid flow rate with superficial air flow rate for difference water level and tube diameter.

The force balance gives

$$\rho_l g V_B = \frac{d}{dt} \left(\frac{11}{16} \rho_l V_B \frac{ds}{dt} \right). \quad (7)$$

If the air flow rate is constant Q_g , then the bubble volume is given by

$$V_B = Q_g t. \quad (8)$$

Integrating the above differential equation using the initial condition that $s = 0$ and $ds/dt = 0$ when $t = 0$, the following equation for the bubble volume is obtained:

$$V_B = 1.378 Q_g^{6/5} g^{-3/5}. \quad (9)$$

Among the other bubble formation correlations, Wraith [9] proposed a simple two-stage model a plate orifice submerged in an inviscid liquid, for high gas flow rate. In his model, the first stage corresponds to the growth of a hemispherical bubble pressed to the plate by the inertial

force. When the buoyancy force becomes dominant, a second stage develops and the bubble formation is dealt with as a virtual mass problem like Davidson model. The solution for the two-stage growth model by Wraith gives the following correlation:

$$V_B = 1.090 Q_g^{6/5} g^{-3/5}. \quad (10)$$

It is interesting to note that these two models take the following form:

$$V_B = k Q_g^{6/5} g^{-3/5}, \quad (11)$$

where k is the constant coefficient.

The data obtained in the present study are compared in Figures 16(a) and 16(b) with the correlations of Davidson (7) and of Wraith (8). In order to compare the experimental results with the correlations, an average volume of one detached bubble was calculated by following equation:

$$V_B = \frac{Q_g}{f}, \quad (12)$$

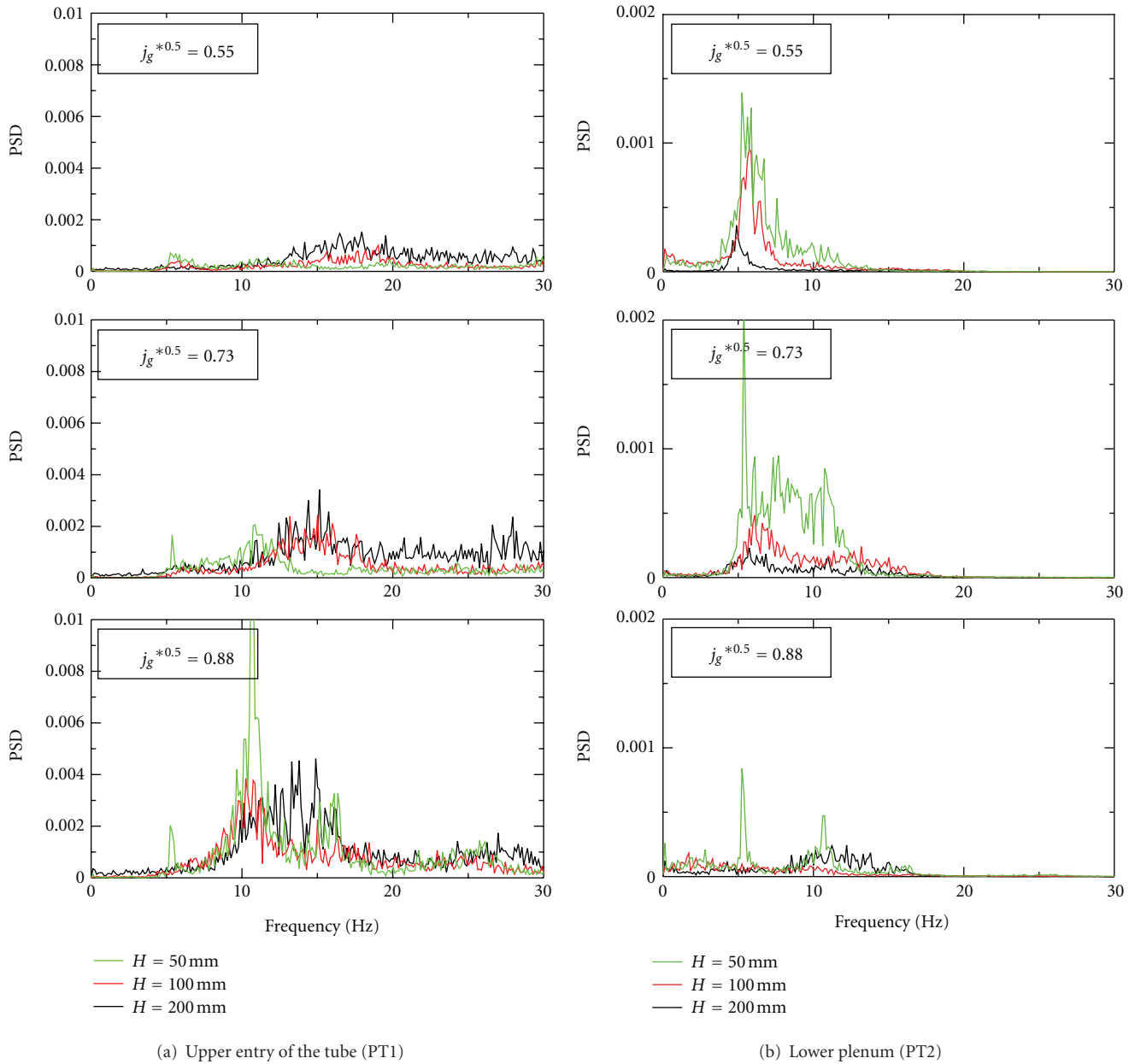


FIGURE 13: Power spectrum density (PSD) of pressure fluctuations for various air flow rates and water levels (tube diameter $D = 12$ mm).

where Q_g is the gas volumetric flow rate (cm^3) and f is the dominant frequency of the pressure fluctuations in the upper entry of the tube. The figure shows that measured bubble volumes increase monotonically with the gas flow rate. Figure 16(a) shows the data for 12 mm diameter tube, and it can be seen that Wraith correlation by (10) agree: with the data for water level of 100 mm and 200 mm. However, as shown in the figure, (9) and (10) slightly underestimate the data of the water level of 50 mm. The data in the 20 mm diameter tube are compared in Figure 16(b); the slope of the analytical relation is a little larger than the measured one and at a lower gas flow rate it underestimates the bubble volume and that the data

gradually approach the analytical relation, and at a larger gas flow rate, the analysis can give a fairly good prediction. The calculated dominant frequency of 20 mm diameter tube includes the bubble “waiting time” in which no bubbles are formed at the tube entry. Therefore, in order to evaluate the detached bubble volume more precisely, the influence of bubble waiting time on pressure fluctuation should be well understood.

4. Conclusions

An experimental study has been conducted to study the Counter Current Flow Limitation in the tubes of 12 mm and

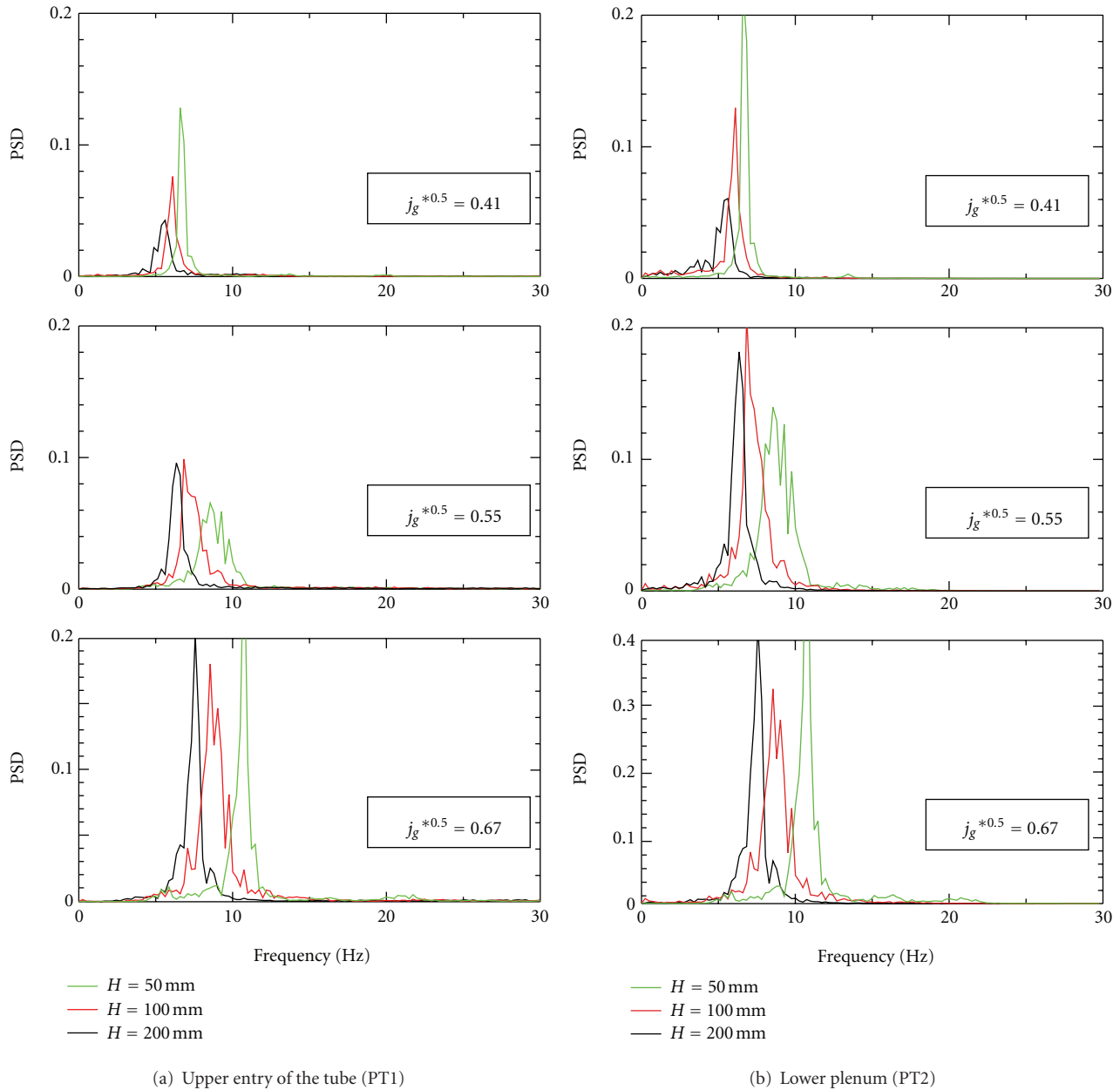


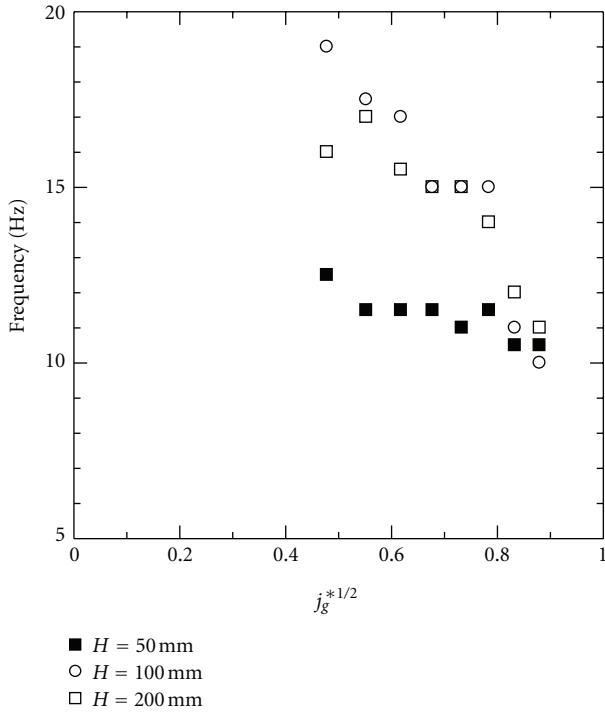
FIGURE 14: Power spectrum density (PSD) of pressure fluctuations for various air flow rates and water levels (tube diameter $D = 20$ mm).

20 mm diameter. The pressures at the upper entry of the tube, lower plenum, and downward falling liquid flow rate were measured over a range of liquid and air flow rates. In addition, the relationship between the downward liquid flow and behaviors of bubbles purged into the liquid pool in the CCFL condition was also investigated using high-speed video camera. The following conclusions were made.

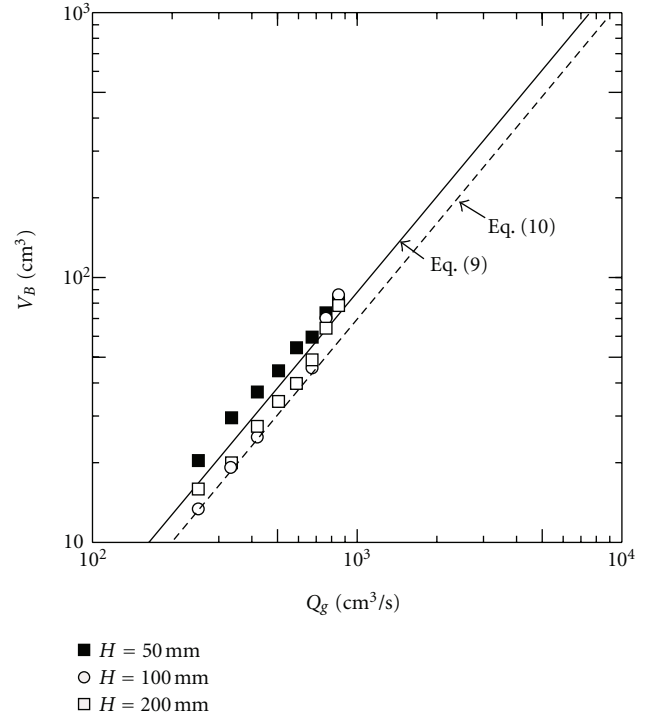
(1) The CCFL superficial velocities of gas and liquid obtained in the present experiments for two different diameter tubes are predicted well by correlation of Wallis. The water level in the upper plenum slightly affects the slope of the curve for the 12 mm i.d. tube, especially at low gas flow rate. On the other hand, for the 20 mm i.d. diameter tube, the

slope of the curve is not affected by the water depth in the upper plenum.

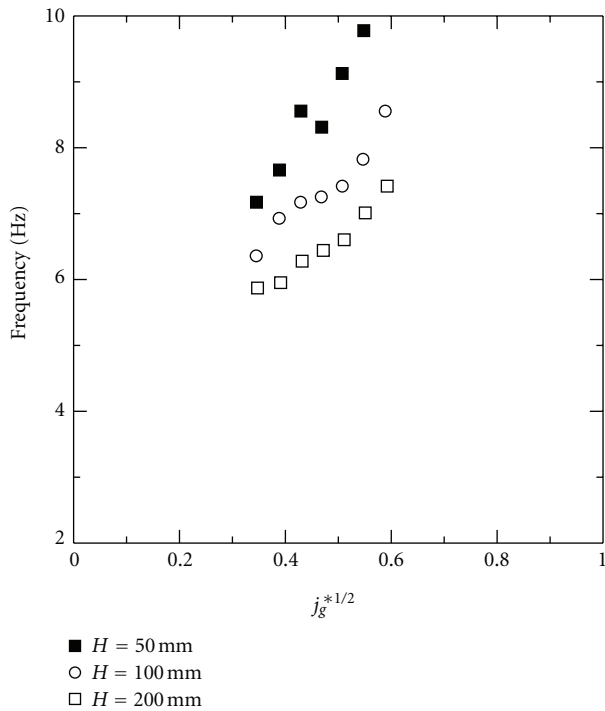
(2) The “bubble one cycle” at the upper entry of the tube corresponds to characteristic one pressure fluctuation cycle. In this bubble cycle, the bubble growth, coalescence, and detachment at the upper entry of the tube were clearly observed. The bubble detachment process is quite different for two diameter tubes. For the 12 mm diameter tube, the formation of the “neck” during bubble detachment is important for evaluating the downward liquid flow rate. On the contrary, for the 20 mm diameter tube, a “waiting time” in which no bubble is observed at the upper entry is important to evaluate the downward liquid flow rate.



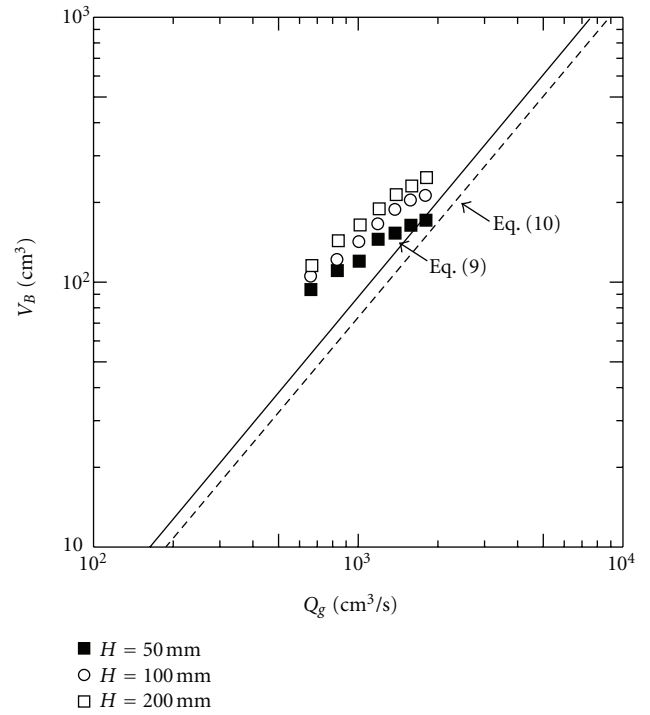
(a) $D = 12$ mm



(a) $D = 12$ mm



(b) $D = 20$ mm



(b) $D = 20$ mm

FIGURE 15: Relationship between dominant frequency of bubble formation and dimensionless air superficial velocity.

FIGURE 16: Comparison of present experimental data with proposed correlations for bubble formation.

(3) The detaching bubble volume is predicted well by Davidson and Wraith correlations for 12 mm diameter tube. However, for the tube diameter of 20 mm, the correlations underestimate the experimental bubble volume especially at the low air flow rate. In the present experiments, the data for 20 mm diameter tube include the effect of “waiting time,” therefore, the calculated bubble frequency may be affected by this characteristic period. It should be noted that the waiting time may be a favorable period for a liquid introduction into the test tube from the upper plenum.

References

- [1] G. B. Wallis, *One-Dimensional Two-Phase Flow*, McGraw Hill, New York, NY, USA, 1969.
- [2] H. J. Richter, “Flooding in tubes and annuli,” *International Journal of Multiphase Flow*, vol. 7, no. 6, pp. 647–658, 1981.
- [3] H. C. No and J. H. Jeong, “Flooding correlation based on the concept of hyperbolicity breaking in a vertical annular flow,” *Nuclear Engineering and Design*, vol. 166, no. 2, pp. 249–258, 1996.
- [4] F. Kaminaga, K. Matsumura, A. Ouchi, and Y. Shibata, “Study on relationship between rising gas bubble and falling liquid flow in CCFL condition,” in *Proceedings of the 6th International Conference on Nuclear Engineering (ICONE '98)*, 1998.
- [5] H. Imura, H. Kusuda, and S. Funatsu, “Flooding velocity in a counter-current annular two-phase flow,” *Chemical Engineering Science*, vol. 32, no. 1, pp. 79–87, 1977.
- [6] D. Bharathan and G. B. Wallis, “Air-water countercurrent annular flow,” *International Journal of Multiphase Flow*, vol. 9, no. 4, pp. 349–366, 1983.
- [7] D. C. Lu, N. S. Liao, and K. H. Wu, “Experimental investigation of counter-current steam-water flooding in a vertical circular pipe,” in *Proceedings of the ASME-JSME Thermal Engineering Joint Conference*, vol. 1, pp. 243–249, Honolulu, Hawaii, USA, 1983.
- [8] J. F. Davidson and B. O. G. Shuler, “Bubble formation at an orifice in an inviscid liquid,” *Transactions of the Institute of Chemical Engineers*, vol. 38, pp. 335–342, 1960.
- [9] A. E. Wraith, “Two stage bubble growth at a submerged plate orifice,” *Chemical Engineering Science*, vol. 26, no. 10, pp. 1659–1671, 1971.

Research Article

VOF Calculations of Countercurrent Gas-Liquid Flow in a PWR Hot Leg

M. Murase,¹ A. Tomiyama,² I. Kinoshita,^{1,2} Y. Utanohara,¹ Chihiro Yanagi,¹
T. Takata,³ and A. Yamaguchi³

¹Institute of Nuclear Technology, Institute of Nuclear Safety System, Inc., 64 Sata, Mihama-cho, Mikata-gun, Fukui 919-1205, Japan

²Department of Mechanical Engineering, Kobe University, 1-1 Rokkodai, Nada-ku, Kobe, 657-8501, Japan

³Department of Sustainable Energy and Environmental Engineering, Osaka University, 2-1 Yamadaoka, Suita-shi, Osaka 565-0871, Japan

Correspondence should be addressed to M. Murase, murase@inss.co.jp

Received 11 October 2011; Accepted 9 November 2011

Academic Editor: Deendarlianto

Copyright © 2012 M. Murase et al. This is an open access article distributed under the Creative Commons Attribution License, which permits unrestricted use, distribution, and reproduction in any medium, provided the original work is properly cited.

We improved the computational grid and schemes in the VOF (volume of fluid) method with the standard $k - \epsilon$ turbulent model in our previous study to evaluate CCFL (countercurrent flow limitation) characteristics in a full-scale PWR hot leg (750 mm diameter), and the calculated CCFL characteristics agreed well with the UPTF data at 1.5 MPa. In this paper, therefore, to evaluate applicability of the VOF method to different fluid properties and a different scale, we did numerical simulations for full-scale air-water conditions and the 1/15-scale air-water tests (50 mm diameter), respectively. The results calculated for full-scale conditions agreed well with CCFL data and showed that CCFL characteristics in the Wallis diagram were mitigated under 1.5 MPa steam-water conditions comparing with air-water flows. However, the results calculated for the 1/15-scale air-water tests greatly underestimated the falling water flow rates in calculations with the standard $k - \epsilon$ turbulent model, but agreed well with the CCFL data in calculations with a laminar flow model. This indicated that suitable calculation models and conditions should be selected to get good agreement with data for each scale.

1. Introduction

Reflux condensation by steam generators (SGs) is considered as one of the possible core cooling methods under hypothetical accident conditions in pressurized water reactors (PWRs). In the reflux condensation, the steam generated in the core and the water condensed in the SG form a countercurrent flow in a hot leg, which consists of a horizontal pipe, an elbow and an inclined pipe. As reviewed by Al Issa and Macian [1], many experiments have been conducted to investigate the countercurrent flow limitation (CCFL) in the hot leg, and empirical correlations were proposed using Wallis parameters [2]. The review showed that many differences between CCFL data were simply due to geometrical effects. To compare CCFL characteristics in hot leg models, Vallée et al. [3] selected three geometrical factors, which were the horizontal pipe length to diameter ratio (L_H/D), the inclined pipe length to diameter ratio (L_I/D),

and the elbow angle θ . They showed that even for similar geometrical factors there was clear deviation between CCFL characteristics due to scale effects. Moreover, effects of fluid properties on CCFL characteristics in a hot leg have not been clearly discussed. Therefore, in order to evaluate effects of scale and fluid properties better, numerical simulation using CFD (computational fluid dynamics) software is expected to be useful.

In order to investigate effects of scale and fluid properties on CCFL characteristics in hot leg models, we have done numerical simulations using a two-fluid model and a VOF (volume of fluid) method implemented in the CFD software, FLUENT6.3.26. We found that the two-fluid model could reproduce CCFL characteristics under low pressure conditions and we confirmed that those in the hot leg could be well correlated with the Wallis parameters in the region of $50 \text{ mm} \leq D \leq 750 \text{ mm}$ [4]. The two-fluid model, however, did not give good results for a large gas density. On the

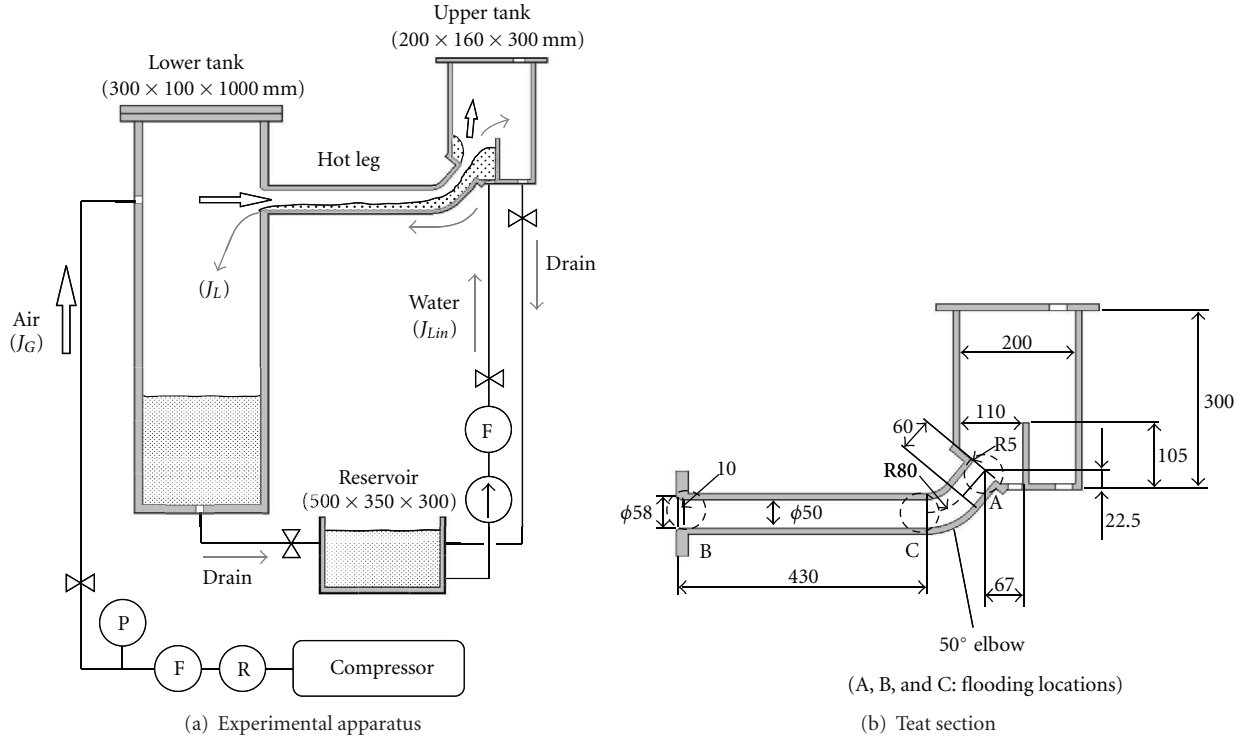


FIGURE 1: Experimental apparatus and test section used by Minami et al. [8] (unit: mm).

other hand, the VOF method could reproduce the effects of fluid properties on CCFL characteristics in a rectangular channel [5], but could not simulate CCFL characteristics in a circular channel. Therefore, the computational grid and schemes were improved in the VOF method [6], and the CCFL characteristics calculated for full-scale conditions agreed well with the UPTF data [7] at 1.5 MPa.

In this paper, in order to evaluate applicability of the VOF method to different fluid properties and a different scale, we did numerical simulations using the VOF method employed in the previous study [6] for full-scale air-water conditions (750 mm diameter) and the 1/15-scale air-water tests (50 mm diameter) reported by Minami et al. [8], respectively.

2. Summary of Previous Studies

In this section, major results of previous studies are summarized and subjects of our own studies are described.

CCFL characteristics in a PWR hot leg are generally expressed by using the Wallis correlation or Wallis parameters which are, respectively, defined by [2]

$$(J_G^*)^{1/2} + m(J_L^*)^{1/2} = C \quad (1)$$

$$J_k^* = J_k \left\{ \frac{\rho_k}{g \cdot \ell \cdot (\rho_L - \rho_G)} \right\}^{1/2}, \quad (2)$$

$$\ell = D \text{ or } H \quad (k = G \text{ or } L),$$

where J (m/s) is the volumetric flux in the hot leg, m and C are empirical constants, ℓ (m) is the characteristic length,

D (m) is the diameter of the hot leg, H (m) is the height of a hot leg model with a rectangular channel, g (m/s^2) is the gravity acceleration, and ρ (kg/m^3) is the density.

2.1. Experimental Studies. Al Issa and Macian [1] classified CCFL data according to the horizontal pipe length to diameter ratio into four groups: $(L_H/D) = 0-5$, $5-10$, $10-25$, and >40 . However, they did not clearly distinguish (1) locations of flooding and (2) onset of flooding or CCFL.

Minami et al. [8] observed three flooding locations using the 1/15-scale model (50 mm diameter) shown in Figure 1; they were (A) the upper end of the inclined pipe (i.e., water inlet into the hot leg); (B) the gas inlet into the hot leg; (C) the horizontal pipe near the elbow. Flooding at (A) appeared only under large feed water flow rates in the process of increasing air flow rates, and onset of flooding conditions (i.e., test conditions of J_G and J_{Lin} at initiation of flooding) and CCFL characteristics under the quasisteady state (i.e., relationship between J_G and J_L) after onset of flooding were different. When they were different, hysteresis between increasing and decreasing air flow rates appeared. Continuously increasing the air flow rate with flooding at (A) caused a flow pattern transition in the hot leg and flooding in (C). Falling water flow rate (J_L) under the quasisteady state was much smaller in flooding in (C) than that at (A). Flooding at (B) appeared only under relatively small feed water flow rates and large air flow rates in the process of increasing air flow rates, and it caused a flow pattern transition in the hot leg and flooding in (C). Under the quasisteady state after onset of flooding at (B), falling water flow rate became zero ($J_L = 0$) due to the

TABLE 1: Test section dimensions and conditions.

Reference	D (mm)	L_H/D (-)	L_I/D (-)	θ (deg)	Fluids	Pressure (MPa)
Richter et al. [10]	203.2	4.5	0	45	Air-Water	0.1
Ohnuki et al. [11]	25.4	9.1	1.2	50	Air-Water	0.1
Mayinger et al. [7]	750	9.0	1.1	50	Stream-Water	0.3, 1.5
Geffraye et al. [12]	351	7.5	3.0	50	Air-Water	0.1
Navarro [9]	54	9.3	1.9	50	Air-Water	0.1
Minami et al. [8]	50	8.4	1.2	50	Air-Water	0.1

D : diameter, L_H : length of horizontal pipe, L_I : length of inclined pipe, θ : angle of elbow.

large air flow rate at onset of flooding. Therefore, CCFL characteristics at the gas inlet were measured only under limited conditions. In the process of decreasing air flow rates, flooding in (C) continued, and deflooding conditions and CCFL characteristics agreed well with each other. The similar hysteresis between increasing and decreasing air flow rates was observed by Navarro [9]. In a PWR hot leg with the expansion of the inclined pipe, which was not simulated in Figure 1, flooding at (A) may not appear due to mitigation of CCFL with a large flow area and low gas velocity [4]. In most experimental studies, focus was on CCFL characteristics due to flooding in (C).

Vallée et al. [3] selected experimental studies using the horizontal pipe length to diameter ratio of $(L_H/D) = 7-10$ to compare CCFL characteristics in hot leg models. Major test conditions in previous studies are listed in Table 1. The empirical constant C in (1) by Richter et al. [10] was about 0.7 and CCFL was mitigated compared with other cases where C was about 0.6, because the horizontal pipe length to diameter ratio (L_H/D) was small. On the other hand, the empirical constant C by Ohnuki et al. [11] was about 0.55 and CCFL became severe compared with other cases, because the diameter of 25.4 mm was too small. Therefore, CCFL data applicable to a PWR hot leg, which is our interest, are limited.

2.2. Numerical Studies. Wang and Mayinger [13] conducted two-dimensional analyses of countercurrent flows in the hot leg of the UPTF tests [7] using a Euler-Euler model. They gave boundary conditions at the inlet and outlet of the hot leg, which might affect the calculated flow patterns in the hot leg. Minami et al. [14] conducted numerical simulations using the CFD software FLUENT6.3.26 and an Euler-Euler model (i.e., two-fluid model) for countercurrent air-water tests using a 1/5-scale rectangular channel. Flow patterns in the hot leg were not reproduced by two-dimensional calculations due to effects of the wall friction but were successfully reproduced by three-dimensional calculations including the lower and upper tanks. Deendarlianto et al. [15] conducted numerical simulations using the CFD software ANSYS CFX 12.0 and a Euler-Euler model for countercurrent air-water tests using a 1/3-scale rectangular channel [3]. Good agreement with data was obtained for the transition process from flooding at the gas inlet to flooding in the horizontal section near the elbow. The computational grid consisted of 248,610 hexahedral elements and 281,076 nodes, and a long computer time was generally needed.

The objectives of our studies were to find a practical numerical method for sensitivity analyses and to evaluate effects of scale and fluid properties on CCFL characteristics in the hot leg. Based on the CCFL data from air-water tests with the diameter of 50 mm [8] and CCFL characteristics calculated for a full-scale model with the diameter of 750 mm using the two-fluid model, we proposed the following correlation for low pressures below 0.3 MPa [4]:

$$(J_G^*)^{1/2} = 0.608 - 0.238(J_L^*)^{1/2} - 1.28(J_L^*). \quad (3)$$

Figure 2 compares (3) with CCFL data listed in Table 1 and values calculated by the two-fluid model. The correlation by Navarro [9], derived from air-water tests (54 mm diameter), was very close to (3). There were no significant differences between CCFL characteristics obtained under the conditions of $7.5 \leq L/D \leq 9.3$ (cf. Table 1) and $50 \text{ mm} \leq D_h \leq 750 \text{ mm}$. In the UPTF tests, the diameter of the hot leg was $D = 750 \text{ mm}$, and the hydraulic diameter in the region with the ECC (emergency core cooling) injection tube was $D_h = 650 \text{ mm}$. In Figure 2, CCFL characteristics at 0.3 MPa evaluated using $D_h = 650 \text{ mm}$ in (2) are shown. As shown in Figure 2(b), the two-fluid model reproduced CCFL characteristics under low pressure conditions using the same correlation for interfacial drag coefficients. The two-fluid model, however, greatly underestimated falling water flow rates at 1.5 MPa compared with the UPTF data [7] at 1.5 MPa.

In order to evaluate effects of fluid properties on CCFL characteristics, we improved the computational grid and schemes in the VOF method [6] and compared the CCFL characteristics calculated for full scale conditions with the UPTF data [7] at 1.5 MPa. Good agreement was obtained between them. In order to fit the calculated falling water flow rate with one UPTF data point at 1.5 MPa; however, the maximum value of the turbulent viscosity ratio was changed from the default value of 10^5 in FLUENT6.3.26 to 10^4 [6]. Therefore, the applicability of the VOF method to different fluid properties should be confirmed.

In this paper, we first did numerical simulations for full-scale air-water conditions (750 mm diameter), and compared the calculated CCFL characteristics with (3) to evaluate the applicability of the VOF method to different fluid properties. And then, to evaluate applicability of the VOF method to a different scale, we did numerical simulations for the 1/15-scale air-water tests with the diameter of 50 mm [8].

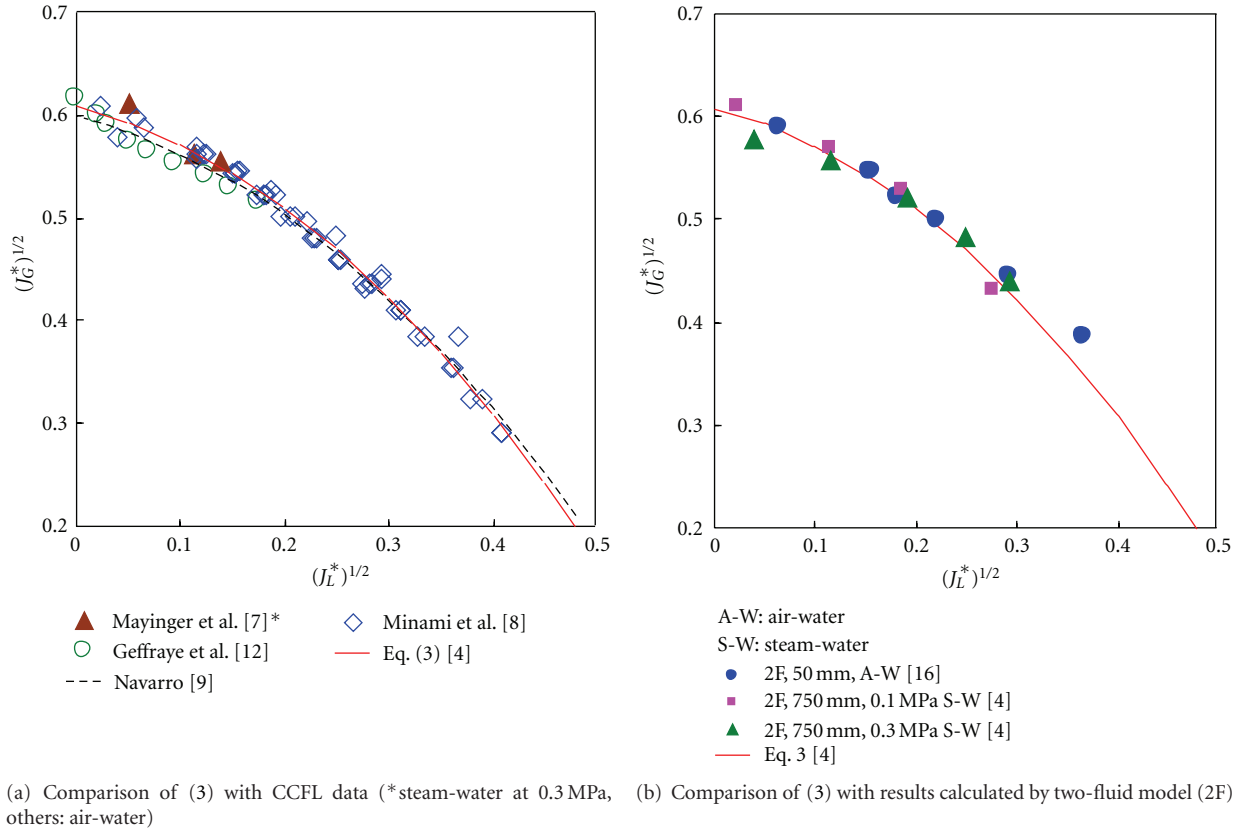


FIGURE 2: CCFL characteristics.

3. Simulation Method

In numerical simulations, the VOF method implemented in the CFD software FLUENT6.3.26 was used. The computational grid and schemes we used were the same as those in our previous report [6].

3.1. Computational Grid. Figure 3 shows the computational grid for the 1/15-scale hot leg model shown in Figure 1, which was reduced from the computational grid for a full-scale PWR hot leg [6]. Because velocity distributions of gas and liquid at both ends of the hot leg affect hydraulic behavior, the calculation region included the lower tank simulating the upper plenum in the reactor vessel and the upper tank simulating the SG inlet plenum. The expansion of the inclined pipe was not simulated in the experimental apparatus but was simulated in the grid shown in Figure 3. There were 299 calculation cells in the cross-section of the hot leg, and about 59,000 calculation cells in total. The diameter of the hot leg and the length of the horizontal pipe were $D = 50$ mm and $L_H = 420$ mm ($L_H/D = 8.4$). The length of the tapered section was not included in the length of the horizontal pipe. Gas was supplied from the side wall into the lower tank and flowed into the upper tank through the hot leg. Water was supplied from the bottom of the upper tank. Some water gravitationally flowed into the lower tank through the hot leg. The water flow rate through the hot leg was calculated from the increasing rate of water volume in

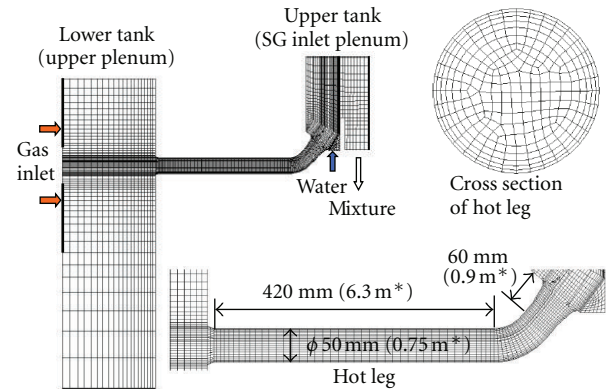


FIGURE 3: Computational grid (*full scale).

the lower tank. The boundary condition of constant velocity was used at the inlets of gas and water, and the boundary condition of constant pressure was used at the outlet of the gas-water mixture.

3.2. Computational Schemes. The standard $k - \varepsilon$ turbulent model was used for the gas and liquid phases. On wall surfaces, conditions of nonslip and the standard wall function were used. Momentum, volume fraction, turbulent kinetic energy, and turbulent dissipation rate of the gas and liquid phases were calculated using the first-order upwind

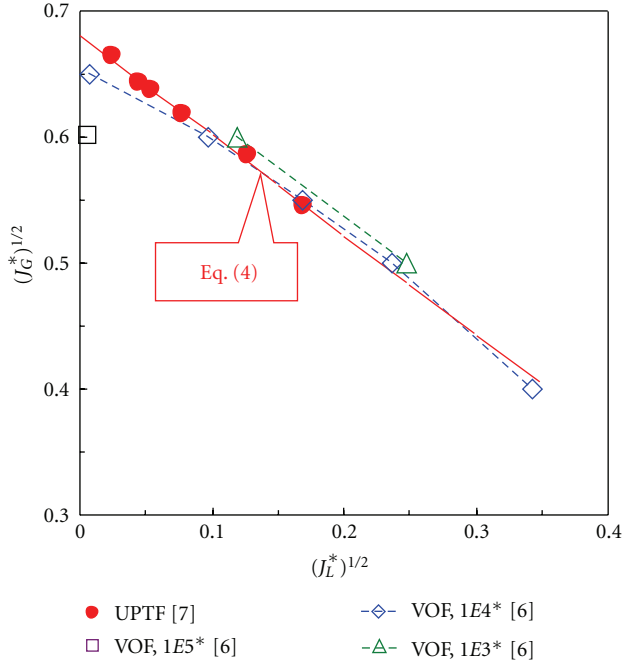


FIGURE 4: CCFL characteristics at 1.5 MPa (*maximum turbulent viscosity ratio).

scheme. For the pressure-velocity coupling, the PISO method implemented in FLUENT6.3.26 and the noniterative time advancement with the neighbor correction of 3 were used. The variable time step was used. The time step was on the order of 0.1 ms for low pressures. In order to fit the calculated falling water flow rate with one UPTF data point at 1.5 MPa, the maximum value of the turbulent viscosity ratio was changed from the default value of 10^5 in FLUENT6.3.26 to 10^4 [6].

4. Calculated Results

Numerical simulations for full-scale air-water conditions (750 mm diameter) were first conducted, and the calculated CCFL characteristics were compared with (3) to evaluate the applicability of the VOF method to different fluid properties. And then, numerical simulations for the 1/15-scale air-water tests (50 mm diameter) [8] were conducted to evaluate applicability of the VOF method to a different scale.

4.1. Full-Scale Condition Results. The maximum value of the turbulent viscosity ratio is 10^5 in the default values of FLUENT6.3.26. However, the maximum value of 10^4 was used to get good agreement with the UPTF data [7] at 1.5 MPa as shown in Figure 4. VOF calculations were done for steam-water flows at 1.5 MPa under PWR full-scale conditions with the diameter of 0.75 m [6]. For UPTF data, the hydraulic diameter of $D_h = 0.65$ m in the region with the ECC injection tube was used in (2) because flooding might occur in the region. CCFL characteristics at 1.5 MPa were fitted by

$$(J_G^*)^{1/2} = 0.68 - 0.79(J_L^*)^{1/2}. \quad (4)$$

From the results in Figure 4, the maximum value of 10^4 was used for the turbulent viscosity ratio in the following VOF calculations.

In order to evaluate capability to predict effects of fluid properties on CCFL characteristics, VOF calculations were conducted for air-water conditions at 0.1 MPa, where many experiments simulating a PWR hot leg have been carried out. Figure 5 compares flow patterns calculated by the VOF method with a flow pattern observed in the 1/15-scale air-water tests [8]. Under flooding conditions in the tests, the water flow rate was restricted at the elbow side of the horizontal pipe. In the elbow and inclined pipe, large waves with droplets periodically flowed upward, water flowed downward from the upper tank, and recirculation of water with bubbles and droplets formed. Therefore, the observed flow pattern fluctuated in the elbow and inclined pipe. The calculation conditions were for air-water in a full-scale hot leg and different from the test conditions. However the calculated flow patterns were similar to the observed flow pattern. Comparing with the 1/15-scale tests, gas volumetric fluxes J_G were larger due to a large diameter. Stable stratified flow formed in the horizontal pipe because small waves could not be calculated with the rather large calculation cells used. A large wave periodically appeared near the elbow and the water flow rate was restricted there. With increasing J_G , water depth became shallow in the horizontal section.

Figure 6(a) shows the calculated water volume in the lower tank after the quasisteady state, which was used to obtain the time-averaged water flow rate through the hot leg. Figure 6(b) compares the calculated CCFL characteristics with (3) for low pressure conditions. The calculated results agreed very well with (3) except for $(J_G^*)^{1/2} = 0.5$, where the falling water flow rate was underestimated. The results showed capability to predict effects of fluid properties on CCFL characteristics and confirmed that CCFL characteristics in the Wallis diagram were mitigated under 1.5 MPa steam-water conditions comparing with air-water flows at 0.1 MPa.

4.2. Standard $k - \epsilon$ Turbulent Model Results for the 1/15-Scale Air-Water Tests. Figure 7 shows results calculated using the standard $k - \epsilon$ turbulent model. Figure 7(a) shows the calculated water volume in the lower tank simulating the upper plenum after establishment of the quasisteady state, which was used to obtain the time-averaged water flow rate through the hot leg. The maximum value of the turbulent viscosity ratio was 10^4 . The results during the initial 5–10 s of the calculation were not used because they included transient effects after the change of calculation conditions. Figure 7(b) compares calculated CCFL characteristics with test data [8]. The falling water flow rates (J_L^*) were greatly underestimated. Even when the maximum value of the turbulent viscosity ratio was reduced to 10^3 , the calculated (J_L^*) did not change.

4.3. Laminar Model Results for the 1/15-Scale Air-Water Tests. As shown in Figure 7(b), the standard $k - \epsilon$ turbulent model greatly underestimated the falling water flow rates (J_L^*). Therefore, the laminar model was used.

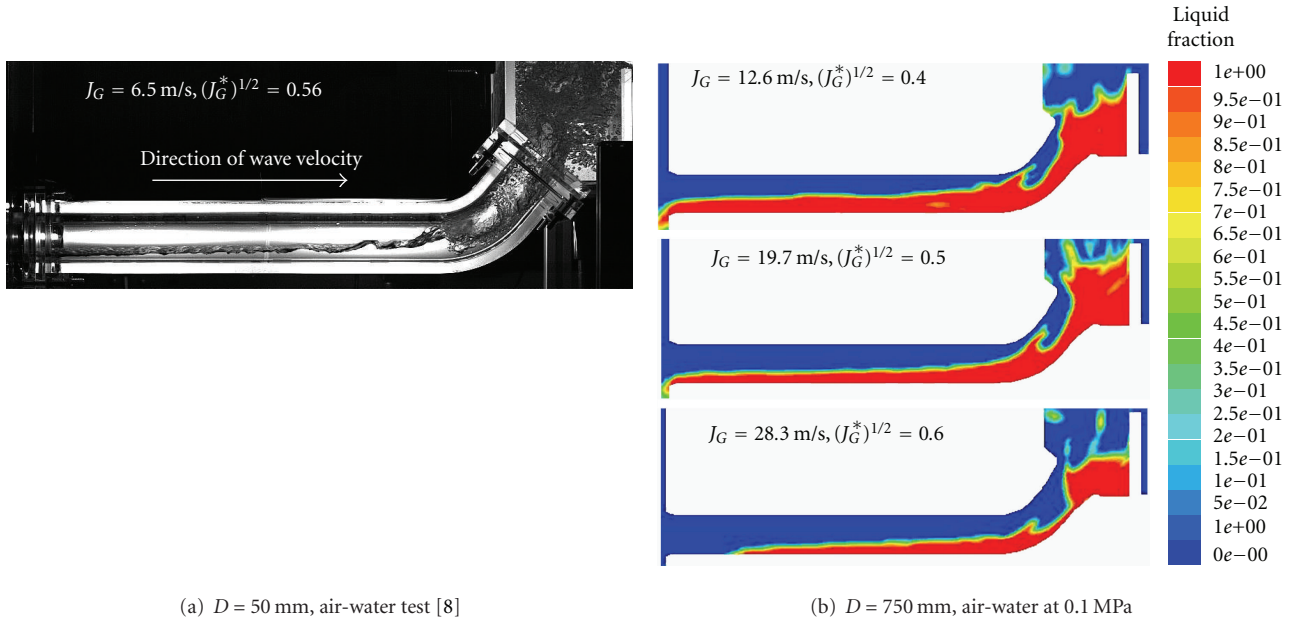


FIGURE 5: Flow patterns.

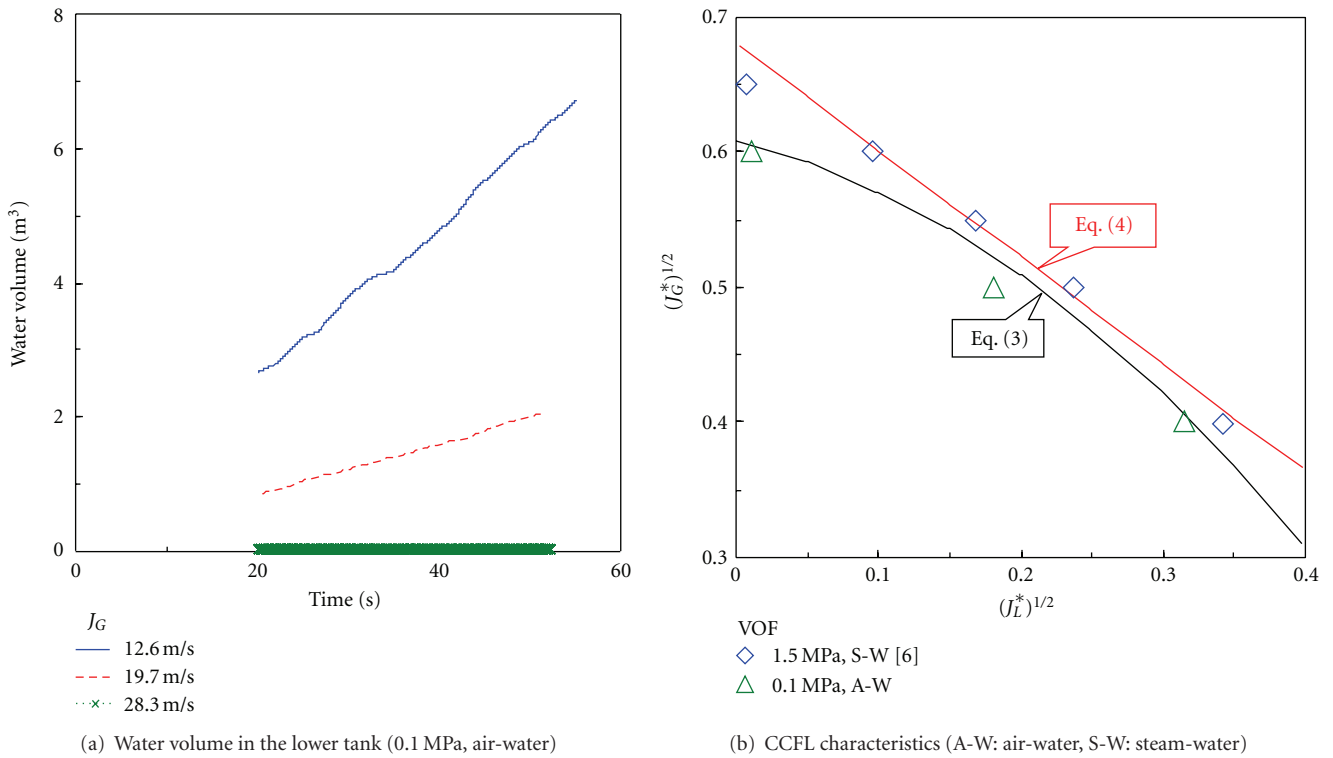
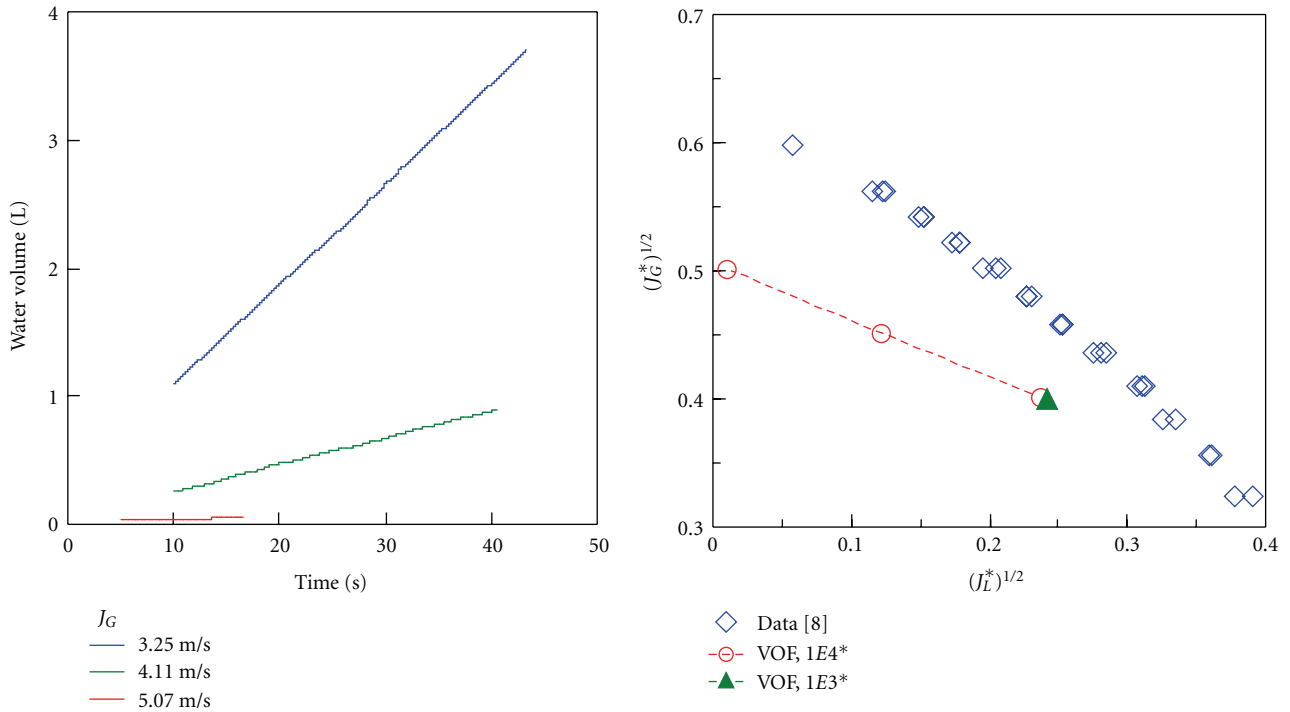


FIGURE 6: Results calculated for the full-scale hot leg.

Figure 8 shows flow patterns calculated by the VOF method. The calculated flow patterns were similar to the observed flow patterns shown in Figure 5(a). Because small waves could not be captured with the rather large calculation cells used, stratified flow formed in the horizontal pipe, but water near the gas-liquid interface flowed toward the elbow.

A large rolling wave periodically appeared near the elbow and the water flow rate was restricted there. The gas-liquid interface in the horizontal pipe fluctuated and it caused fluctuation of the falling water flow rate through the hot leg.

Figure 9 shows results calculated using the laminar model. Figure 9(a) shows the calculated water volume in the



(a) Water volume in the lower tank (maximum turbulent viscosity ratio = 10^4)

(b) CCFL characteristics (*maximum turbulent viscosity ratio)

FIGURE 7: Results calculated using the standard $k - \epsilon$ turbulent model for the 1/5-scale tests ($D = 50$ mm, air-water).

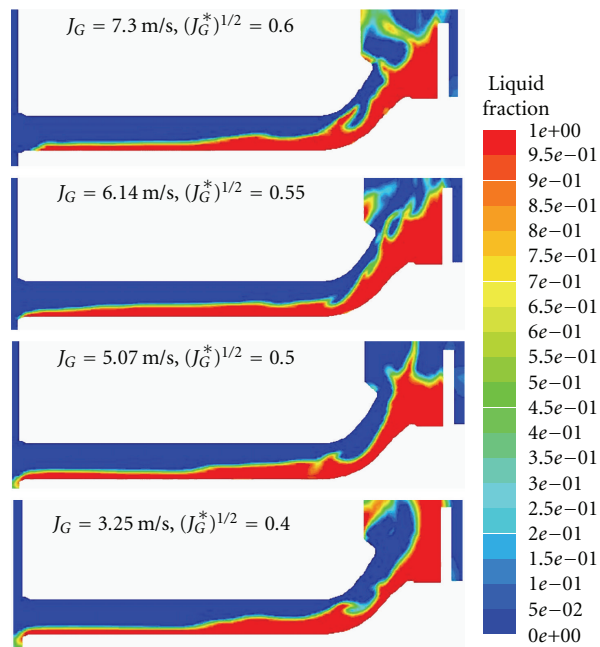


FIGURE 8: Flow patterns for the 1/5-scale tests (laminar model).

lower tank, which fluctuated due to fluctuation of the gas-liquid interface in the horizontal pipe. The results during the initial 10 s of the calculation were not used for CCFL characteristics because they included transient effects after the change of calculation conditions. Figure 9(b) compares

calculated CCFL characteristics with test data [8] and values calculated by the two-fluid model [16]. The falling water flow rates (J_L^*) calculated by the VOF method with the laminar model agreed well with the test data and calculated results of the two-fluid model.

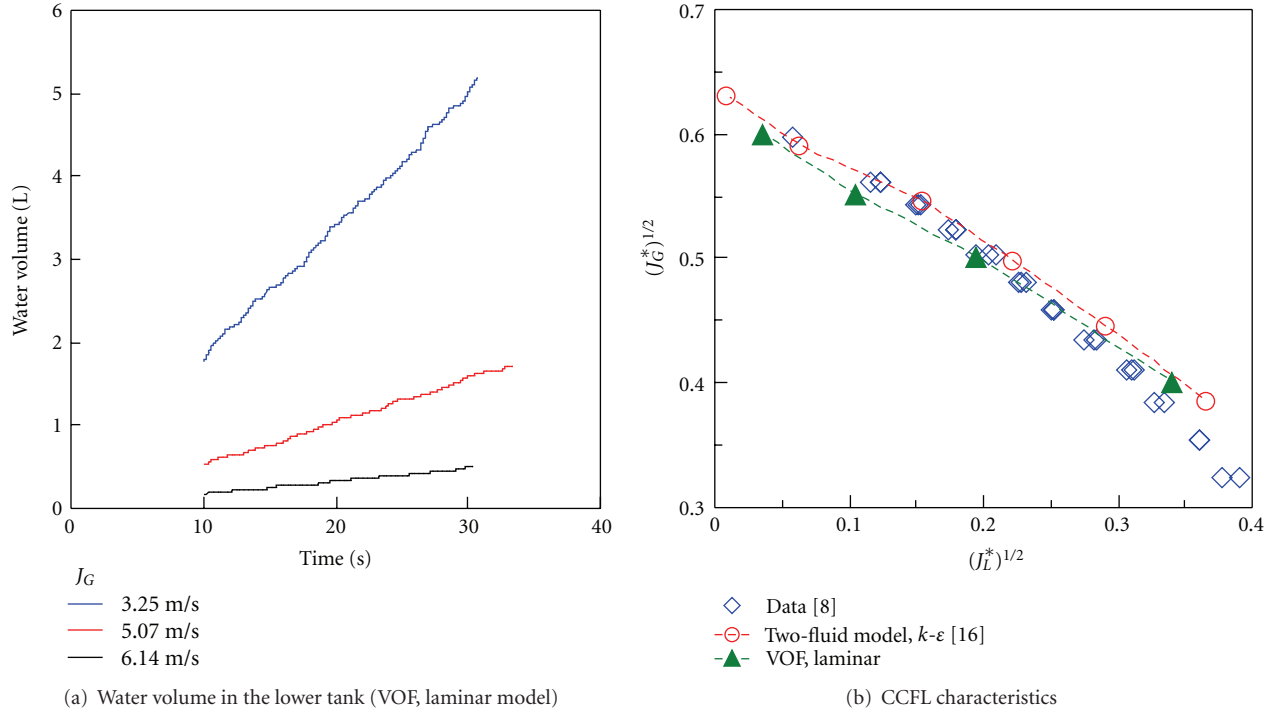


FIGURE 9: Results calculated using the laminar model for the 1/5-scale tests ($D = 50$ mm, air-water).

TABLE 2: Summary of CCFL prediction.

Shape and scale	Size	Two-fluid*	VOF: remarks
1/5 rectangular	$H = 150$ mm	○ (—) [14]	○ (○): $k - \epsilon$ (TVR=10 ⁵) [5]
1/3 rectangular	$H = 250$ mm	○ (Δ) [17]	Δ (○): $k - \epsilon$ (TVR=10 ⁵) [17]
1/15 circular	$D = 50$ mm	⊙ (—) [16]	⊙ (—): laminar [p]
Full scale	$D = 750$ mm	⊙ (×) [4]	⊙ (⊙): $k - \epsilon$ (TVR = 10 ⁴) [p]

* Standard $k - \epsilon$ turbulent model, maximum turbulent viscosity ratio (TVR) = 10⁵,

D : diameter, H : height of rectangular channel,

⊙: very good, ○: good, Δ: poor, ×: very poor, —: not available,

(): effects of fluid properties, []: references, [p]: present study.

4.4. Discussion. The standard $k - \epsilon$ turbulent model gave a good CCFL prediction for full-scale hot leg conditions as shown in Figure 6(b). For 1/15-scale conditions, however, it greatly underestimated the falling water flow rates, and the laminar model gave a better CCFL prediction. Figure 10 shows the calculated Reynolds numbers of gas and liquid phases, which are defined by

$$Re_k = \frac{J_k D}{\nu_k}, \quad (k = G \text{ or } L), \quad (5)$$

where ν (m²/s) is the kinematic viscosity. The gas phase was turbulent in both the full scale and 1/15 scale. The liquid phase was turbulent except at low J_L in the full scale conditions, but it was laminar except at high J_L in the 1/15-scale conditions. This may be related to why the laminar model gave the better CCFL prediction for the 1/15-scale conditions. On the other hand, however, in the two-fluid model, the standard $k - \epsilon$ turbulent model gave a good CCFL prediction for both the 1/15-scale and full-scale conditions as shown in Figure 2(b).

Table 2 summarizes results of the CCFL prediction. The two-fluid model with the standard $k - \epsilon$ turbulent model gave good CCFL prediction for effects of shape and scale [4, 14, 16, 17]. Its prediction was very good for circular channels, but poor or very poor for effects of fluid properties. Under large gas density conditions, it greatly underestimated the falling water flow rates. On the other hand, the VOF method gave good CCFL prediction for effects of fluid properties [5, 17]. However, it was not suitable for circular channels, and the flow model should be changed to get good agreement with CCFL data. Table 2 indicates that suitable calculation models and conditions should be selected to get good agreement with data for each scale.

5. Conclusions

In order to evaluate applicability of the VOF method to different fluid properties and a different scale, we did numerical simulations for full-scale air-water conditions

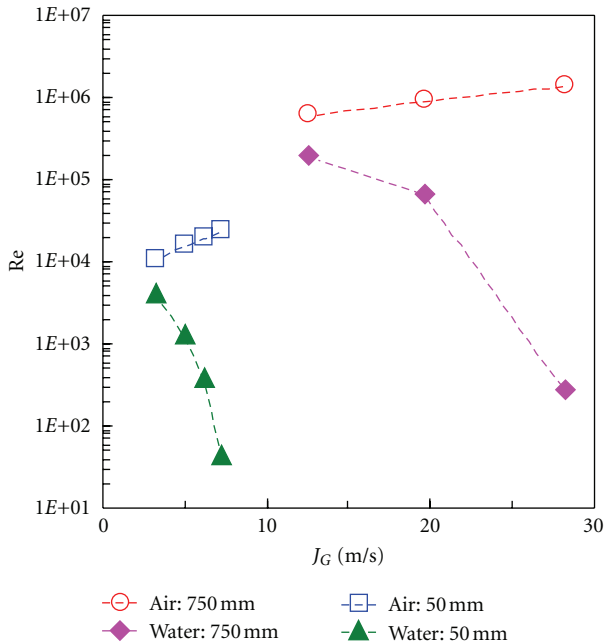


FIGURE 10: Reynolds numbers.

(750 mm diameter) and the 1/15-scale air-water tests (50 mm diameter), respectively.

The results calculated using the standard $k - \epsilon$ turbulent model for full-scale conditions agreed well with CCFL data, and confirmed that CCFL characteristics in the Wallis diagram were mitigated under 1.5 MPa steam-water conditions comparing with air-water flows at 0.1 MPa.

The results calculated using the standard $k - \epsilon$ turbulent model for the 1/15-scale air-water tests greatly underestimated the falling water flow rates. Therefore, a laminar flow model was used, and the calculated results agreed well with the CCFL data. This indicated that suitable calculation models and conditions should be selected to get good agreement with data for each scale.

References

- [1] S. Al Issa and R. Macian, "A review of CCFL phenomenon," *Annals of Nuclear Energy*, vol. 38, no. 9, pp. 1795–1819, 2011.
- [2] G. B. Wallis, *One-Dimensional Two-Phase Flow*, McGraw Hill, New York, NY, USA, 1969.
- [3] C. Vallée, T. Seidel, D. Lucas, A. Tomiyama, and M. Murase, "Comparison of countercurrent flow limitation experiments performed in two different models of the hot leg of a pressurized water reactor with rectangular cross section," *Journal of Engineering for Gas Turbines and Power*, vol. 133, no. 5, article 052917, 2011.
- [4] I. Kinoshita, M. Murase, Y. Utanohara, N. Minami, and A. Tomiyama, "Numerical simulation of countercurrent gas-liquid flow in a PWR hot leg under reflux cooling," *Journal of Nuclear Science and Technology*, vol. 47, no. 10, pp. 963–972, 2010.
- [5] I. Kinoshita, M. Murase, T. Nariai, and A. Tomiyama, "Countercurrent gas-liquid flow in a rectangular channel simulating a PWR hot leg (3) evaluation of effects of fluid properties using VOF method," *Japanese Journal of Multiphase Flow*, vol. 24, no. 4, pp. 445–453, 2010 (Japanese).
- [6] M. Murase, I. Kinoshita, C. Yanagi et al., "Numerical simulation of countercurrent gas-liquid flow in a PWR hot leg using VOF method," in *Proceedings of the 14th International Topical Meeting on Nuclear Reactor Thermal-hydraulics (NURETH14-067'11)*, Toronto, Canada, September 2011.
- [7] F. Mayinger, P. Weiss, and K. Wolfert, "Two-phase flow phenomena in full-scale reactor geometry," *Nuclear Engineering and Design*, vol. 145, no. 1-2, pp. 47–61, 1993.
- [8] N. Minami, D. Nishiwaki, T. Nariai, A. Tomiyama, and M. Murase, "Countercurrent gas-liquid flow in a PWR hot leg under reflux cooling (I) air-water tests for 1/15-scale model of a PWR hot leg," *Journal of Nuclear Science and Technology*, vol. 47, no. 2, pp. 142–148, 2010.
- [9] M. A. Navarro, "Study of countercurrent flow limitation in a horizontal pipe connected to an inclined one," *Nuclear Engineering and Design*, vol. 235, no. 10–12, pp. 1139–1148, 2005.
- [10] H. J. Richter, G. B. Wallis, K. H. Carter, and S. L. Murphy, *Deentrainment and Countercurrent Air-water Flow in a Model PWR Hot-leg*, NRC-0193-9, U. S. Nuclear Regulatory Commission, 1978.
- [11] A. Ohnuki, H. Adachi, and Y. Muraio, "Scale effects on countercurrent gas-liquid flow in a horizontal tube connected to an inclined riser," *Nuclear Engineering and Design*, vol. 107, no. 3, pp. 283–294, 1988.
- [12] G. Geffraye, P. Bazin, P. Pichon, and A. Bengaouer, "CCFL in hot legs and steam generators and its prediction with the CATHARE code," in *Proceedings of the 7th International Topical Meeting on Nuclear Reactor Thermal Hydraulics (NURETH-7'95)*, Saratoga Springs, NY, USA, September 1995.
- [13] M. J. Wang and F. Mayinger, "Simulation and analysis of thermal-hydraulic phenomena in a PWR hot leg related to SBLOCA," *Nuclear Engineering and Design*, vol. 155, no. 3, pp. 643–652, 1995.
- [14] N. Minami, M. Murase, D. Nishiwaki, and A. Tomiyama, "Countercurrent gas-liquid flow in a rectangular channel simulating a PWR hot leg (2) analytical evaluation of countercurrent flow limitation," *Japanese Journal of Multiphase Flow*, vol. 22, no. 4, pp. 413–422, 2008 (Japanese).
- [15] Deendarlianto, T. Höhne, D. Lucas, and C. Vallée, "Numerical simulation of air-water counter-current two-phase flow in a model of the hot-leg of a pressurized water reactor (PWR)," in *Proceedings of the 7th International Conference on Multiphase Flow (ICMF'10)*, Tampa, Fla, USA, May 2010.
- [16] N. Minami, M. Murase, and A. Tomiyama, "Countercurrent gas-liquid flow in a PWR hot leg under reflux cooling (II) numerical simulation of 1/15-scale air-water tests," *Journal of Nuclear Science and Technology*, vol. 47, no. 2, pp. 149–155, 2010.
- [17] Y. Utanohara, I. Kinoshita, M. Murase, D. Lucas, C. Vallée, and A. Tomiyama, "Numerical simulations for steam-water CCFL tests using the 1/3 scale rectangular channel simulating a PWR hot leg," *Nuclear Engineering and Design*. In Press.

Research Article

Countercurrent Air-Water Flow in a Scale-Down Model of a Pressurizer Surge Line

Takashi Futatsugi,¹ Chihiro Yanagi,² Michio Murase,²
Shigeo Hosokawa,¹ and Akio Tomiyama¹

¹ Department of Mechanical Engineering, Faculty of Engineering, Kobe University, 1-1 Rokkodai, Nada, Hyogo Kobe, 657-8501, Japan

² Institute of Nuclear Safety System, Inc. (INSS), 64 Sata, Mihama-cho, Mikata-gun, Fukui 919-1205, Japan

Correspondence should be addressed to Akio Tomiyama, tomiya@mech.kobe-u.ac.jp

Received 13 October 2011; Accepted 16 December 2011

Academic Editor: Thomas Hoehne

Copyright © 2012 Takashi Futatsugi et al. This is an open access article distributed under the Creative Commons Attribution License, which permits unrestricted use, distribution, and reproduction in any medium, provided the original work is properly cited.

Steam generated in a reactor core and water condensed in a pressurizer form a countercurrent flow in a surge line between a hot leg and the pressurizer during reflux cooling. Characteristics of countercurrent flow limitation (CCFL) in a 1/10-scale model of the surge line were measured using air and water at atmospheric pressure and room temperature. The experimental results show that CCFL takes place at three different locations, that is, at the upper junction, in the surge line, and at the lower junction, and its characteristics are governed by the most dominating flow limitation among the three. Effects of inclination angle and elbows of the surge line on CCFL characteristics were also investigated experimentally. The effects of inclination angle on CCFL depend on the flow direction, that is, the effect is large for the nearly horizontal flow and small for the vertical flow at the upper junction. The presence of elbows increases the flow limitation in the surge line, whereas the flow limitations at the upper and lower junctions do not depend on the presence of elbows.

1. Introduction

The mid-loop operation is to be conducted during plant refueling and maintenance of a PWR (Pressurized Water Reactor). In this operation, the reactor coolant level is kept around the primary loop center, and decay heat is removed by RHR (Residual Heat Removal) systems. If the loss of cooling systems such as RHR and/or other cooling systems takes place, cooling water in the reactor core may be heated up to boil and the top of the fuel assembly can be exposed to the air. In such an event, reflux cooling by the steam generators (SG) is regarded as one of the possible and effective core cooling methods. The reflux cooling is a way of core cooling by making use of water condensed in SGs. The steam generated in the reactor core and water condensed in the SG form a countercurrent flow in the hot leg. The authors therefore measured CCFL (Countercurrent Flow Limitation) characteristics in a scale-down model of a hot leg using air and water [1] and reported that CCFL can be accurately

evaluated based on a one dimensional momentum balance for air-water two-phase flow [2]. In addition to this CCFL, the steam generated in the reactor core and water condensed in the pressurizer due to heat transfer to the vessel wall may also form a countercurrent flow in a surge line which connects the hot leg and the pressurizer. The ROSA-IV/LSTF (Rig-of-Safety-Assessment No. 4/Large Scale Test Facility) experiment [3], which simulated the loss of RHR systems during mid-loop operation, reported that water actually accumulated in the pressurizer due to CCFL in the surge line. When the core coolant moves to the primary coolant system and remains there, the reactor core water level decreases. Thus, characteristics of CCFL in the surge line must be well understood for safety evaluation of the mid-loop operation.

Takeuchi et al. [4] calculated CCFL characteristics for a slightly inclined surge line of an AP600 using the momentum equations for steam and water. They reported that (1) CCFL in a vertical pipe is more dominant than that in a slightly inclined pipe, (2) the horizontal elbow increases

the falling water volume, and (3) CCFL in the vertical pipe is the most dominant among various CCFLs taking place at different locations in the surge line. Although their prediction overestimated the falling water volume compared with the small break LOCA (Loss of Coolant Accident) data conducted at the AP600-scale test facility (APEX) [5, 6], there are no experimental data for validating their predictions. The surge line consists of a vertical pipe, a vertical elbow and an inclined pipe with several elbows. The flow in the surge line is very complicated due to its complex geometry, and therefore, it is difficult to apply the data and knowledge of CCFL obtained in a simple geometry such as straight pipes and ducts to CCFL in the surge line.

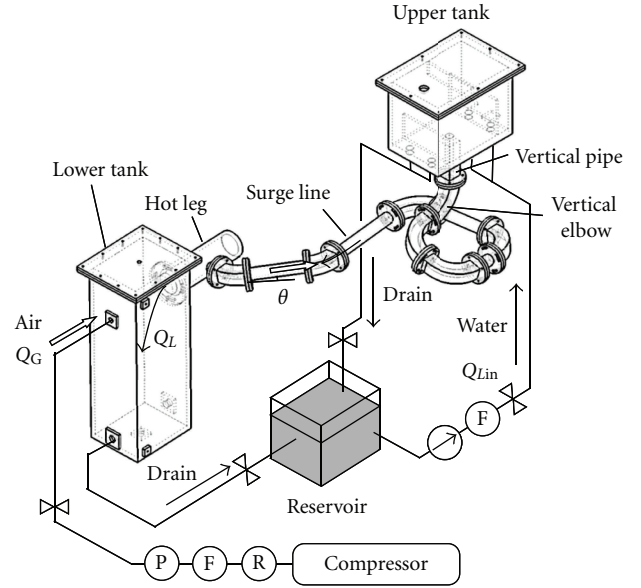
In this study, we carried out experiments using air and water in a 1/10-scale model and measured CCFL characteristics in the surge line. Effects of inclination angle and elbows in the surge line on CCFL characteristics were also investigated.

2. Experimental Setup

Figure 1 shows the experimental setup. It consists of the lower tank corresponding to a reactor vessel, the surge line, the upper tank simulating a pressurizer, and the air and water supply systems. The surge line is made of acrylic resin for the observation of flow pattern in the pipe. The internal diameter is 30 mm. The geometry of the surge line is shown in Figure 2. Air is supplied through the sidewall of the lower tank. Water is supplied through the bottom face of the upper tank. They form a countercurrent flow in the surge line. The elbow is made of two acrylic blocks with semicircular grooves to keep the channel cross-section circle. At a constant flow rate Q_{Lin} of water supplied to the upper tank, the flow rate Q_L of water falling into the lower tank was measured at each gas flow rate Q_G to obtain a relationship between Q_L and Q_G . The Q_L was measured not only by increasing Q_G but also by decreasing Q_G to check a possibility of hysteresis in CCFL. The experimental ranges were $J_{Lin} (= 4Q_{Lin}/\pi D^2) = 0.02\text{--}0.12\text{ m/s}$ and $J_G (= 4Q_G/\pi D^2) = 0\text{--}5.5\text{ m/s}$. CCFL data were plotted by using the dimensionless gas and liquid volumetric fluxes, J_G^* and J_L^* , given by [6]

$$J_k^* = J_k \left\{ \frac{\rho_k}{gD(\rho_L - \rho_G)} \right\}^{1/2}, \quad (k = G, L), \quad (1)$$

where J is the superficial velocity, ρ the density, g the acceleration of gravity, and D the pipe diameter. The subscripts G and L denote the gas and liquid phases, respectively. The inclination angle θ of the surge line was changed from 0.0 to 5.0 deg. (0.0, 0.6, 1.0, 2.0 and 5.0 deg.) to investigate the effects of θ on CCFL characteristics. We also measured CCFL characteristics by replacing the surge line with the straight pipe shown in Figure 3 to examine effects of elbows.



(F: flow meter, P: pressure gauge, R: regulator)

FIGURE 1: Experimental setup (Surge line).

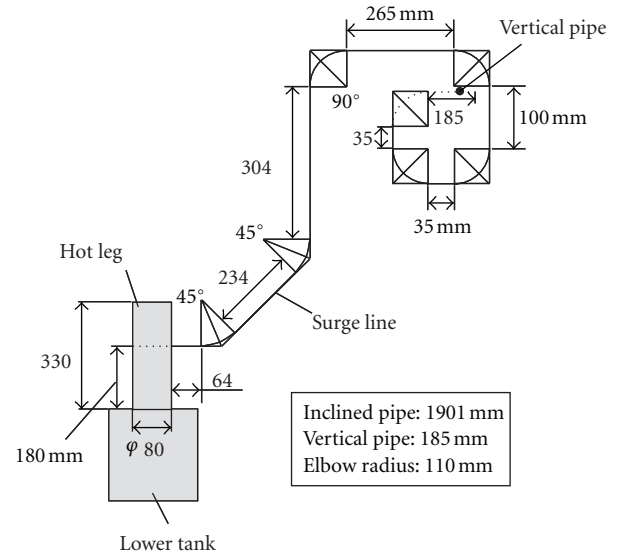


FIGURE 2: Geometry of surge line.

3. Results and Discussion

3.1. Classification of CCFL. Depending on the inclination angle θ and J_G , CCFL took place at three different locations, that is, at the upper junction, in the surge line, and at the lower junction as shown in Figure 4. Hereafter, CCFL at the upper junction between the surge line and the upper tank, in the surge line and that at the lower junction between the surge line and the hot leg will be referred to as CCFL-U, CCFL-S, and CCFL-L, respectively.

In CCFL-U, the flow limitation occurs only at the upper junction of the surge line as shown in Figure 5(a), and

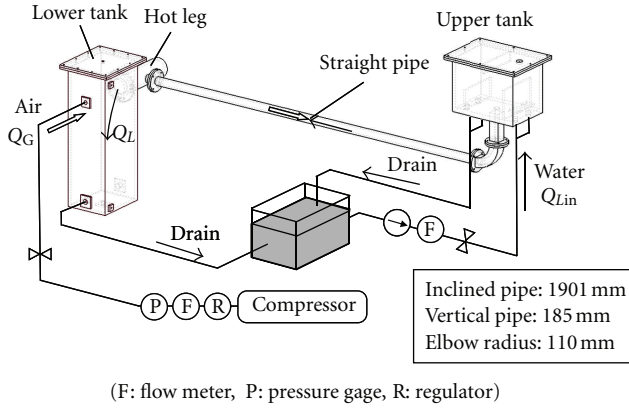


FIGURE 3: Experimental apparatus with straight pipe.

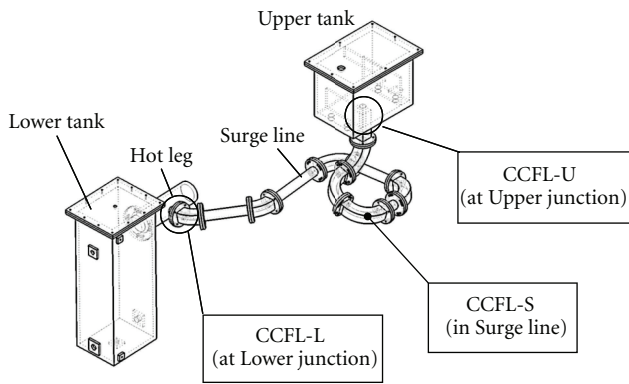


FIGURE 4: Flow limitation locations and CCFL classification.

therefore, water in the surge line and at the lower junction smoothly flows toward the lower tank. To the contrary, the flow limitation occurs not only at the upper junction but also in the surge line in CCFL-S as shown in Figure 5(b). Waves are generated in the surge line and move toward the upper junction. In CCFL-L, the flow limitation occurs at the lower junction as well as at the upper junction. Water is accumulated near the lower junction to form large liquid slugs and periodically flows back toward the upper junction as shown in Figure 5(c).

3.2. CCFL Characteristics at Reference Condition. Figure 6 shows CCFL characteristics at $J_{Lin} = 0.07 \text{ m/s}$ and $\theta = 0.6 \text{ deg.}$ As J_G^* increases from zero, flow limitation takes place when J_G^* reaches a certain critical value (point A in Figure 6). At point A, waves form in the surge line and move toward the upper junction. At the same time, J_L^* suddenly decreases to the flooding point (point B in Figure 6), that is, CCFL-S occurs. Further increase in J_G^* reduces J_L^* , and all the water returns to the upper tank at the flow reversal point (point C in Figure 6). When J_G^* is decreased from the flow reversal point C, J_L^* gradually increases as shown in Figure 6. The minimum J_G^* observed in the decreasing process is smaller than J_G^* at the flooding point B. Thus, hysteresis exists in the CCFL characteristics. The hysteresis is caused by the difference in the presence of initial waves on the

gas-liquid interface. There is, however, no difference in the dependence of J_L^* on J_G^* between the processes of increasing and decreasing J_G^* .

3.3. Effects of θ . Figure 7 shows CCFL characteristics at various θ . At $\theta = 0.0$ and 0.6 deg. , only CCFL-S takes place at any values of J_G . At $\theta = 1.0 \text{ deg.}$, CCFL disappears in the surge line, and therefore, it is classified as CCFL-U when J_G is low, whereas CCFL-S occurs at high J_G . This disappearance of CCFL in the surge line is due to the enhancement of water drainage by increasing θ . At $\theta = 2.0$ and 5.0 deg. , CCFL-L appears instead of CCFL-S at high J_G . This indicates that the flow limitation at the lower junction becomes dominant because CCFL in the surge line is mitigated by the increase in θ . At low J_G , CCFL-U occurs not only for $\theta = 2.0$ and 5.0 deg. but also for $\theta = 1.0 \text{ deg.}$ These results show that type of CCFL depends on θ and J_G^* , and the dependence of the relation between J_G^* and J_L^* on θ is different among CCFL-S, CCFL-U, and CCFL-L.

Figure 8 shows characteristics of CCFL-S at various θ . A small change in θ causes a large change in the falling water flow rate, that is, the dependence of CCFL-S on the inclination angle is very large. The increase in θ results in the mitigation of flow limitation in the surge line due to the enhancement of water drainage. Hence, CCFL-S occurs only at low θ .

Figure 9 shows characteristics of CCFL-L at various θ . CCFL-L is also affected by θ , and the flow limitation becomes weaker as θ increases. The dependence of CCFL-L on the inclination angle, however, is weaker than that of CCFL-S. Since the holdup at the lower junction depends not only on the water velocity along the surge line but also on the velocity of water falling into the lower tank, the weak dependency of the falling water velocity on θ might be a cause of the small dependency of CCFL-L on θ .

Figure 10 shows characteristics of CCFL-U at various θ . CCFL-U is the limitation at the upper junction between the upper tank and the vertical pipe, and the gravity force acting on the water along the surge line (the vertical pipe) is $\rho g \cos \theta$. Hence, CCFL-U has a very weak dependence on θ at small θ as shown in Figure 10.

These experimental results confirm that the effect of θ on CCFL depends on the flow direction, that is, the effect is large for the nearly horizontal flow in the surge line, small for the vertical flow at the upper junction, and intermediate for the flow at the lower junction at which the flow changes its direction from horizontal to vertical directions. The CCFL in the surge line is determined by the most strong flow limitation among CCFL-S, CCFL-U and CCFL-L.

3.4. Onset of Flooding. The gas volumetric flux at the onset of flooding is important information when designing surge lines. Figure 11 shows the onset of flooding measured by increasing the gas volumetric flux. Flooding-S, Flooding-U, and Flooding-L in Figure 11 represent that the flooding takes place in the surge line, at the upper junction and at the lower

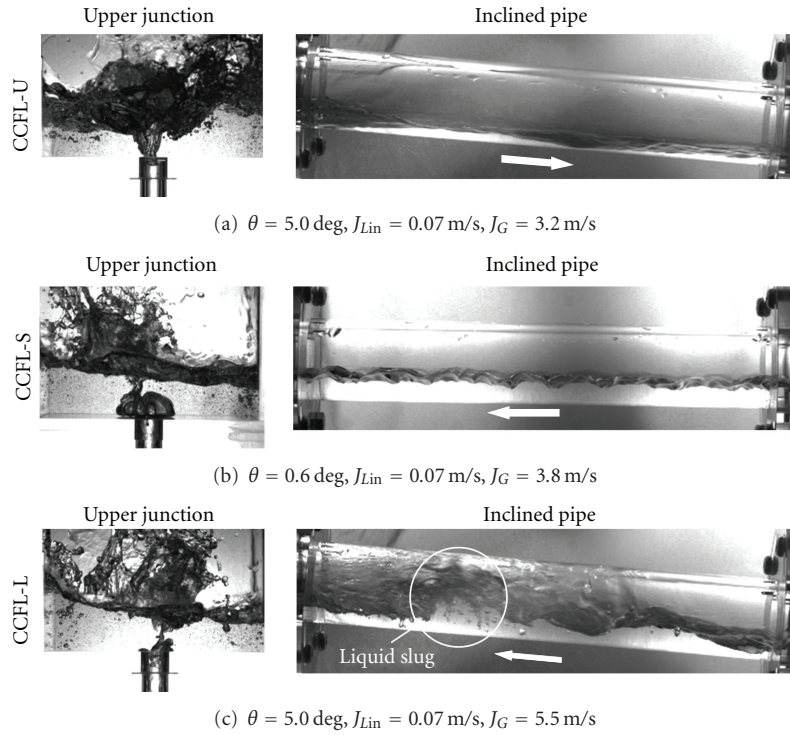


FIGURE 5: Typical flow pattern at CCFL conditions.

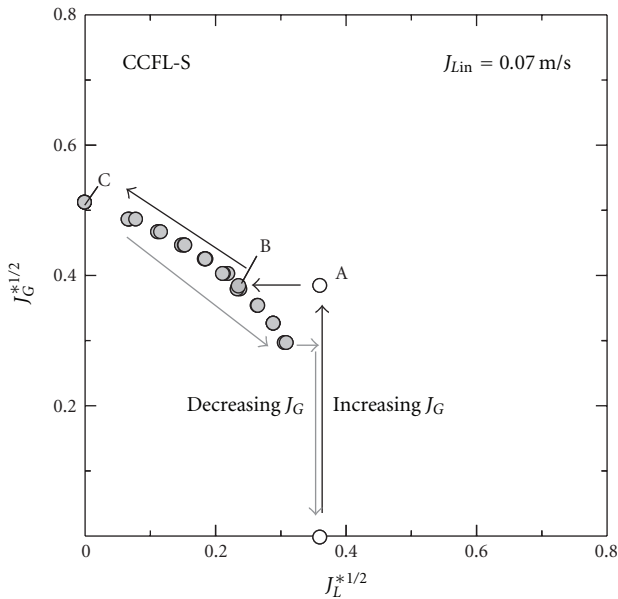


FIGURE 6: CCFL characteristics ($\theta = 0.6$ deg.).

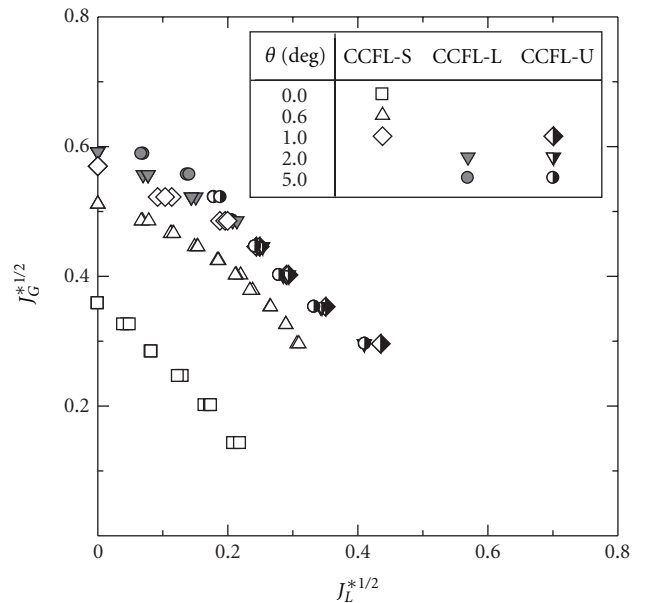


FIGURE 7: CCFL characteristics (effects of θ).

junction, respectively. The line in Figure 11 is drawn by using the Wallis's model [7–9]:

$$\sqrt{J_G^*} + \sqrt{J_{Lin}^*} = 1. \quad (2)$$

The J_G^* at the onset of flooding decreases as J_{Lin}^* increases, and J_G^* increases with θ . The flooding always occurs in the surge line at low θ . On the other hand, at high θ , it occurs at the

lower junction when J_{Lin}^* is low and at the upper junction at high J_{Lin}^* . Since the flooding at the upper junction is similar to that in a vertical pipe, the points of Flooding-U are not far from (2).

3.5. Effects of J_{Lin} . Figure 12 shows the CCFL characteristics under three different J_{Lin} conditions ($J_{Lin} = 0.02, 0.07,$ and

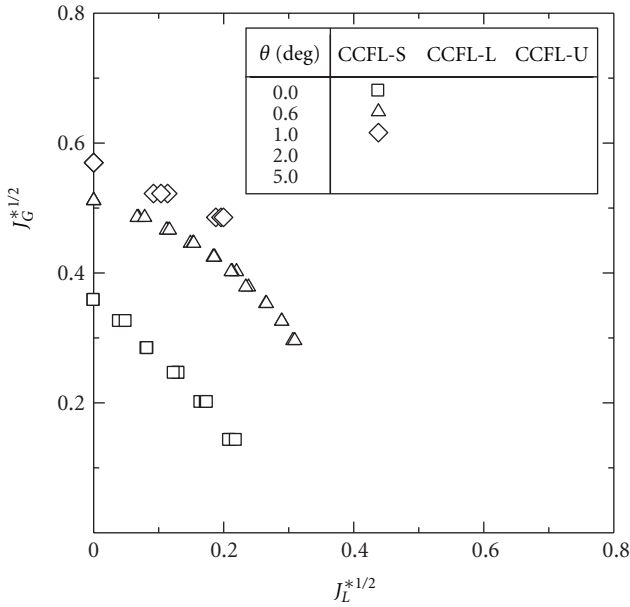


FIGURE 8: CCFL-S characteristics (effects of θ).

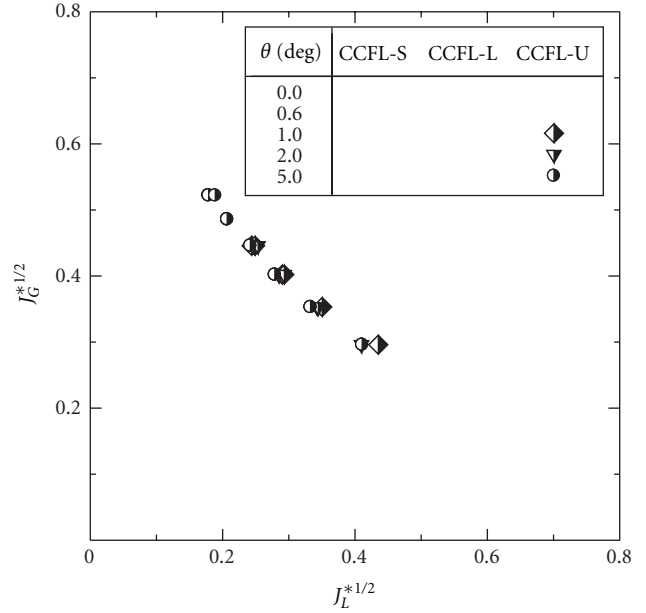


FIGURE 10: CCFL-U characteristics (effects of θ).

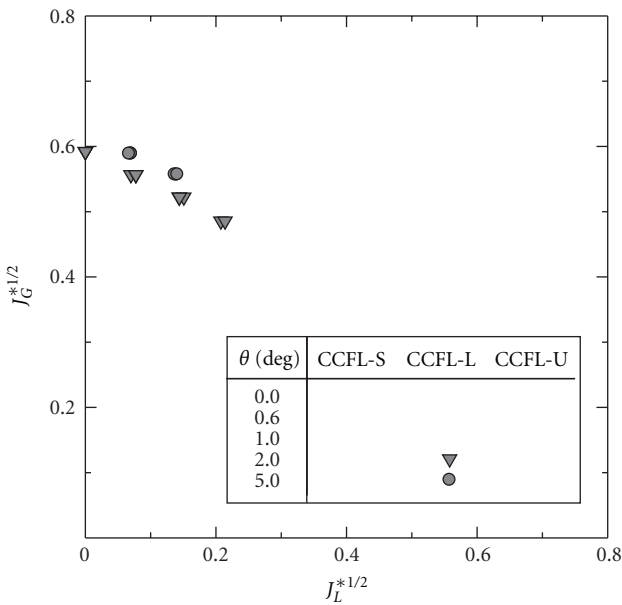


FIGURE 9: CCFL-L characteristics (effects of θ).

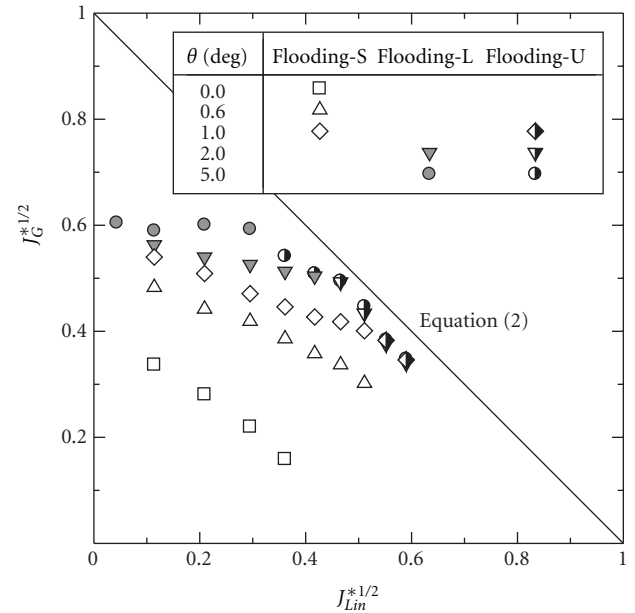


FIGURE 11: Onset of flooding.

0.12 m/s) for $\theta = 0.6$ and 5.0 deg. The volumetric flux J_L^* of the falling water does not depend on the volumetric flux J_{Lin} of the supplied water in the upper tank, irrespective of θ and a type of CCFL (CCFL-S, CCFL-U, and CCFL-L). This is because the water level in the upper tank depends not on J_{Lin} but on the height of the partition in the upper tank when the flow limitation takes place.

3.6. Effects of Elbows. Figure 13 shows comparisons of CCFL characteristics between the surge line and the straight pipe. CCFL in the straight pipe is also classified into CCFL-S,

CCFL-U, and CCFL-S. CCFL-S occurs at low θ whereas CCFL-U, and CCFL-L appear at high θ . The flow limitation in the surge line is stronger than that in the straight pipe as shown in Figure 13(a). The elbows, therefore, enhance the flow limitation in the surge line, which contradicts the predictions obtained by Takeuchi et al. [4]. They explained that centrifugal force in the elbow section stabilizes the gas-liquid interface and inhibits the flow limitation. However, the centrifugal force would make the liquid film thinner and increase the wall friction. In addition, the presence of elbows would increase pressure drop in the line, in other words,

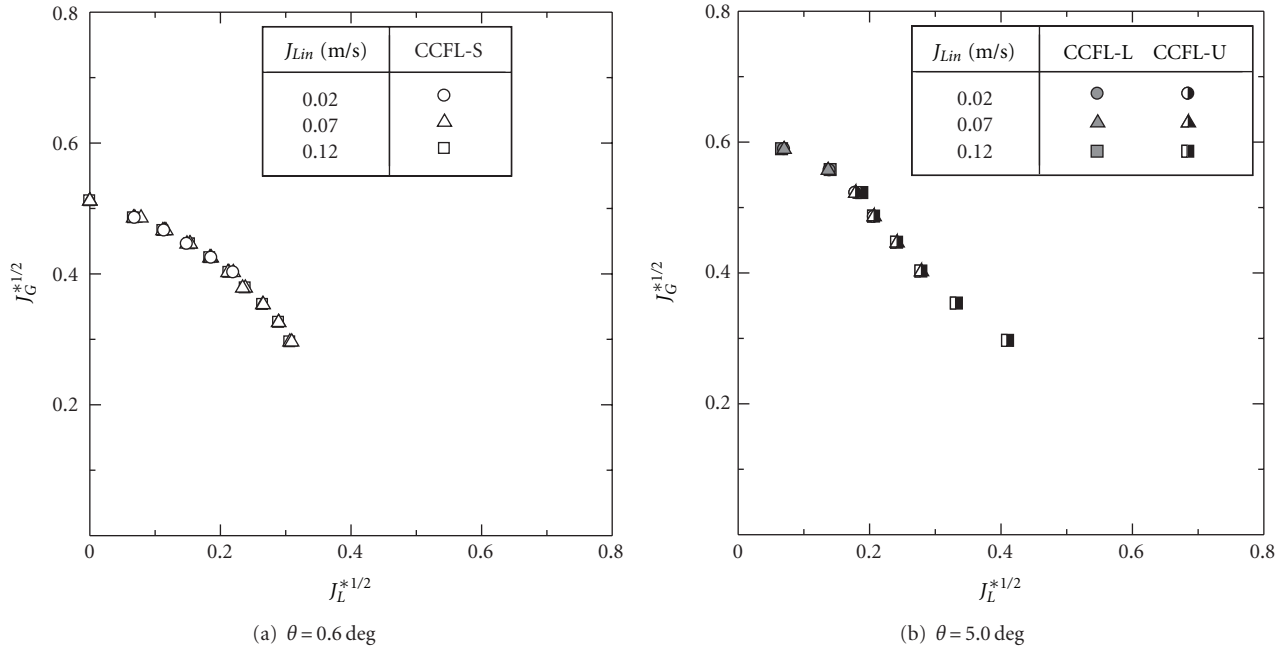
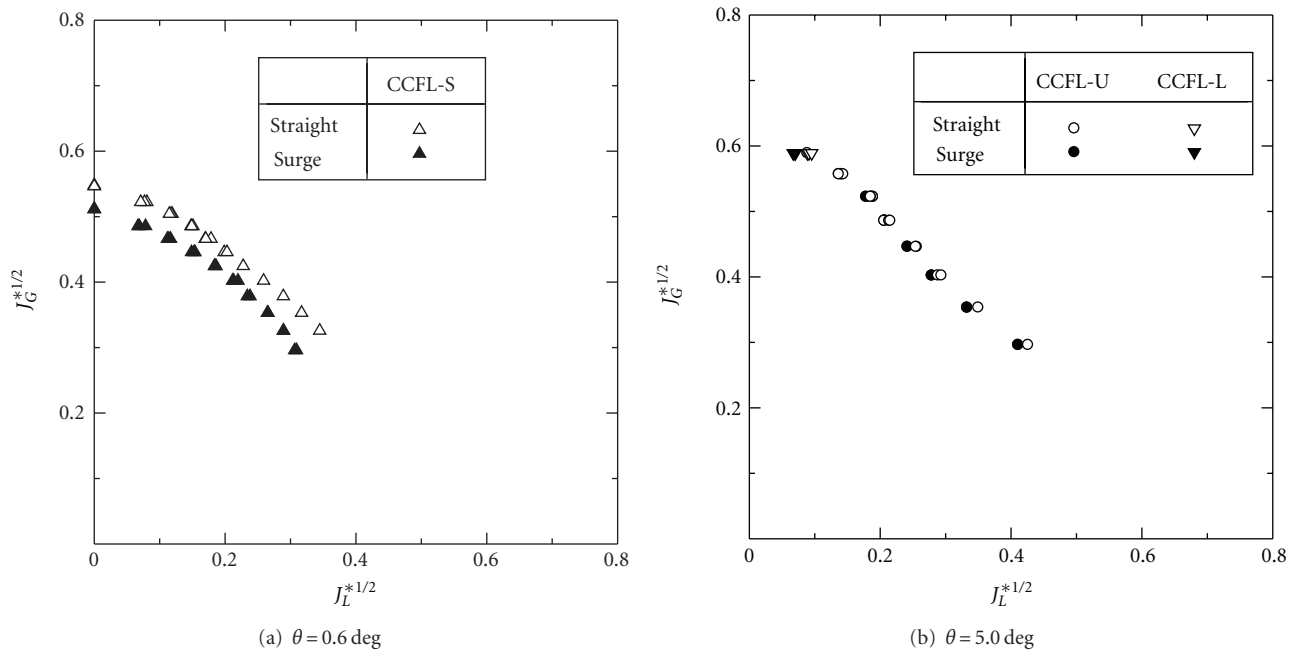
FIGURE 12: CCFL characteristics (effects of J_{Lin}).

FIGURE 13: Effect of elbows on CCFL characteristics.

increases the force acting on water in the upstream direction. These effects would result in enhancement of flow limitation. The present result, therefore, supports the latter speculation rather than Takeuchi's one. On the other hand, CCFL-U and CCFL-L do not depend on the presence of elbows as shown in Figure 13(b). This is because the flow limitation occurs at the junctions, and therefore, it has no relation with the elbows in the surge line.

3.7. Discussion on Effects of Size and Fluid Properties on CCFL Characteristics. Minami et al. [10] measured CCFL characteristics in a scale-down model of PWR hot leg and confirmed thorough comparisons with literature [11–14] that the effects of the size and fluid properties are small. Since CCFL-L and CCFL-S in the surge line are similar to CCFL in the hot leg, this result implies that their dependence on the size and fluid properties is also small. On the other

hand, CCFL-U is similar to CCFL in a vertical pipe. Many researches, which are summarized in textbooks [7, 15, 16], have been carried out for CCFL in a vertical pipe. These researches indicate that the Kutateladze number is more appropriate than the dimensionless volumetric flux J_k^* for large diameter tubes, and that the fluid properties can be taken into account by using the Bond number, viscosity ratio and/or Grashof number. This kind of knowledge can be utilized when applying the present results to a system with different pipe sizes or different fluid properties.

4. Conclusions

Countercurrent air-water flow in a scale-down model of a PWR pressurizer surge line was measured to understand characteristics of countercurrent flow limitation, CCFL. As a result, the following conclusions were obtained.

- (1) CCFL takes place at three different locations, that is, at the upper junction, in the surge line, and at the lower junction. CCFL characteristics are governed by the most dominating flow limitation among the three.
- (2) CCFL characteristics depend on the inclination angle of the surge line and the air flow rate. The effects of inclination angle on CCFL depend on the flow direction, that is, the effect is large for the nearly horizontal flow in the surge line, small for the vertical flow at the upper junction, and intermediate for the flow at the lower junction at which the flow changes its direction from horizontal to vertical directions.
- (3) The presence of elbows enhances the flow limitation in the surge line, whereas the flow limitations at the upper and lower junctions do not depend on the presence of elbows.

Nomenclature

D : Pipe diameter [m]
 g : Acceleration of gravity [m/s^2]
 J : Volumetric flux [m/s]
 J^* : Dimensionless volumetric flux
 Q : Volume flow rate [m^3/s]
 ρ : Density [kg/m^3]
 θ : Angle of inclination [deg.].

Subscripts

G : Gas phase
 L : Liquid phase
 Lin : Liquid phase supplied to the upper tank.

References

- [1] N. Minami, D. Kataoka, A. Tomiyama, S. Hosokawa, and M. Murase, "Countercurrent gas-liquid flow in a rectangular channel simulating a PWR hot leg (1) flow pattern and CCFL characteristics," *Japanese Journal of Multiphase Flow*, vol. 22, no. 4, pp. 403–412, 2008 (Japanese).
- [2] N. Minami, M. Murase, D. Nishiwaki, and A. Tomiyama, "Countercurrent gas-liquid flow in a rectangular channel simulating a PWR hot leg (2) analytical evaluation of countercurrent flow limitation," *Japanese Journal of Multiphase Flow*, vol. 22, no. 4, pp. 413–422, 2008 (Japanese).
- [3] H. Nakamura, J. Katayama, and Y. Kukita, "Loss of residual heat removal (RHR) event during PWR mid-loop operation: ROSA-IV/LSTF experiment without opening on primary loop pressure boundary," *American Society of Mechanical Engineers, Fluids Engineering Division (Publication) FED*, vol. 140, pp. 9–16, 1992.
- [4] K. Takeuchi, M. Y. Young, and A. F. Gagnon, "Flooding in the pressurizer surge line of AP600 plant and analyses of APEX data," *Nuclear Engineering and Design*, vol. 192, no. 1, pp. 45–58, 1999.
- [5] L. E. Hochreiter, S. V. Fanto, L. E. Conway, and L. K. Lau, "Integral testing of the AP600 passive emergency core cooling systems," *Journal of Power and Energy*, vol. 207, no. 4, pp. 259–268, 1993.
- [6] J. N. Reyes, "Scaling Analysis for the OSU AP600 Integral Systems and Long Term Cooling Facility," OSU-NE-9204, 1992.
- [7] G. B. Wallis, *One Dimensional Two-Phase Flow*, McGraw Hill, New York, NY, USA, 1969.
- [8] S. Levy, *Two-Phase Flow in Complex Systems*, Wiley Interscience, 1999.
- [9] G. F. Hewitt and G. B. Wallis, *ASME Multi-Phase Flow Symposium*, ASME, Philadelphia, Pa, USA, 1963.
- [10] N. Minami, D. Nishiwaki, T. Nariai, A. Tomiyama, and M. Murase, "Countercurrent gas-liquid flow in a PWR hot leg under reflux cooling (I) air-water tests for 1/15-scale model of a PWR hot leg," *Journal of Nuclear Science and Technology*, vol. 47, no. 2, pp. 142–148, 2010.
- [11] H. J. Richter, G. B. Wallis, K. H. Carter et al., "Deentrainment and Countercurrent Air-Water Flow in a Model PWR Hot-Leg," NRC-0193-9, U.S. Nuclear Regulatory Commission, 1978.
- [12] A. Ohnuki, "Experimental study of counter-current two-phase flow in horizontal tube connected to an inclined riser," *Journal of Nuclear Science and Technology*, vol. 23, no. 3, pp. 219–232, 1986.
- [13] A. Ohnuki, H. Adachi, and Y. Murao, "Scale effects on countercurrent gas-liquid flow in a horizontal tube connected to an inclined riser," *Nuclear Engineering and Design*, vol. 107, no. 3, pp. 283–294, 1988.
- [14] F. Mayinger, P. Weiss, and K. Wolfert, "Two-phase flow phenomena in full-scale reactor geometry," *Nuclear Engineering and Design*, vol. 145, no. 1-2, pp. 47–61, 1993.
- [15] P. B. Whalley, *Boiling Condensation and Gas-Liquid Flow*, Oxford University Press, New York, NY, USA, 1987.
- [16] J. M. Delhay, M. Giot, and M. L. Riethmuller, *Thermohydraulics of Two-Phase Systems for Industrial Design and Nuclear Engineering*, Hemisphere, New York, NY, USA, 1981.

Research Article

Assessment of TRACE CCFL Model with SBLOCA Experiment of IIST Facility

Jung-Hua Yang,¹ Jong-Rong Wang,² Hao-Tzu Lin,² and Chunkuan Shih³

¹Department of Engineering and System Science, National Tsing Hua University, No. 101, Section 2, Kuang Fu Road, Hsinchu 30013, Taiwan

²Institute of Nuclear Energy Research, Atomic Energy Council, R.O.C., No. 1000, Wenhua Road, Jiaan Village, Longtan Township, Taoyuan 32546, Taiwan

³Institute of Nuclear Engineering and Science, National Tsing Hua University, No. 101, Section 2, Kuang Fu Road, Hsinchu 30013, Taiwan

Correspondence should be addressed to Jung-Hua Yang, junghua1984@gmail.com

Received 15 October 2011; Accepted 26 December 2011

Academic Editor: Thomas Hoehne

Copyright © 2012 Jung-Hua Yang et al. This is an open access article distributed under the Creative Commons Attribution License, which permits unrestricted use, distribution, and reproduction in any medium, provided the original work is properly cited.

In this paper, the TRACE model for IIST facility is developed and verified with the Small Break loss of coolant accident (SBLOCA) experiment of IIST (Institute of Nuclear Energy Research Integral System Test) facility. By using the Wallis and Kutateladze correlations of countercurrent flow limitation (CCFL) model, the TRACE analyses results, such as break flow rate, primary pressure, and the temperature of cold-leg and hot-leg, are consistent with the IIST data. The results show the Kutateladze correlation of CCFL model can well predict the SBLOCA behavior and present good agreement with IIST experiment data in this paper. Besides, the sensitivity study results of Kutateladze correlation in CCFL model are verified and compared with the IIST data.

1. Introduction

A reduced-height and reduced-pressure IIST facility has been established for safety studies of the Westinghouse three loops pressurized water reactor (PWR) since 1992. The research purposes of the IIST facility are enhancement of understanding of thermal hydraulics phenomena during the accidents [1–3], contributing to evaluate and develop the safety computer codes [4, 5], and validation of EOP during the accidents of PWR [6]. The IIST facility has three loops as well as all the systems associated with Westinghouse PWR plant system transients. The maximum operating pressure of the IIST facility is 2.1 MPa. CCFL is an important phenomenon in a reactor system. In a PWR, countercurrent flow (CCF) may occur in both the hot-leg and the entrance to the steam generator during LOCA. CCF also occurs during blowdown as the Emergency Core Cooling Systems (ECCSs) fill water into the downcomer. When the CCFL occurs, the mass and heat transfer between gas and liquid phases reduces, and a water pool forms. This phenomenon

prevents the core from cooling such that the fuel temperature rapidly increases [7]. Therefore, studies on CCF and CCFL are essential for proper nuclear reactor safety.

The codes used in this paper are TRACE v 5.0p2 and SNAP v 2.0.3. TRACE (TRAC/RELAP Advanced Computational Engine) is an advanced and best estimate reactor systems code for analyzing thermal hydraulic behaviors in light water reactors [8]. TRACE consolidates the capabilities of the four codes, TRAC-P, TRAC-B, RELAP 5, and RAMONA, into one modernized code. One of the features of TRACE is its capability to model the reactor vessel with 3D geometry. It can support a more accurate and detailed safety analysis of nuclear power plants. TRACE has a greater simulation capability for loss of coolant accident. Furthermore, a graphic user interface program, SNAP (Symbolic Nuclear Analysis Package), which is being under development by Applied Programming Technology, Inc. for conveniently creating and editing the input decks.

According to the best LOCA simulation capability of TRACE, this paper focuses on the development of TRACE

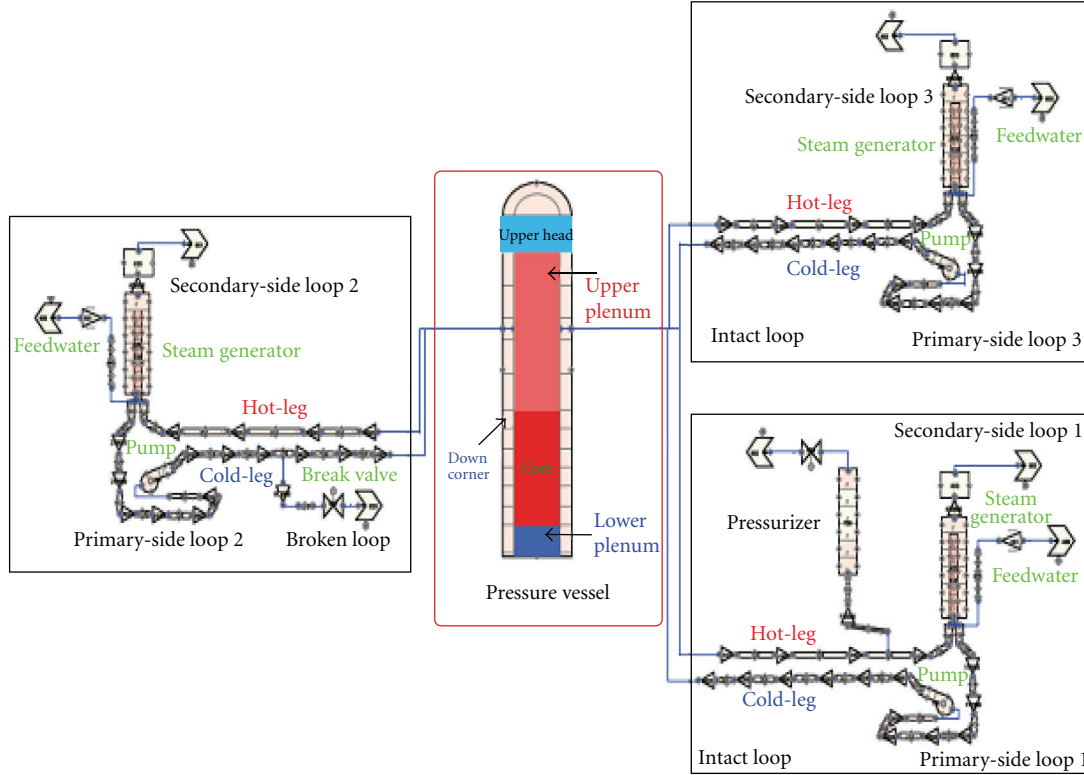


FIGURE 1: The TRACE model for IIST facility.

IIST model and analysis of the SBLOCA with the IIST experiment data. The results of different form of CCFL model, such as Wallis correlation and Kutateladze correlation, are also verified with the IIST data in this study. Furthermore, the sensitivity studies of CCFL model in water level and core cladding temperature are discussed.

2. IIST Facility and SBLOCA Experiment

Figure 1 shows the TRACE model of IIST facility. IIST facility is established in order to simulate the thermal hydraulics phenomena of Maanshan NPP, which is a Westinghouse three loops PWR. The IIST facility consists of a pressure vessel and three loops. Each loop has a steam generator (SG) and a coolant pump [9]. Except that there is a pressurizer in the loop 1, the three loops are identical. The scaling factors of height and volume in the RCS are approximately 1/4 and 1/400, respectively. Scaled safety injection systems (include HPI and accumulators) inject cooling water into the cold-leg of each loop. During the SBLOCA experiment [10], a catch tank is simulated to collect and measure the effluent from the simulated break. The comparison of major parameters between IIST facility and the Maanshan NPP is shown in Table 1.

The experiment of IIST facility was performed in order to simulate a 2% cold-leg break (the break area is 2% of the scaled cold-leg cross-section area) with total HPI failure [11]. This break is located in loop 2 of IIST facility, which is one of the two loops that do not have a pressurizer. In this experiment, the core power decay and pump coastdown

during the SBLOCA experiment were not simulated. The initial condition of the experiment is shown in Table 2.

3. CCFL Model in TRACE

CCFL is an important issue related to the safety analysis of PWRs. CCFL phenomenon determines the maximum velocity of one phase relative to the other one when the velocity of neither of the two phases can increase further without flow regime change [12]. CCFL may occur in the downcomer, the upper core tie plate, the hot legs, the entrance of the SG inlet plenum, and the pressurizer surge line, where the flow direction or flow area changes. The TRACE code has the ability to calculate the CCF and predict the CCFL by applying the CCFL model at the flow path. The CCFL correlation can be applied at specific locations in the 3D component and in the 1D vertical component. The CCFL correlations can be represented as Wallis form [13], Kutateladze form [14], and Bankoff form [15]. In TRACE, the CCFL model basically uses the Bankoff correlation, because the correlation reverts to the Wallis form by setting the scaling constant $\beta = 0$, and reverts to the Kutateladze form by setting $\beta = 1$.

Equations (1) and (2) show the Wallis correlation and Kutateladze correlation, respectively,

$$J_g^{1/2} + m_w J_l^{1/2} = C_w, \quad (1)$$

$$K_g^{1/2} + m_K K_l^{1/2} = C_K, \quad (2)$$

TABLE 1: The comparison of major parameters between IIST facility and the Maanshan NPP.

Parameter	IIST	Maanshan PWR	IIST/PWR
Design pressure (MPa)	2.1	15.6	1.35×10^{-1}
Maximum core power (MW)	0.45	2775	1.62×10^{-4}
Primary system volume (m ³)	5.37×10^{-1}	2.15×10^2	2.50×10^{-3}
Number of loops	3	3	1
Core			
Height (m)	1.0	3.6	2.77×10^{-1}
Hydraulic diameter (m)	1.08×10^{-1}	1.22×10^{-2}	8.85
Bypass area (m ²)	7.2×10^{-5}	1.54×10^{-2}	4.67×10^{-3}
Hot leg			
Inner diameter, D (m)	5.25×10^{-2}	7.35×10^{-1}	7.13×10^{-2}
Length, L (m)	2.0	7.28	2.75×10^{-1}
L/\sqrt{D} (m ^{0.5})	8.72	8.48	1.03
U-tube in one SG			
Number	30	5626	5.33×10^{-3}
Average length (m)	4.08	16.85	2.24×10^{-1}
Inner diameter (mm)	15.4	15.4	1.0
Volume (m ³)	2.28×10^{-2}	18.44	1.23×10^{-3}
Cold leg			
Inner diameter, D (m)	5.25×10^{-2}	7.87×10^{-1}	6.67×10^{-2}
Length, L (m)	5.0	15.7	3.18×10^{-1}
L/\sqrt{D} (m ^{0.5})	21.8	17.69	1.22
Downcomer			
Flow area (m ²)	0.0185	2.63	7.03×10^{-2}
Hydraulic diameter (m)	4.12×10^{-2}	4.8×10^{-1}	8.58×10^{-2}
Pressurizer			
Volume (m ³)	9.32×10^{-2}	39.64	2.35×10^{-3}
Surge-line flow area (m ²)	3.44×10^{-4}	6.38×10^{-2}	5.39×10^{-3}

where J_k and K_k are dimensionless mass flux (k : gas or liquid). The m and C are constants determined from the experiments

$$J_k = j_k \left[\frac{\rho_k}{gd(\rho_f - \rho_g)} \right]^{1/2}, \quad (3)$$

$$K_k = j_k \left[\frac{\rho_k^2}{g\sigma(\rho_f - \rho_g)} \right]^{1/4}.$$

Here, j_k and ρ_k are the superficial velocity and the density of phase (k : gas or liquid), d is the hole diameter, and σ is the surface tension.

4. Results and Discussions

4.1. Analysis Results of CCFL Model. In this study, the CCF may occur in the hot leg, the entrance to the steam generator, and the pressurizer surge line in IIST SBLOCA experiment. In order to verify the SBLOCA prediction of TRACE CCFL model, the comparisons of the results among Wallis correlation, Kutateladze correlation, and IIST data are considered in this paper. From (3), the hydraulic diameters

TABLE 2: The initial condition of the IIST SBLOCA experiment.

Parameter	IIST test data
Primary coolant system	
Core power (kW)	126
Pressurizer pressure (MPa)	0.958
Pressurizer water level (m)	1.459
Loop flow rate (kg/s)	0.217
Hot-leg temperature (K)	450
Cold-leg temperature (K)	409
Secondary coolant system	
Secondary-side pressure (MPa)	0.295
Secondary-side fluid temperature (K)	407

of pipe from 2.5 to 200 mm are calculated for the Wallis correlation and Kutateladze correlation of CCFL model, as shown in Figures 2 and 3. The pipe hydraulic diameter of reactor coolant system is 52.5 mm in IIST facility, so it is chosen the 50 mm results for the IIST CCFL model analysis in this study. Figure 2 shows the Wallis correlation plotted against the data. The constant m_w and C_w are both set to 1 from the results of Figure 2. The Kutateladze correlation

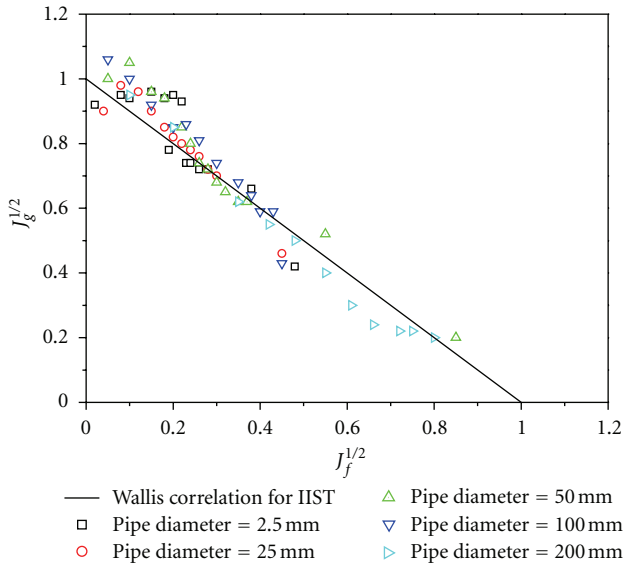


FIGURE 2: The Wallis correlation comparison with data (pipe diameter = 2.5–200 mm).

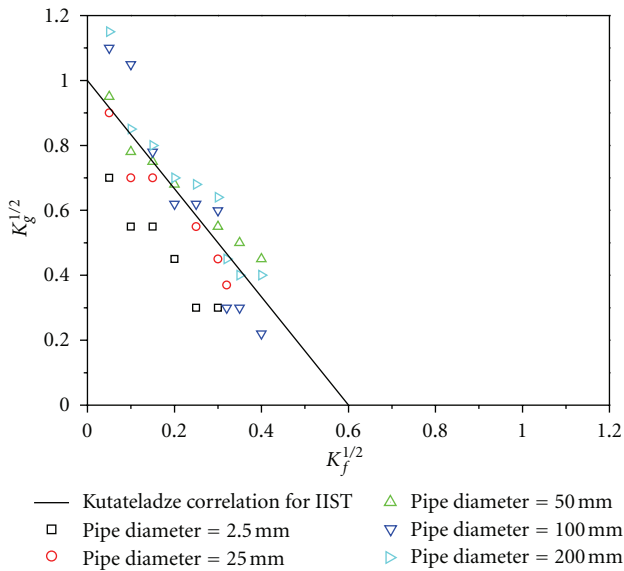


FIGURE 3: The Kutateladze correlation comparison with data (pipe diameter = 2.5–200 mm).

plotted against the data is shown in Figure 3. The constant m_k and C_k are set to 0.6 and 1, respectively.

Figure 4 shows the comparison of break flow rate and primary system pressure among Wallis form, Kutateladze form, and IIST data. The break flow rate and primary system pressure trends of Wallis form, and Kutateladze form are similar with the IIST data. Asymmetric natural-circulation flow rates were observed in the three loops during the IIST SBLOCA experiment. Figure 5 shows the comparison of loop 1 and loop 3 flow rate among Wallis form, Kutateladze form, and IIST data in the SBLOCA experiment. The trends of Wallis form and Kutateladze form are similar to the IIST

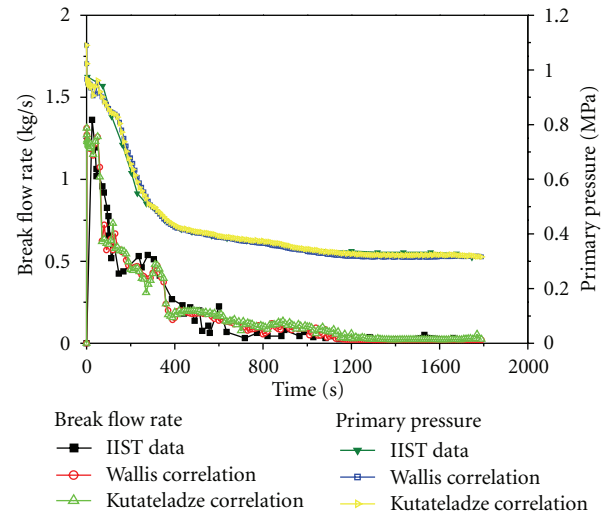


FIGURE 4: The comparison of break flow rate and primary pressure among Wallis form, Kutateladze form, and IIST data.

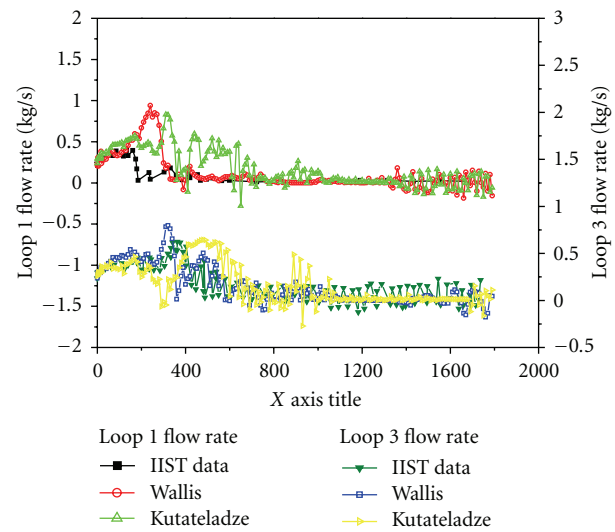


FIGURE 5: The comparison of loop 1 and loop 3 flow rate among Wallis form, Kutateladze form, and IIST data.

data. For loop 1, the IIST data show the inlet and outlet plenum of SG1 to empty after 500 s, as shown in Figure 6. Figure 6 indicates the Wallis form of CCFL model results compared with the IIST data are overpredicted during 400~1600 s. The Kutateladze form predictions of water level in the SG1 inlet plenum are the same trends with IIST data, except at 100~700 s. Figure 6 also shows the Wallis form and Kutateladze form overpredicted water level in the SG1 outlet plenum at 300~800 s. Figure 7 shows the comparison of the liquid holdup in the SG2 inlet plenum and SG3 outlet among Wallis form, Kutateladze form, and IIST data. There are the similar trends in this parameter. However, the water level of Wallis form and Kutateladze form predicted are lower than IIST data after 300 sec. According to the results of SG3 outlet plenum liquid level predicted by Wallis form and Kutateladze

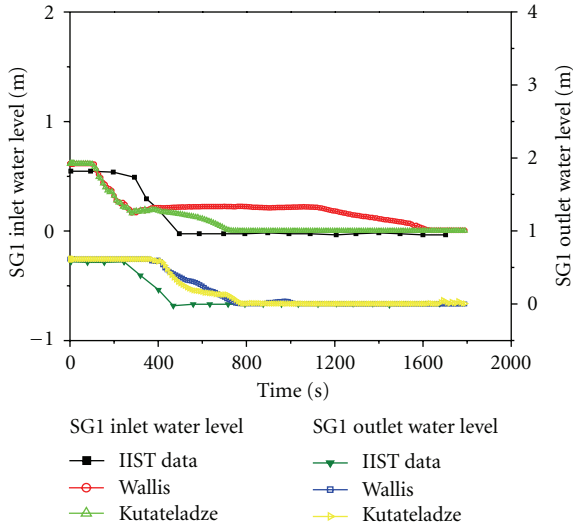


FIGURE 6: The comparison of SG1 inlet and outlet water level among Wallis form, Kutateladze form, and IIST data.

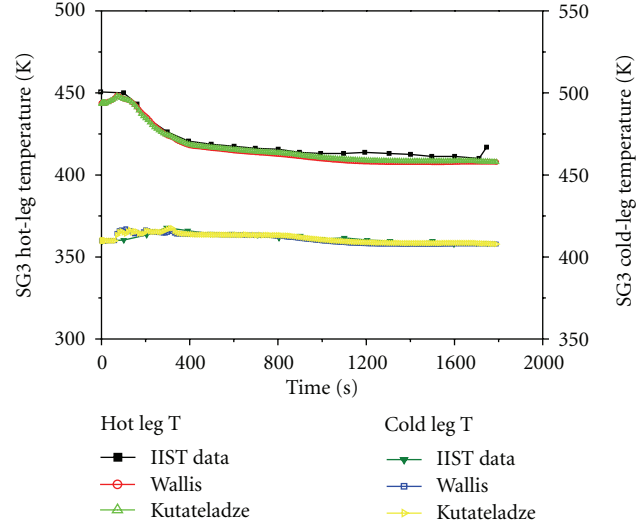


FIGURE 8: The comparison of SG3 hot leg and cold leg temperature among Wallis form, Kutateladze form, and IIST data.

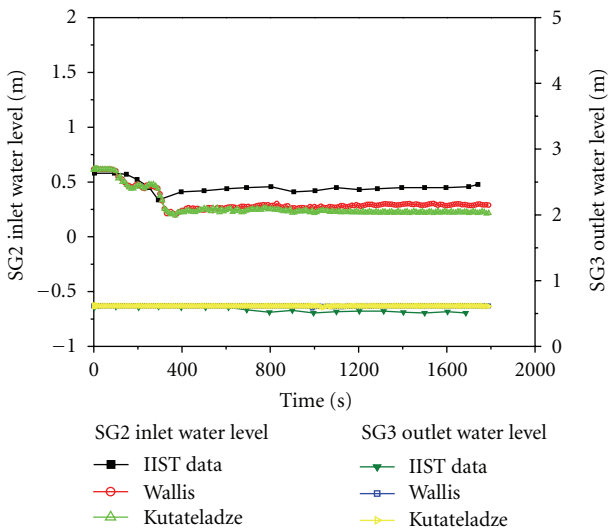


FIGURE 7: The comparison of SG2 inlet and SG3 outlet water level among Wallis form, Kutateladze form, and IIST data.

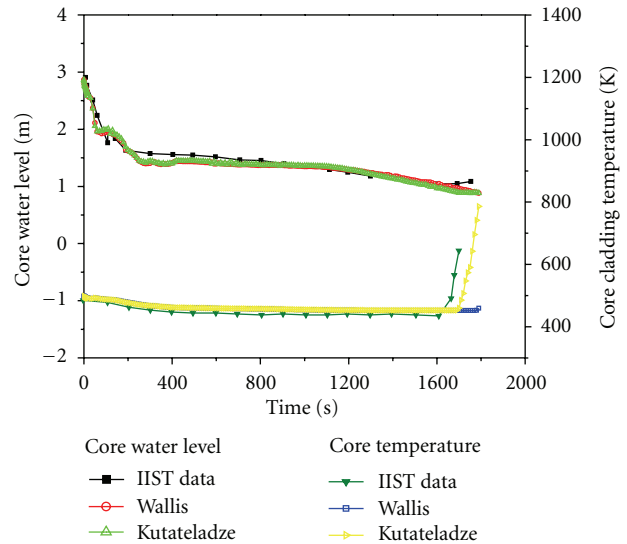


FIGURE 9: The comparison of core water level and cladding temperature among Wallis form, Kutateladze form, and IIST data.

form, the trends compared with IIST data are generally consistent in 0~700 s and overpredicted after 700 s. Figure 8 shows the fluid temperatures of the cold-leg and hot-leg in loop 3. The TRACE predicted the loop 3 fluid temperature to be in good agreement with the IIST experiment data. Figure 9 shows the comparison of the core liquid level and cladding temperature among Wallis form, Kutateladze form, and IIST data. The trends of their curves are similar. Besides, the TRACE can predict the time to reach the core uncover, which caused the core cladding temperature increase, as shown in Figure 9. The results show that the core cladding temperatures of Kutateladze form predicted are the same trends with IIST data. The core cladding temperature begins to increase when the core uncovered. Comparing to IIST

data and Kutateladze form, the trends of core cladding temperature predicted by Wallis correlation do not increase.

4.2. Sensitivity Studies of Kutateladze Correlation. From the results of Section 4.1, it is indicated using Kutateladze form of CCFL model in the IIST that TRACE model has a good SBLOCA behaviors prediction capability. Furthermore, the sensitivity studies of Kutateladze correlation for the water levels and core cladding temperature are verified and discussed in this paper. According to the results of Figure 3, the base values of C_k and m_k are 1 and 0.6, respectively. The sensitivity studies for Kutateladze correlation are setting the difference value for m_k and C_k . The first method is to maintain the constant C_k , and set the value of m_k for 1.0,

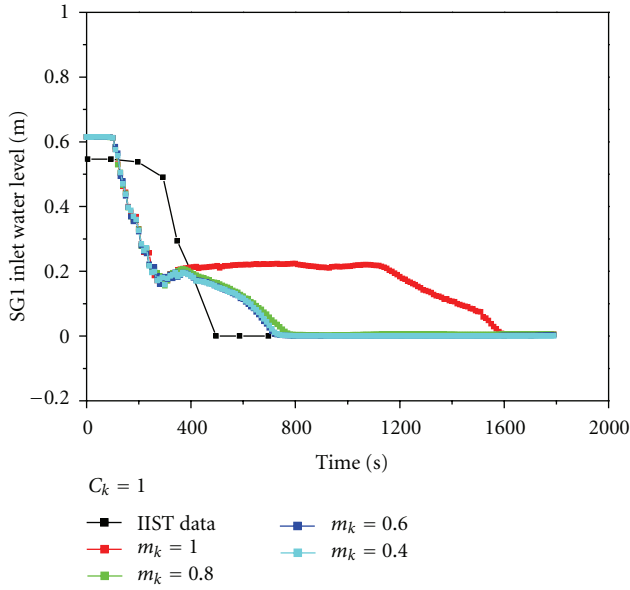


FIGURE 10: The CCFL sensitivity study of m_k for SG1 inlet water level.

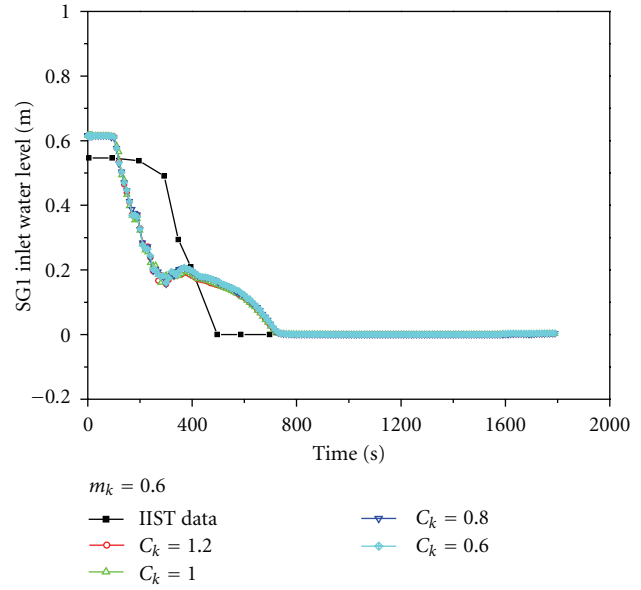


FIGURE 12: The CCFL sensitivity study of C_k for SG1 inlet water level.

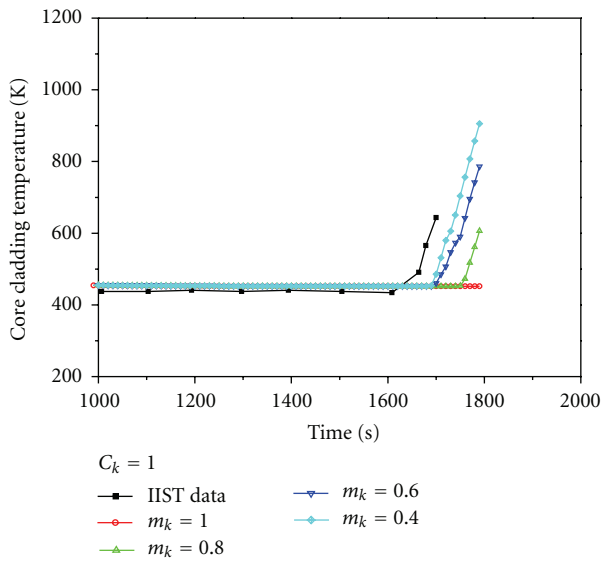


FIGURE 11: The CCFL sensitivity study of m_k for core cladding temperature.

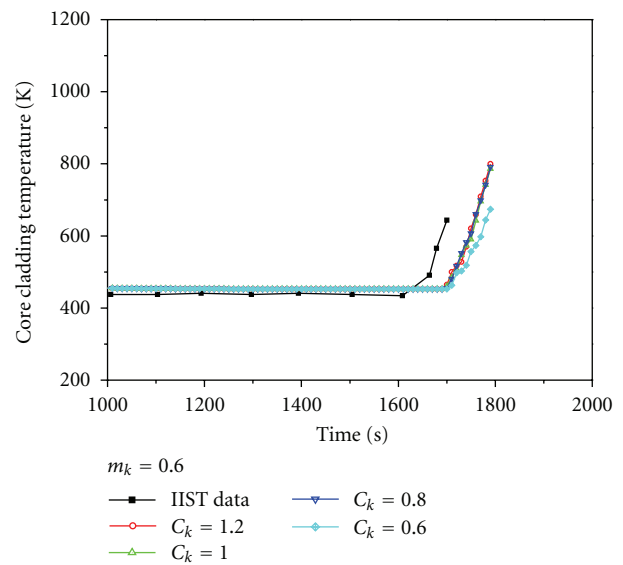


FIGURE 13: The CCFL sensitivity study of C_k for core cladding temperature.

0.8, 0.6, and 0.4, respectively. The other one is to maintain the constant m_k and set the value of C_k for 1.2, 1.0, 0.8, and 0.6, respectively. Figure 10 shows the sensitivity study of m_k for SG1 inlet water level. The results of $m_k = 1.0$ case overpredicted the water level after 400 s. By the way, the trends are almost the same without CCFL model. The results of $m_k = 0.8$ are different from the $m_k = 0.6$ and $m_k = 0.4$ between 600~800 s. It also indicates that the results of $m_k = 0.6$ and $m_k = 0.4$ are consistence. Figure 11 shows the sensitivity study of m_k for core cladding temperature.

The results of $m_k = 0.6$ and $m_k = 0.4$ show to predict the same times to reach the core uncover and to increase the core cladding temperature. The time of $m_k = 0.8$ predicted is later than $m_k = 0.6$ and $m_k = 0.4$. The core cladding temperature curve of $m_k = 1.0$ does not increase. Figure 12 shows the sensitivity study of C_k for SG1 inlet water level. The results of $C_k = 0.6\sim 1.2$ are almost the same. It indicates that the different values of C_k follow the same trend. The results are also shown in Figure 13. The different values of C_k predict

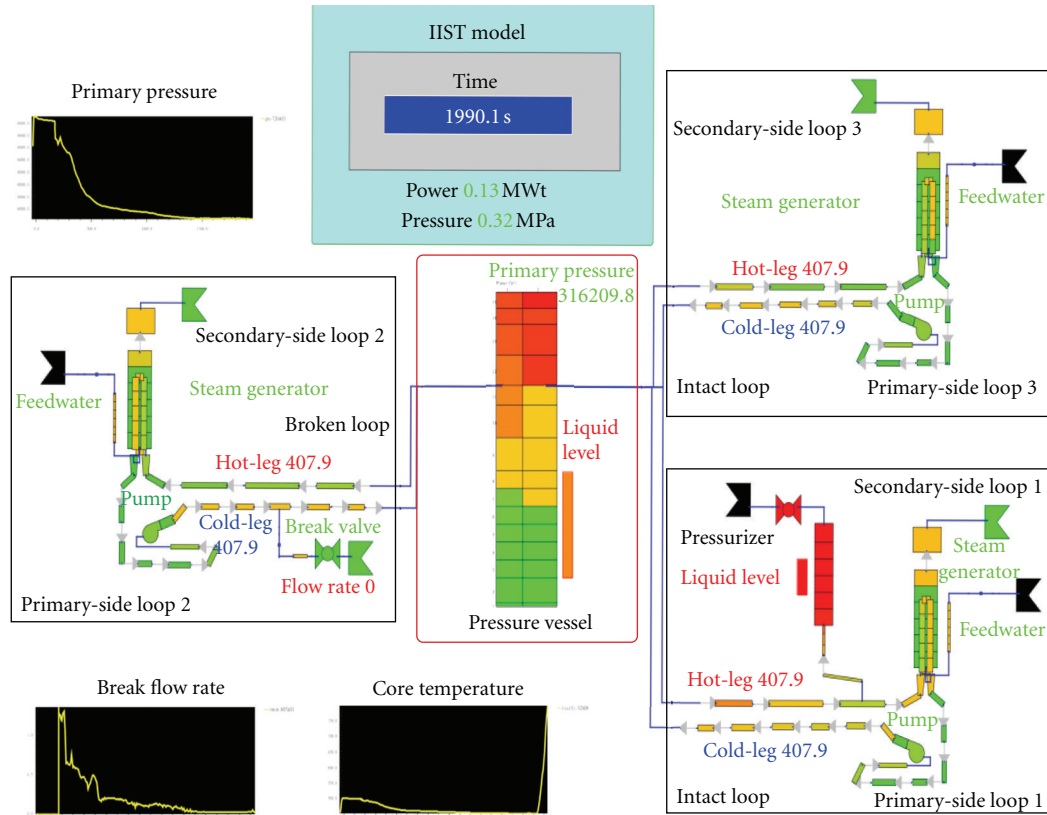


FIGURE 14: Animation of the IIST facility TRACE model for SBLOCA analysis.

the same times to reach the core uncover, and to increase the core cladding temperature.

For the 50 mm pipe of the reactor coolant system analysis, the above sensitivity studies of CCFL in IIST TRACE model indicate that using the values of $m_k = 0.6$ and $C_k = 1$ for Kutateladze correlation can well predict the SBLOCA behavior and the results present good agreement with IIST SBLOCA experiment data.

Furthermore, the animation of the IIST TRACE model is presented using the animation function of TRACE/SNAP interface with analysis results, such as primary pressure, break flow rate, and core cladding temperature. The animation model of IIST is shown in Figure 14.

5. Conclusions

By TRACE/SNAP code, the TRACE model for IIST facility is developed and verified with the SBLOCA experiment of IIST facility. In TRACE code, the CCFL model includes the Wallis correlation and Kutateladze correlation. In order to verify the SBLOCA prediction of TRACE CCFL model, the comparisons of the results among Wallis correlation, Kutateladze correlation, and IIST data are considered in this paper. The TRACE analyses results, such as break flow rate, primary pressure, the temperature of cold leg and hot leg, and core cladding temperature, are consistent with the IIST data. It also indicates that the results of Kutateladze form predicted can best represent the results of IIST data. Besides,

the sensitivity studies of Kutateladze correlation are verified and discussed in this paper. The best values of m_k and C_k for IIST TRACE model are 0.6 and 1, respectively. In summary, since our current paper has shown good agreements between IIST data and TRACE results using Kutateladze correlation of CCFL model, future applications of this model are highly recommended for SBLOCA analysis.

References

- [1] C. H. Lee, "INER integral system test (IIST) facility for simulating the Maanshan nuclear power plant—investigation of PWR natural circulation," *Journal of Nuclear Science and Technology*, vol. 31, p. 83, 1994.
- [2] C. H. Lee, T. J. Liu, W. T. Hong, I. M. Huang, Y. K. Chan, and C. J. Chang, "Experimental investigation of PWR small break loss-of-coolant accidents in IIST facility," *Journal of Nuclear Science and Technology*, vol. 33, pp. 251–259, 1996.
- [3] C. H. Lee, T. J. Liu, Y. S. Way, and D. Y. Hsia, "Investigation of mid-loop operation with loss of RHR at INER integral system test (IIST) facility," *Nuclear Engineering and Design*, vol. 163, no. 3, pp. 349–358, 1996.
- [4] Y. M. Ferng and C. H. Lee, "Numerical simulation of natural circulation experiments conducted at the IIST facility," *Nuclear Engineering and Design*, vol. 148, no. 1, pp. 119–128, 1994.
- [5] Y. M. Ferng and C. H. Lee, "Comparison of the RELAP5/MOD3 code with the IIST natural circulation experiments," *Nuclear Technology*, vol. 111, no. 1, pp. 34–45, 1995.

- [6] C. Y. Chang, C. H. Lee, T. J. Liu, and Y. K. Chan, "Experimental investigation of loss of feedwater with bleed and feed operation," *Journal of Nuclear Science and Technology*, vol. 33, pp. 318–323, 1996.
- [7] P. S. Damerell and J. W. Simons, "Reactor Safety Issues Resolved by the 2D/3D Program," NUREG/IA-0127, 1993.
- [8] US Nuclear Regulatory Commission (USNRC), TRACE V5.0 User Manual, 2007.
- [9] J. R. Wang, H.-T. Lin, C.-J. Chang et al., "The development and verification of TRACE model for IIST experiments," NUREG/IA-0252, 2011.
- [10] C. J. Chang, C. H. Lee, W. T. Hong, and L. L. C. Wang, "IIST small break LOCA experiments with passive core cooling injection," *Nuclear Engineering and Design*, vol. 236, no. 1, pp. 19–34, 2006.
- [11] C. H. Lee, I. M. Huang, C. J. Chang, T. J. Liu, and Y. M. Ferng, "Using an IIST SBLOCA experiment to assess RELAP5/MOD3.2," *Nuclear Technology*, vol. 126, no. 1, pp. 48–61, 1999.
- [12] S. Wongwises, "Two-phase countercurrent flow in a model of a pressurized water reactor hot leg," *Nuclear Engineering and Design*, vol. 166, no. 2, pp. 121–133, 1996.
- [13] G. B. Wallis, *One Dimensional Two Phase Flow*, McGraw-Hill, New York, NY, USA, 1969.
- [14] S. S. Kutateladze, "A hydrodynamic theory of changes in the boiling process under free convection conditions," *Izvestiya Akademii Nauk SSSR, Otdelenie Tekhnicheskikh Nauk*, vol. 8, p. 529, 1951.
- [15] S. G. Bankoff, R. S. Tankin, M. C. Yuen, and C. L. Hsieh, "Countercurrent flow of air/water and steam/water through a horizontal perforated plate," *International Journal of Heat and Mass Transfer*, vol. 24, no. 8, pp. 1381–1395, 1981.